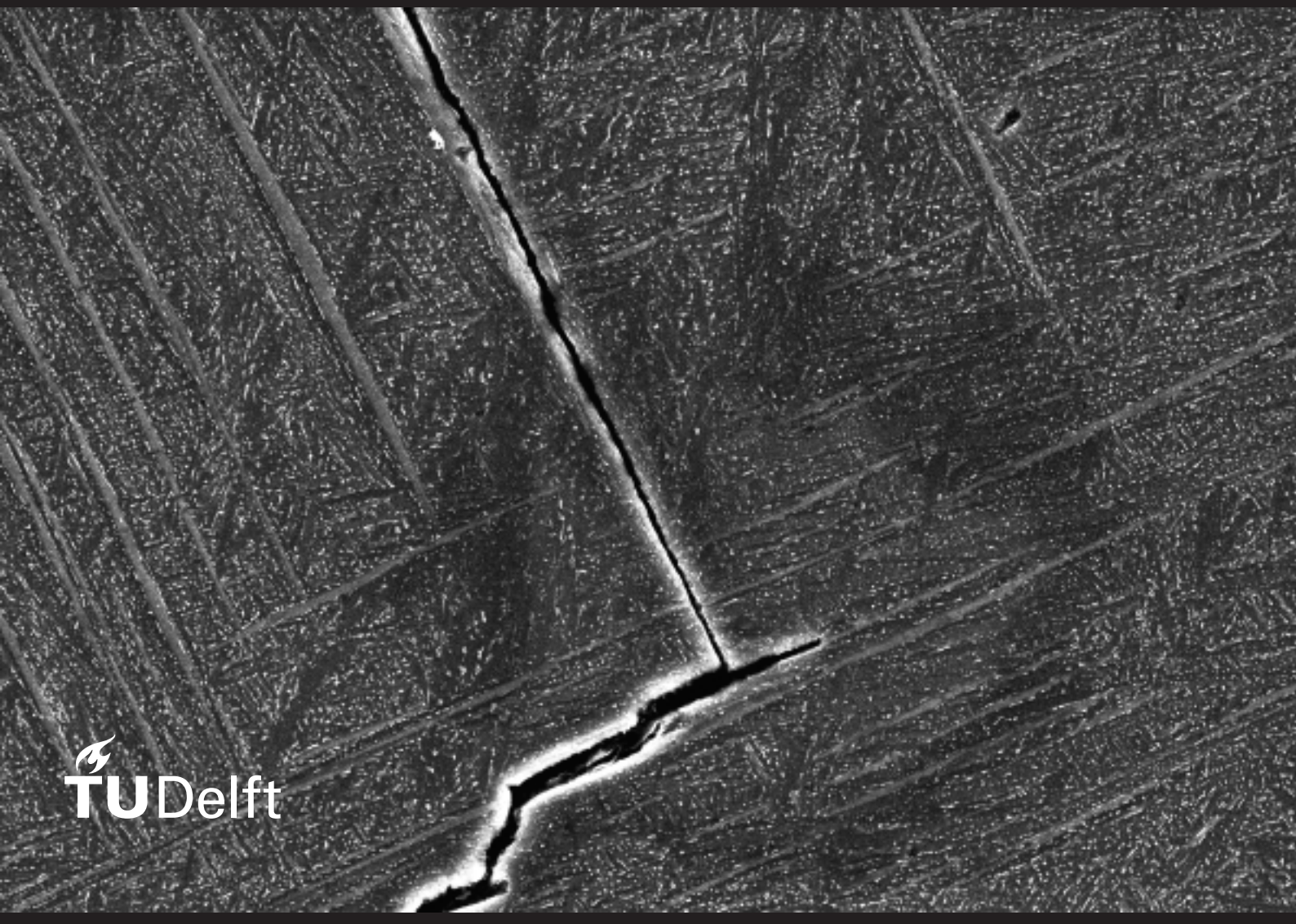
Fatigue of additively manufactured Ti-6Al-4V using sub-sized samples

Master of Science Thesis

Sreyas Chellu



TU Delft

Fatigue of additively manufactured Ti-6Al-4V using sub-sized samples

Master of Science Thesis

by

Sreyas Chellu

to obtain the degree of Master of Science

at the Delft University of Technology,

to be defended publicly on Monday August 29, 2022 at 09:00 AM.

Student number:	5275458	
Project duration:	November, 2021 – August, 2022	
Thesis committee:	Dr. V.A. Popovich,	TU Delft, supervisor
	Dr. ir. C. Ayas,	TU Delft
	Dr. ir. S. Kumar,	TU Delft
	Dr. ir. A.C. Riemslag,	TU Delft

An electronic version of this thesis is available at
http://repository.tudelft.nl/.

TU Delft

Acknowledgements

The journey of my master thesis has been nothing short of challenging to say the least. It has been a steep learning curve which required patience, discipline and out of the box thinking. The thesis has however only increased my love for materials science.

I would like to extend my deepest gratitude to Dr. Vera Popovich, without whom the project would not have been possible, for her constant support, knowledge and critical discussions. I would like to thank Nicolas Macallister for his huge help in this project. I will miss our discussions early in the mornings and over coffee on a daily basis. It has been a pleasure working with you. Thanks are also in order for Dr.Ton Riemslag and Sean Scott for their help with setting up the tests. I would also like to thank everyone working in and around the mechanical behaviour lab for their help. Having lunch with the people from the lab is definitely something I will cherish for a long time.

Personally, I would like to thank all my friends for being there for me whenever required. Lastly, I would like to thank my parents and my brother for their unconditional love and constant support over the last two years.

Sreyas Chellu
Delft, August 2022

Abstract

Additive manufacturing (AM) is quickly becoming one of the more popular methods to manufacture components made of Ti-6Al-4V in the aerospace and automobile industry due to its flexibility in producing complex geometries and reducing tooling costs. As the world of additive manufacturing is still relatively young, there is no globally accepted method for the certification of AM parts, allowing freedom to develop procedures to utilize the advantages of AM. To greatly reduce material wastage, the use of smaller specimens has been explored to characterize the mechanical properties of the material.

This study aims to analyze the influence of test specimen size on the near threshold fatigue properties of Ti-6Al-4V manufactured by conventional processes and Laser powder bed fusion (LPBF) . Two different specimen sizes were utilized, the standard size and the sub-sized specimens. The effect of two heat treatments, stress relief (SR) and annealing (AN) on the LPBF material on the fatigue properties was also studied. In addition, the effect of anisotropy on the fatigue threshold value was also touched upon in this study. A fatigue test setup for the sub-sized samples was designed and a constant K_{max} test was employed to characterize the threshold properties. The direct current potential drop (DCPD) method was employed to measure the crack length during the test.

The fatigue threshold of the SR microstructure did not show any effect due to sample size. This was attributed to the partly intergranular crack propagation observed playing a prominent role in the fatigue threshold. The conventional and annealed samples witnessed a drop in threshold values of about 0.5 MPa$\sqrt{m}$ when sub-sized samples were used. It was observed that the sub-sized samples had a greater crack depth at threshold leading to increased constraint at the crack tip and hence smaller degree of crack closure explaining the drop in threshold values.

The current study has thus established successfully the feasibility of using sub-sized specimens to characterize the near threshold fatigue properties of conventionally and additively manufactured Ti-6Al-4V.

Nomenclature

ΔK	Stress intensity range
ΔK_{th}	Threshold stress intensity range
σ_{YS}	Yield strength
a/W	Crack ratio or crack depth
AC	Air cooling
AN	Annealed
B	Thickness
BCC	Body centered cubic
C	Stress intensity gradient
da/dn	crack growth rate
FC	Furnace cooling
HCP	Hexagonal close packed
HIP	Hot Isostatic Pressing
K_{max}	Maximum stress intensity value
K_{min}	Minimum stress intensity value
$LEFM$	Linear Elastic Fracture Mechanics
$LPBF$	Laser Powder Bed Fusion
R	Stress/Load ratio
R_p	Plastic zone size
S	Span
$SENB$	Single Edge Notched Bending
SR	Stress relieved
T_β	Beta transus temperature
$Ti-64$	Ti-6Al-4V

W	Width
XRD	X Ray Diffraction

Contents

1 Introduction **1**

2 Background **3**
2.1 LPBF Parameters . . . 4
2.2 Defects . . . 5
2.3 Microstructure . . . 7
2.3.1 Conventional Ti-6Al-4V . . . 8
2.3.2 LPBF Ti-6Al-4V . . . 9
2.4 Mechanical properties . . . 14
2.5 Introduction to fatigue . . . 16
2.6 Near threshold fatigue properties of LPBF Ti-6Al-4V . . . 20
2.7 Conclusions . . . 26
2.7.1 Research gaps . . . 27
2.8 Research Objectives . . . 27

3 Materials and Methods **29**
3.1 Materials . . . 29
3.1.1 Manufacturing and heat treatment . . . 29
3.1.2 Geometry and dimensions . . . 30
3.2 Microstructure Characterization . . . 31
3.2.1 Microscopy . . . 32
3.2.2 Hardness . . . 33
3.2.3 X-Ray Diffraction . . . 33
3.3 Fatigue testing . . . 33
3.4 Summary of fatigue tests . . . 38

4 Results and discussion **41**
4.1 Effect of heat treatment on microstructure . . . 41
4.2 XRD analysis . . . 44
4.3 Hardness . . . 46
4.4 Fatigue behaviour . . . 48
4.4.1 Effect of heat treatment . . . 48
4.4.2 Effect of anisotropy . . . 50
4.4.3 Influence of microstructure on crack propagation . . . 50
4.4.4 Fracture surface analysis . . . 54
4.4.5 Effect of sample size . . . 56

5 Conclusions and future recommendations **65**
5.1 Conclusions . . . 65
5.2 Future recommendations . . . 66

A Fatigue test fixtures drawing **69**
A.1 Large sample fixture drawing 69
A.2 Small sample fixture drawing 69

B Crack curvature measurement **71**

C Validity of fatigue tests **73**

D Matlab codes **75**

List of Figures

2.1 Schematic of the LPBF process. Reproduced from [12] 3
2.2 a)Important process parameters of LPBF.Adapted from [13], b)Illustration of the important processing parameters of LPBF. Reproduced from [14] 4
2.3 Equilibrium phase diagram of Ti-6Al-4V. Reproduced from [32]. 8
2.4 Phases as a function of cooling rates. Reproduced from [33]. 8
2.5 Optical micrographs of Ti-64 microstructures: a) bimodal, b) lamellar and c) equiaxed. Reproduced from [37],[38] 9
2.6 As fabricated LPBF Ti-64 a) Optical micrograph showing columnar grains b) SEM image showing acicular martensite. Reproduced from [41]. . . . 10
2.7 Microstructure after annealing at 870°C followed by a) AC, b) FC. Reproduced from [34] 12
2.8 Microstructure showing the difference in α colony size for different residence times. a) 1020°C for 2h, b) 1040°C for 20h. Reproduced from [42] 13
2.9 Tensile curve showing anisotropy in properties. Reproduced from [60] . 16
2.10 Parameters to describe fatigue loading. Reproduced from [6] 17
2.11 LEFM fracture modes. Reproduced from [64] 17
2.12 Schematic of the $\frac{da}{dn}$ versus ΔK curve showing the different stages. Reproduced from [66]. 18
2.13 Schematic showing ΔK_{eff} as a result of crack closure. Reproduced from [67] 19
2.14 Schematic showing different mechanisms of crack closure. Reproduced from [68] 20
2.15 FCGR curves obtained by Tarik Hasib et al [76] 22
2.16 Effect of load ratio in the near threshold fatigue region. Reproduced from [77] 23
2.17 Schematic showing the influence of microstructural features on fatigue crack propagation. Reproduced from [79]. 24
2.18 Effect of microstructure size on fatigue threshold. Reproduced from [76]. 24
2.19 Illustration of the R constant (red) and constant K_{max} (blue) tests. Reproduced from [77]. 25

3.1 Different heat treatments on the conventional and LPBF samples. . . . 30
3.2 Projected views of the large SENB sample 31
3.3 projected views of the small SENB sample 31
3.4 Schematic showing the different orientations and the crack planes. . . . 31
3.5 Plane of measurement for the hardness tests. 33
3.6 Large sample fatigue test setup a) zoomed out, b) zoomed in 34
3.7 Small sample fatigue test setup a) zoomed out, b) zoomed in 35
3.8 Schematic of a) large sample , b) small sample test setup. 36

3.9 Illustration of the constant Kmax test. 37
3.10 Summary of the fatigue tests 39

4.1 Optical micrographs of the conventional microstructure. 41
4.2 Optical micrograph of the stress relieved microstructure. 42
4.3 Optical micrographs of the annealed microstructure. 43
4.4 SEM micrographs of large a) conventional, b) Stress relieved and c) annealed microstructures. Dashed lines in (b) and (c) show PBG and alpha colony respectively.) 44
4.5 SEM micrographs of small a) conventional, b) Stress relieved and c) annealed microstructures. 45
4.6 XRD results of a) Conventional, b) Stress relieved and c) Annealed samples. 46
4.7 Hardness of the different samples 47
4.8 Effect of heat treatment on large sample fatigue threshold 48
4.9 Effect of heat treatment on small sample fatigue threshold 49
4.10 Fatigue crack growth rate curve of stress relieved microstructure in the vertical and horizontal orientations. 50
4.11 Crack profile through the conventional microstructure. (a),(b) large sample steady growth and threshold regime, (c),(d) small sample steady growth and threshold regime. Arrow directs to an enlarged bifurcation in (b). 52
4.12 Crack profile through the stress relieved microstructure. (a),(b) large sample steady growth and threshold regime, (c),(d) small sample steady growth and threshold regime. Enlarged figures represent intergranular crack propagation in (b),(d). 53
4.13 Crack profile through the annealed microstructure. (a),(b) large sample steady growth and threshold regime, (c),(d) small sample steady growth and threshold regime. Yellow line shows a PBG boundary in (a). Enlarged figures show crack tortuosity in (b),(d). 54
4.14 SEM micrograph showing the fracture surface of the conventional sample (a) Large, (b) Small. 55
4.15 SEM micrograph showing the fracture surface of the stress relieved sample (a) Large, (b) Small. White arrows point to stairs and ridges on the surface. 55
4.16 SEM micrograph showing the fracture surface of the annealed sample (a)Large, (b) Small. White arrows point to ridges in the surface. 56
4.17 SEM micrograph of the annealed fracture surface with the arrow showing ductile tearing in the (a) large, (b) small sample. 57
4.18 Fatigue crack growth rates of a) conventional, b) stress relieved and c) annealed microstructures. 58
4.19 Schematic showing the mechanism of roughness induced crack closure. Reproduced from [88]. 59
4.20 BSE micrographs of the fracture surfaces in the threshold regime of a) Large conventional, b) small conventional, c) large stress relieved, d) small stress relieved, e) large annealed and f) small annealed 60
4.21 Crack front in the conventional sample (a) Large, (b) Small 62

4.22 Crack front in the stress relieved sample (a) Large, (b) Small 63
4.23 Crack front in the annealed sample (a) Large, (b) Small 63

A.1 Drawing of the large sample fixture [98] 69
A.2 Drawing of the small sample fixture 70

B.1 Measurement of crack curvature in the large stress relieved sample . . 71

C.1 Constant ΔK test result. 73

List of Tables

2.1 Tensile properties of as fabricated and heat treated LPBF Ti-64 14

3.1 Laser powder bed fusion process parameters 29
3.2 Steps for sanding of Ti-6Al-4V 32

4.1 Phase fractions in the different samples determined by XRD. 45
4.2 Summary of the threshold fatigue test results 51
4.3 Monotonic plastic zone size ahead of the crack tip for the different microstructures. 54
4.4 Fracture surface roughness of the different samples 61
4.5 a/W values at threshold for the different samples 62
4.6 Degree of crack curvature in all samples. All values are in μm. 63

1 Introduction

Ti-6Al-4V, also commonly known as Ti-64 is a titanium alloy primarily composed of two phases, α and β. The alloy was initially developed in the 1950s for structural components in air crafts. But in the present day, Ti-64 finds itself as a useful material in a multitude of industries owing to its strength, weight, fracture toughness, corrosion resistance and biocompatability [1]. In the aerospace industry, Ti-64 is used for the manufacturing of airframe parts such as skin panels, wing boxes etc, and fans of a compressor in a jet engine owing to its high impact strength, low coefficient of thermal expansion and high strength to weight ratio [2]. In the biomedical field, Ti-64 is used as a bio implant in different parts of the body such as heart valve prosthesis, hip, shoulder, knee and stents due to its excellent combination of great mechanical properties and excellent corrosion resistance and biocompatability. In addition, the relatively low stiffness of the alloy when compared to metals like steel helps reduce the effect of stress shielding [3]. In the marine industry, Ti-64 is used in offshore oil and gas production and also as structural components in the ship building industry due to its high strength and corrosion resistance [4].

The conventional methods of manufacturing Ti-64 components include casting, forging, rolling of bulk material followed by further machining to the required shape and size of the product. Some of the limitations of conventional machining of Ti-64 are the low thermal conductivity, tendency of strain hardening and high affinity to oxygen leading to the formation of oxide layers. These limitations lead to the manufacturing being expensive, excessive material wastage and having high lead times. This led to the use of additive manufacturing which offers a large amount of flexibility in the design of the components as well as extremely low material wastage. To quantify the reduce in cost and material, a buy-to-fly(BTF) ratio is utilized. The BTF ratio is defined as the ratio of the weight of the initial raw material to the weight of the final product. It was seen that the BTF ratio of a titanium component in the aerospace industry produced by conventional machining was in the range of 12-30 while the ratio was reduced to as much as 3-12 when produced using additive manufacturing [5].

The components made of Ti-64 undergo various types of loading and stresses during its service lifetime. One important type of loading is cyclic loading leading to fatigue of the material. Near threshold fatigue is crucial as 85% of the fatigue lifetime

of a component is during the crack initiation phase [6]. Research on using miniature specimens to determine the mechanical properties of a material began in the 1980s for the nuclear industry to test materials pre and post irradiation [7, 8]. Sub- sized specimens could also be utilized for testing to massively reduce material usage. This is even more relevant in the case of additively manufactured materials. In the case of complex designs, a scaled down version of the component could be manufactured and tested for mechanical properties. The use of sub sized samples to characterize the mechanical properties of materials/components could lead to standardized part certification. As additively manufactured components also show signs on anisotropy, the position of the component whose properties are desired could be extracted and tested for it's properties. Sub-sized samples could also be utilized in the electronic industries where there is an ever decreasing size of the components [9]. So far, research using sub-sized specimens has mostly been focused in determining the static mechanical properties of materials. For fatigue properties, sub-sized samples have been mostly used for determining the fatigue crack growth rate properties in the Paris region and fatigue lifetime using S-N curves. Minimal research has been done to evaluate the near threshold properties of sub-sized samples [10] and hence, this study focuses on the feasibility of using sub-sized samples and its effect on the near threshold fatigue properties of additively manufactured Ti-6Al-4V.

The outline of the report is as follows

1. Chapter 2: Background - Contains the necessary literature and fundamentals to understand the report.
2. Chapter 3: Materials and methods - Shows the various techniques used to characterized the materials and the experimental design setup to determine the fatigue properties.
3. Chapter 4: Results and discussions - Provides the obtained results and the critical explanations of the the results.
4. Chapter 5: Conclusions and recommendations - The major findings of the study and future recommendations to continue the study.

2

Background

Laser powder bed fusion is one of the most popular additive manufacturing methods to fabricate metal components. The working principle of LPBF involves a layer of metal powder distributed on the base plate followed by heating the powder using a laser in an inert environment as prescribed by the CAD model. LPBF uses a CO_2 laser with a wavelength of 10.6μm or a Neodymium-doped yttrium aluminum garnet (Nd-YAG) laser with a wavelength of 1.06μm to heat the powder [11]. The heating is done in an environment of nitrogen or argon to prevent oxidation of the sample which could reduce the ductility of the component. A schematic of the LPBF process is shown in Figure 2.1.

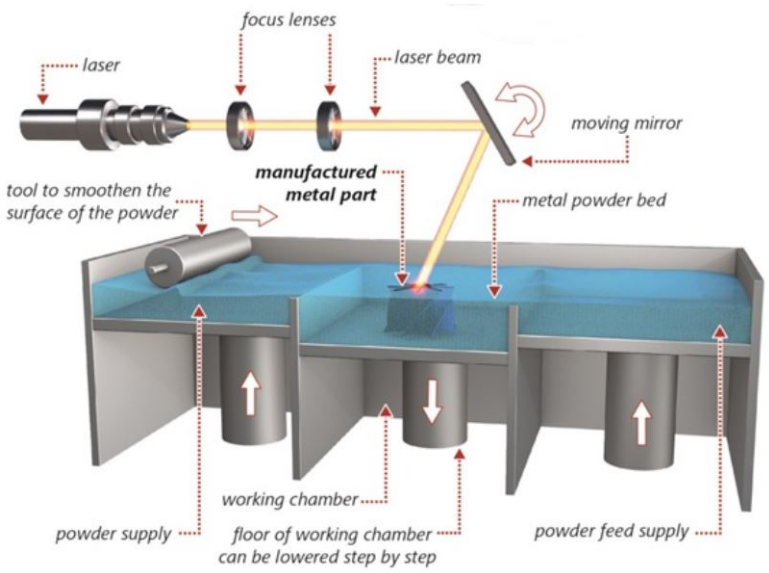


Figure 2.1: Schematic of the LPBF process. Reproduced from [12]

As seen from the figure, lenses are used to focus the laser beam and mirrors are used to direct the laser beam to the desired spot. The powder feed supply provides the powder for every new layer and the working chamber can be lowered to accordingly accommodate the height of the component. Upon heating, the powder melts to form the melt pool which solidifies upon cooling as the laser moves. After solidification

of the melt pool of one layer, a new layer of powder is added and the process is repeated until the component is fabricated. The working chamber is lowered after the deposition of each new layer of the powder. Once the entire component is fabricated, it is removed from the base plate/substrate by electrical-discharge machining(EDM).

2.1. LPBF Parameters

To optimize the overall LPBF process to obtain desired properties in the component and increased efficiency of the overall process, different processing parameters have to be optimized. The various important parameters are shown in Figure 2.2a and an illustration of the parameters is shown in Figure 2.2

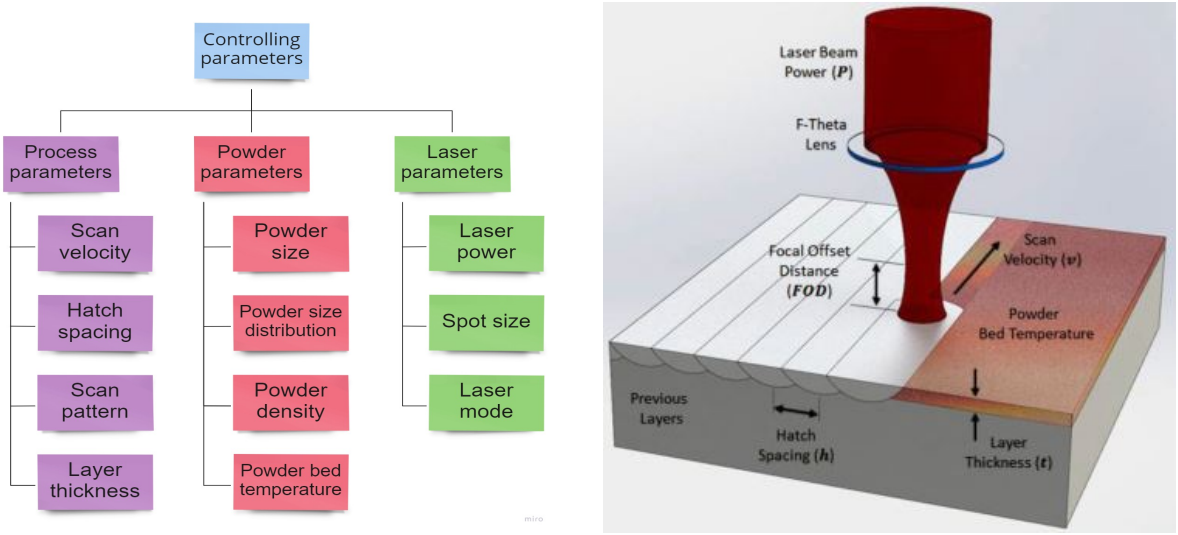


Figure 2.2: a)Important process parameters of LPBF.Adapted from [13], b)Illustration of the important processing parameters of LPBF. Reproduced from [14]

Kumar et al broadly classified the important parameters into 3 types: powder related, laser related and parameters related to the process itself [13] as shown in the figure. The parameters related to the powder are called pre-process parameters while the parameters related to laser and the process itself are called in-process parameters.

The important parameters that can be controlled with the powder are powder size, powder size distribution, powder density and powder temperature. To achieve a part with high density, it is necessary to have a powder bed with high density. High density can be achieved by aving spherical powder particles. Having all powder particles of the same size would result in a lot of gaps. Hence, powders having different sizes are preferred. Powders that are too small have a large surface area resulting in a lot of pores. At the smaller size, interatomic forces also come into play restraining good flowability of the powder. On the other hand, if the powder size is too big, the time taken to melt them is also high, thus decreasing the efficiency of the process. The size distribution of the powder also influences the LPBF process. It has been found that a narrow powder size distribution (PSD) is necessary for good flowability

of the powder while a wider PSD is necessary to achieve a high powder bed density. Hence, a suitable particle size distribution is to be chosen to optimize the proceedings [15]. A particle size range between 20μm and 70μm was observed for Ti-64 [16]. The final parameter regarding the powder is the powder bed temperature. To reduce the thermal gradient during the process, the powder bed can be pre heated to reduce the initiation of residual stresses in the final component [17].

The different parameters related to the laser are laser power (P), spot size and the laser mode. The parameters related to the LPBF process itself are scan velocity(v), hatch spacing(h), scan patters and layer thickness (t) . The laser in an LPBF machine has a power range of 50-1000W. Increasing the laser power allows higher temperatures to be reached. The spot size is the diameter of the laser beam. If products with high resolution is required, a smaller spot size is chosen. On the other hand, having a smaller spot size would require increased scan cycles, thus reducing the production rate or efficiency of the process. The scan velocity is the speed with which the laser beam moves across the powder bed. Hatch spacing is the distance between two consecutive scan lines, having a similar relation as the spot size to process efficiency. A large hatch spacing increases the production rate but would decrease the degree of remelting, affecting the density of the component. A small hatch spacing would mean a complete melting of the powder but decreases the production rate. The scan pattern describes how the laser traces across the powder bed. Scan pattern is an important parameter influencing the degree of anisotropy in the component. The layer thickness is the thickness of each layer of powder that is deposited after a cycle. A small layer thickness would require less power to melt while a large thickness would require more power to melt completely [13].

Combining a few of the process parameters, an important term is defined for laser AM processes, the volume energy density (E) which is the average applied energy per volume of material. Volume energy density is calculated as follows

$$E = \frac{P}{v \times h \times t} \tag{2.1}$$

where E is the energy density in J/mm^3, P is the laser power in W, v is the scan velocity in mm/s, h is the hatch distance in mm and t is the layer thickness in mm. Volume energy density plays an important role in the melt pool dynamics. The melt pool is the resultant of the interaction between the powder and the laser. The characteristics of the melt pool such as temperature field, shape, size, its evolution and flow dynamics influences the temperature gradient and solidification rate of the LPBF process that decides the final microstructure that is obtained [18]. Due to high laser powers and short interaction times, high temperatures and high cooling rates are experienced in the melt pool. Yaroditsev et al reported temperatures up to 2710K and Hocine et al observed cooling rates of 10^4-10^6°C/s respectively in their processes [19],[20].

2.2. Defects

As explained previously, the LPBF process has an incredibly complex thermal behaviour due to directional melting, cooling opposite to the direction of heat transfer and repeated melting/solidification due to multiple scan cycles and small hatch spacing. The process above is controlled by a myriad pre-processing and in process parameters that are inter dependant and dynamically influence the features and properties of the component. As a result, optimization of all the parameters is close to impossible and the presence of defects are inevitable. These defects could be detrimental to the mechanical properties of the component and hence, the origin of the defects have been extensively studied. Some of the defects and their origin and effects are explained in this section.

Porosity is an undesirable manufacturing defect when a highly dense component is required. Porosity is a type of geometrical defect detrimental to the mechanical properties of the material, especially in fracture mechanics. Porosity can be classified into two types, gas pores and lack of fusion pores. Gas pores are spherical in shape and are a result of the entrapment of the gas molecules in the melt pool. When the scanning velocities are high, there is insufficient time for the gas atoms to escape and they are trapped in the melt pool. They can be atoms from the inert atmosphere, such as Argon. Gas pores can be reduced by lowering the scan velocities but they cannot be completely eliminated. These pores act as stress concentrators when the component is subjected to a stress [1]. Gas pores can also be a result of poor powder quality and trapment of gas molecules during atomization. Lack of fusion pores are not caused due to the gaseous atoms, but due to incomplete melting of the metal powders. These defects can also be caused due to poor bonding between two successive layers. This is caused due to a lack of energy density causing a small melt pool. Unlike the gas pores, the lack of fusion pores are sharp and elongated in shape. This makes them more dangerous than gas pores as they act as very high stress concentrators [21].

Surface roughness is a common surface characteristic in LPBF fabricated components and is caused due to three reasons according to Li et al [22],

- Staircase effect due to the layer by layer fabrication in AM processes.
- Incomplete melting of powder particles that are then adhered to the surface.
- Presence of defects.

Staircase effect is the characteristic by which surface roughness is not homogeneous on all surfaces of the component. The surface that is facing the powder bed has more chances of picking up the unmelted powder particles, leading to a higher surface roughness. This was also seen by Edwards et al who concluded that surface roughness is dependant on the build orientation of the component [23]. According to Chen et al, a powder size distribution that has a larger percentage of coarser particles than finer particles would result in a rough surface. The authors observed that the surface roughness increases with the layer thickness. The authors also observed that the process parameters affect the surface roughness when the ”optimal” values for the process parameters to obtain a highly dense sample showed significant surface

roughness [24]. Yadollahi et al also observed that with increasing scan speed and hatch distance, the value of surface roughness increases [25]. Due to the irregularities in the surface, stress concentrations are created which then act as fatigue crack initiation points, thus reducing the threshold limit of the component.

Residual stresses are the stresses that remain in a component at equilibrium after fabrication. Residual stresses originate due to non-uniform plastic deformation [26]. As LPBF is a process with a complex thermal behaviour with rapid heating and very high cooling rates, residual stresses are present in components fabricated by this method [27, 28].

As explained previously, LPBF is a layer by layer manufacturing process. The underlying layer that has solidified cools uniformly. When a new layer of powder is deposited on the solid underlayer and heated, the powder melts and expands much faster than the cool underlayer. This expansion of the new layer is then restrained due to the difference in temperature and a compressive stress is developed in the new layer and a tensile stress is present in the underlying layer. During cooling, due to the high cooling rates, the new layer cools down and solidifies first. This quick contraction cannot be accommodated by the underlayer which is still at a higher temperature and hence, tensile stresses originate at the surface and the lower layers have compressive stresses. Residual stress can be decreased by reducing the scan speed and increasing laser power, hatch spacing and layer thickness. Tensile residual stresses are detrimental to the fatigue properties of AM materials because they act as driving forces for crack initiation and also affecting the loading ratio in fatigue [29, 30]. They are also unfavorable because they cause distortion of the component when removed from the substrate.

2.3. Microstructure

The microstructure of a material is the different phases and the morphology of grains present in a material. Determining or controlling the microstructure is a significant step in the life cycle of a material as it highly influences the various properties of the material. In this chapter, a general overview of the microstructure of Ti-64 is presented with a focus on the as fabricated LPBF microstructure. Different heat treatments and their influence on the microstructures is also discussed.

Titanium is an allotrope which means that it can occur in two or more forms in the same physical state. Titanium consists of two crystal structures: α-Ti and β-Ti coexist below the β transus temperature and β-Ti is obtained above the β transus temperature. α-Ti has a hexagonal close-packed (HCP) crystal structure while β-Ti has a body-centered cubic crystal structure (BCC). The occurrence of the above mentioned crystal structure/phases strongly depend on the temperature and cooling rates subjected during the manufacturing processes. Since Ti-64 contains Al, which is an α phase stabilizer along with V, which is a β phase stabilizer, Ti-64 shows a dual phase microstructure at room temperatures [31]. The phase diagram and the different phases with respect to the cooling rate for Ti-64 is shown in Figure 2.3 and Figure 2.4.

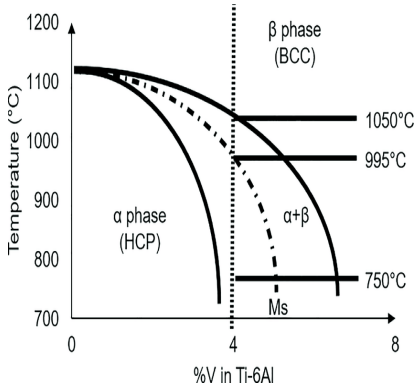


Figure 2.3: Equilibrium phase diagram of Ti-6Al-4V. Reproduced from [32].

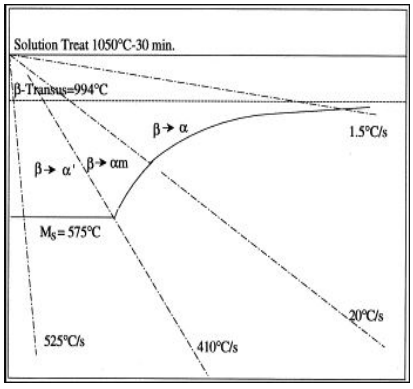


Figure 2.4: Phases as a function of cooling rates. Reproduced from [33].

As seen in the figures, the microstructures obtained are highly dependant on the temperature and cooling rates. In Figure 2.3, 1050°C is the temperature of the solutionizing heat treatment which is the most commonly used temperature. 995°C is the β transus temperature and 750°C is the martensite start temperature. In Figure 2.4, the different microstructures obtained after solutionizing at 1050°C as a function of the cooling rates is shown. When the cooling rate is greater than 410°C/s, a complete α' martensitic microstructure is obtained. When the rate is between 410 °C/s and 20°C/s, an incomplete transformation of α' occurs and when the cooling rate is less than 20°C/s, there is no formation of α' martensite [33]. Hence, very different microstructures are obtained for conventional manufacturing techniques like forged and wrought Ti-64 and additively manufactured Ti-64 because of the vast difference in cooling rates. These phase transformations are driven by two main mechanisms: Reduction of the Gibbs Free energy of the system and reduction of the total surface energy. The change in α or β phase fraction by a process called nucleation and growth until an equilibrium concentration is reached when the Gibbs Free energy is minimum. The movement of atoms is via the process of diffusion. The rate of diffusion is a complex term and depends on a number of constraints like temperature, interface mobility, diffusivity and alloy concentration [34]. The rate of diffusion increases with increase in temperature. Hence, a diffusion driven mechanism is observed for low to moderate cooling rates and a shear displacement as observed in the formation of α' is seen for high cooling rates [35]. With the understanding of these mechanisms and kinetics driving the phase transformations, microstructures are further modified to the user's requirement by different heat treatments and post processing.

2.3.1. Conventional Ti-6Al-4V

The most common conventional method of manufacturing Ti-64 is forged or wrought Ti-64 followed by the required heat treatments. Since heat treatments can be performed at various temperatures, multiple microstructures are possible to obtain. Since the initial microstructure obtained by conventional manufacturing is different from the microstructure obtained by LPBF, the effect of heat treatments are not the same. The most common microstructures are bimodal, equiaxed and lamellar[36]. An example

of the optical micrographs of the different microstructures is shown in Figure 2.5.

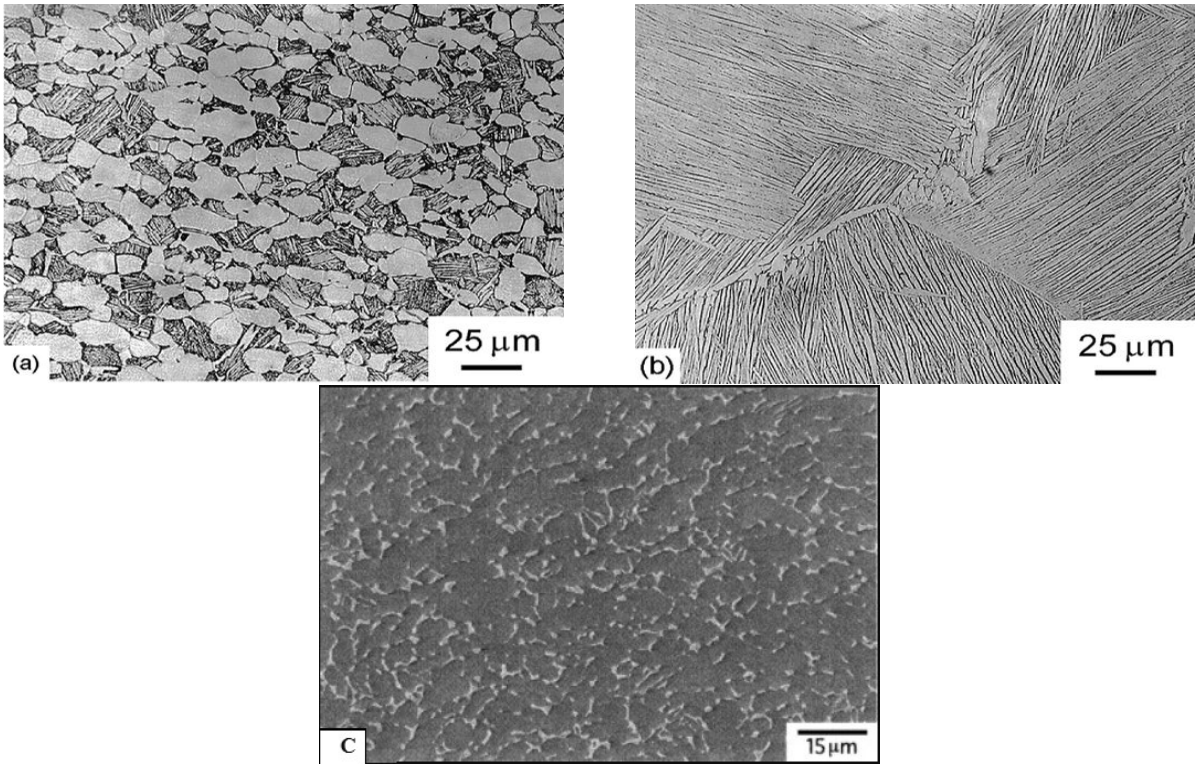


Figure 2.5: Optical micrographs of Ti-64 microstructures: a) bimodal, b) lamellar and c) equiaxed. Reproduced from [37],[38]

In the figure, different heat treatments are done for each microstructure. Figure 2.5a represents a bimodal microstructure which is obtained by a heat treatment called solution treatment and over aging. In this case, Nalla et al heated the sample at 925°C for 1 hour, air cooled using a fan and then aged at 700°C for 2 hours [37]. The resultant microstructure is a bimodal structure with interconnected equiaxed α grains and lamellar $\alpha + \beta$ regions. Figure 2.5b shows a lamellar microstructure which was obtained by heating the sample in vacuum at 1005°C for a duration of 10 to 30 minutes followed by cooling at a rate of 100°C/min in a helium gas atmosphere. The sample was then heated at 700°C for 2 hours in vacuum in order to stabilize the microstructure obtained. The result was an α-lamellar microstructure with a colony size of 500μm with a width of the lamellae laths around 1 to 2 μm.

2.3.2. LPBF Ti-6Al-4V

As-fabricated

As explained in the previous chapter, a characteristic of the LPBF process is it's large temperature gradient and very high cooling rates, in the order of 10^5 K. Another significant characteristic is it's complex thermal history owing to its directional nature

and multiple cycles of heating and cooling. This gives the as-fabricated LPBF Ti-64 sample a unique microstructure. Upon cooling below 1660°C, solidification of the BCC β phase begins. This takes place on the substrate during the first cycle or on the previous layers during subsequent cycles. Thus, a directional behaviour is obtained along the build direction/along the maximum thermal gradient which results in columnar β grains. These columnar grains might also be orientated at an angle due to melt pool displacement[39].

Upon further rapid solidification from the β-transus temperature, a new solid phase is formed. As the temperature falls below the martensite start temperature, there is not enough time for diffusion and a shear type,diffusion-less transformation from the BCC β phase to a meta-stable α' phase takes place. This martensite is acicular in nature and is formed within the prior β grains[40]. This α' martensite has a high density of dislocations and twins to accommodate the strains associated with the transformation. The crystallographic orientation relationship between the BCC and HCP phases is given by Burger's relationship

$$(110)_\beta || (0002)_\alpha$$
$$[1\bar{1}1]_\beta || [11\bar{2}0]_\alpha$$

This phase transformation has 12 hexagonal variants with the development of lamellae within the prior beta grain boundaries [31]. A typical micrograph of as-fabricated LPBF Ti-64 is shown in Figure 2.6.

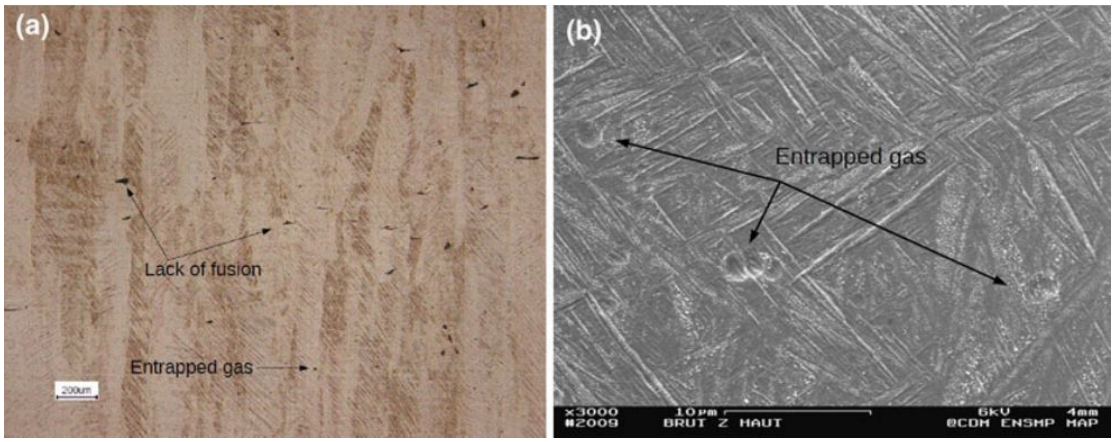


Figure 2.6: As fabricated LPBF Ti-64 a) Optical micrograph showing columnar grains b) SEM image showing acicular martensite. Reproduced from [41].

Figure 2.6a shows the side view of the sample at a low magnification. A clear image of columnar grains is seen growing along the direction of the thermal gradient. These are recognized as the prior-β grains within which the martensite grows. The top view of the sample would show a chess board pattern due to the alternating pattern of the scan history [41]. The width of the square in the chess board pattern and the width of the columnar grain is directly a function of the hatch spacing of the LPBF process[42]. Figure 2.6b shows a magnified image under the SEM. This clearly reveals elongated acicular needles of α' martensite. In both the images, the lack of fusion pores and entrapped gas molecules are also seen clearly due to the mechanisms explained previously. The detrimental effects of the as fabricated microstructure on the

fatigue initiation phase is explained in detail in section 2.6.

Post-processing heat treatments

As the as-fabricated microstructure is dominated by acicular martensite which severely reduces the ductility of the sample, post processing heat treatments are usually done to achieve a more favourable microstructure and hence, properties. In general there are three types of heat treatments, stress relief, annealing below the β-transus temperature also called low temperature annealing and annealing above the β-transus temperature also called high temperature annealing.

Stress relief

As explained in the previous chapter, as fabricated LPBF components have high amounts of residual stresses due to large thermal gradients that reduces the resistance to crack propagation. To overcome this, a heat treatment known as stress relief is performed. As the residual stresses originate due to thermal gradients, stress relief heat treatment involves heating the sample at a moderate temperature for a sufficiently long period. The temperature chosen must not be too high such that it induces a significant change in microstructure. Hence, the main aim of performing the stress relief heat treatment is to eliminate residual stresses and instigate a decomposition of the α' martensite. Ter Haar et al studied the effect of different temperatures and holding times on the microstructural changes and came up with an ideal temperature of 550°C to 610°C for a duration of 1 hours such that there are minimal changes in the microstructure while reducing the residual stresses [43]. Microstructural changes are observed only for holding times close to a few hours due to the slow kinetics of phase transformation.

Annealing

As acicular α' martensite is detrimental to the mechanical properties of Ti-64, annealing heat treatments at sufficiently high temperatures are required. Annealing at temperatures below the β-transus temperature is called sub transus annealing and annealing at temperatures over β-transus temperature is called β annealing or super transus annealing. T_0 is defined as the temperature above which α' martensite is obtained upon rapid cooling [35]. This was determined to be close to 900°C. A number of annealing temperatures have already been investigated with different cooling rates [44, 30, 34, 45, 29, 46, 47, 41, 48, 49]. The main aim of annealing below the β-transus temperature is to decompose the martensitic needles and improve the ductility of the material. Sallica-Leva et al proposes a mechanism for the decomposition of α' martensite as follows: at the grain boundaries of the martensitic needles, β phase precipitates and since the α' phase is supersaturated in Vanadium, there is a diffusion of Vanadium from the α' to the β phase to reduce the free energy of the system [44]. Eventually, the α' depleted of V atoms transforms to the α phase [50]. This is in

contradiction to the mechanism proposed by Vrancken et al and Zhang et al that says there is nucleation of α phase at the α' boundaries and there is diffusion of vanadium atoms leading to the evolution of β phase at the α phase boundaries [51]. However, there is no proof of the nucleation of the α phase at the α' boundaries.

Different cooling rates can be achieved by furnace cooling (FC), air cooling (AC) or water quench (WQ). Heating well below T_β, a dual phase lamellar $\alpha+\beta$ microstructure is obtained by decomposing the acicular α' needles. When temperatures close to T_β are reached, fragmentation and globularization of α' at the twinning sites take place leading to an equiaxed microstructure [34]. Below T_β, the influence of temperature plays a more significant role than the influence of cooling rate or residence time on the microstructural changes. The volume fraction of the β phase increases as T_β is approached. At 780°C, an α-fraction of 87% is observed, reducing to 73% at 850°C and further decreases to 23% at 950°C [52],[53]. The increase in maximum temperature results in an increase in α grain size and rise in β phase fraction. The reduce in α phase fraction is due to the minimization of Gibbs Free Energy as explained earlier. However, there is not significant amounts of grain growth observed below T_β as there are two phase hindering each other's growth. Hence, below Tβ, the influence of maximum annealing temperature plays a more important role when compared to the residence time and cooling rate [42]. The influence of cooling rate below T_β is seen in the study done by Ter Haar et al as shown in Figure 2.7.

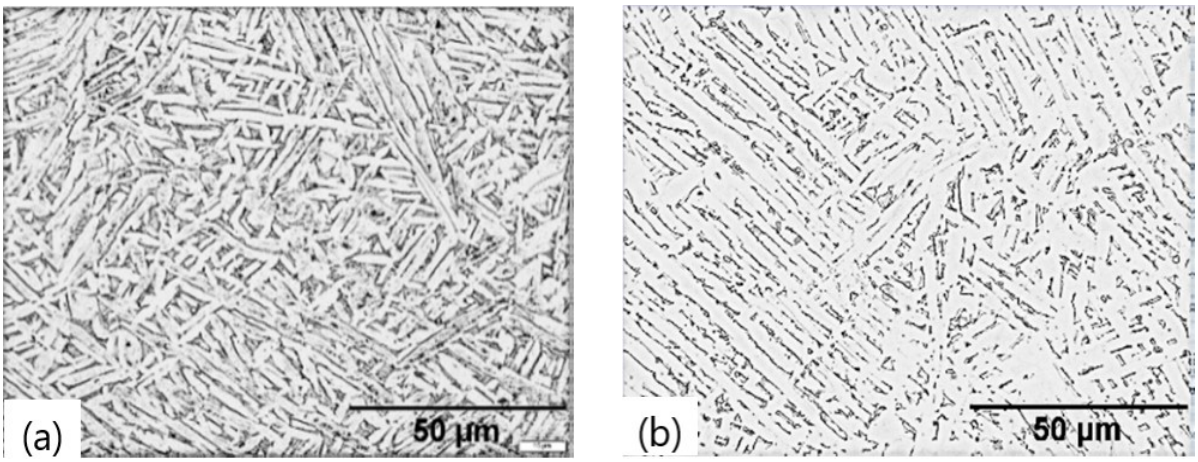


Figure 2.7: Microstructure after annealing at 870°C followed by a) AC, b) FC. Reproduced from [34]

It can be seen from Figure 2.7 that a lamellar microstructure is obtained. The microstructure obtained from furnace cooling has a greater grain width than the air cooled sample. Ter Haar et al measured the size and observed an α grain width of 1.5-3.5μm for the FC sample and a width of 1.5-2.5μm for the AC sample. This difference in grain size is due to the slower cooling rate in FC allowing more time for diffusion to take place.

Beta annealing or super transus annealing is usually performed around 20°C over T_β. At these temperatures, the α phase is completely converted to β phase. This results in unhindered grain growth of β. As the amount of α phase decreases, cooling

rate and residence time becomes an increasingly significant factor on the evolution of the microstructure. The residence time determines the β grain size which in turn determines the size of the α colonies when cooled which affects the properties of the material. This is shown in Figure 2.8. As seen in the figure, the α colony sizes are larger for the sample held for 20 hours at 1040°C than the sample held at 1020°C for 2 hours. This is due to the coarsening of the β grains over T_β. The maximum size of the α colony is limited by the size of the β grain within which it nucleates.

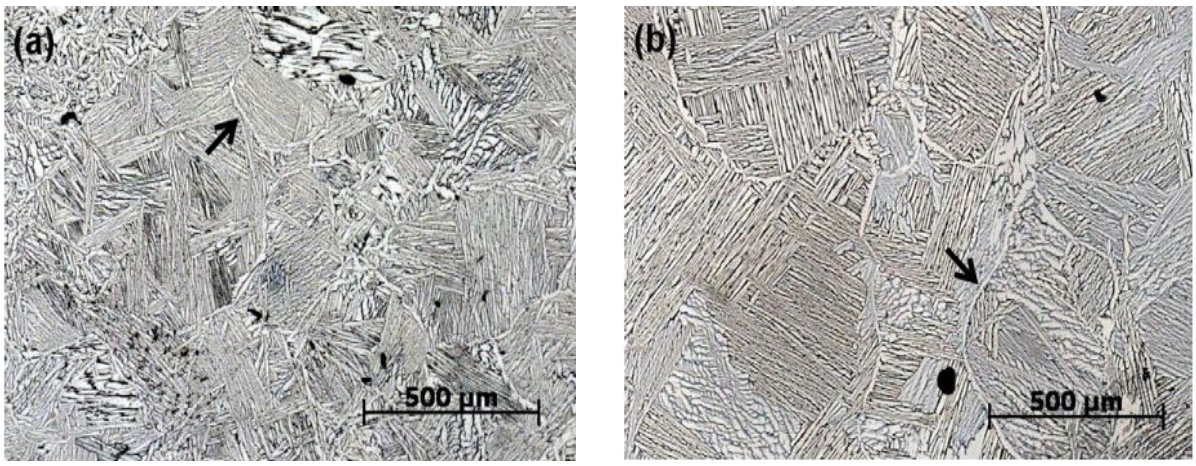


Figure 2.8: Microstructure showing the difference in α colony size for different residence times. a) 1020°C for 2h, b) 1040°C for 20h. Reproduced from [42]

The other important parameter, cooling rate determines the morphology and dimensions of the α phase [54],[31]. When high cooling rates are reached, sufficient undercooling is achieved which leads to numerous α nucleation points which results in small α colonies and fine spacing between the α plates. In general, from β annealing, furnace cooling results in a lamellar microstructure, air cooling leads to α-Widmanstätten or basket weave microstructure and water quenching leads to an acicular α' martensite [42],[19].

Since a bimodal microstructure provides a good balance in strength and ductility, it is believed to be a useful microstructure to obtain. In the case of conventionally manufactured Ti-64, this is possible by thermo-mechanical processing. As mechanical processing is not possible in the case of LPBF Ti-64, studies have been done to come up with a two step annealing process to obtain the bi-modal structure. Ter Haar et al heated the sample at 910°C for 8 hours followed by WQ and then heated the sample at 750°C for 2 hours followed by AC. As the initial temperature was above T_0, a martensitic microstructure was obtained after WQ. The martensite was decomposed when heated again at 750°C resulting in a final microstructure of bimodal equiaxed primary α and lamellar secondary $\alpha + \beta$ [34]. Kumar et al heated the sample at 920°C for 30 minutes followed by FC and held at 700°C for 2 hours followed by AC. This resulted in a bimodal structure with lenticular α plates with β phase [55].

In order to avoid the extra step of heat treatments, studies have been done to optimize the processing parameters of LPBF to obtain a bimodal microstructure in the as fabricated sample. Xu et al and Simonelli et al have produced as fabricated bimodal

structures by in situ decomposition of α' by controlling different parameters in LPBF. The main parameters were focal offset distance, hatch spacing and pre heating of the substrate bed to avoid large thermal gradients. A close hatch spacing would result in overlap of melt pool over each cycle leading to a more uniform heating [56],[57],[58]. Although the microstructure is favourable, varying the process parameters reduces the overall efficiency of LPBF. Xu et al says that controlling the thermal gradients with high accuracy would put a constraint on the overall size of the component to be manufactured. Therefore, as of today, post process heat treatments are still the way to move forward.

Hot Isostatic Pressing

Hot Isostatic Pressing (HIP) treatment is the process of subjecting the component to a uniform pressure at elevated temperatures in inert atmospheres such as Argon. An inert atmosphere is required because Ti-64 is susceptible to oxidation at high temperatures. This treatment is done with the aim of eliminating porosity and achieving highly dense components. The HIP process can accommodate pressures and temperatures as high as 2000 bar and 2000°C. For Ti-64 however, temperatures in the range of 900 to 940°C and pressures in the range of 120 MPa for a duration of 2 to 3 hours are utilized [59]. This results in a component with a relative density of over 99.9%. The elimination of porosity results in significant improvement in the fatigue properties of the material. In addition to the elimination of porosity, a decomposition of the martensitic phase is seen due to the high temperatures and holding times, increasing the ductility of the material [30].

2.4. Mechanical properties

The tensile properties of the material is influenced by the microstructure and hence, in a way by the processing parameters of the LPBF process. As the effect of heat treatments on mechanical properties of LPBF Ti-64 is a highly studied, subject, it is out of the scope of this report to provide a comprehensive review on the effect of different heat treatments of the mechanical properties. Hence, a general summary of the tensile properties for a few heat treatments is given in this section.

To maintain continuity, the tensile properties for some of the heat treatments described in Figure 2.3.2 is chosen. The tensile properties are shown in Table 2.1.

Table 2.1: Tensile properties of as fabricated and heat treated LPBF Ti-64

Sample	Heat treatment	Yield strength (MPa)	Tensile strength (MPa)	Final elongation (%)	Reference
As fabricated	-	1150	1250	<9	[11]
Sub transus HT	850°C, 2h, FC	955	1004	13	[42]
Super transus HT	1020°C, 2h, FC	760	840	14	[42]
Duplex anneal	910°C, 8h, WQ/ 750°C, 4h, FC	900	950-980	16-20	[34]
HIP	920 °C, 103 MPa, 4h	920-1000	1000-1100	12-18	[60]
Wrought	Mill anneal	790	870	18	[45]

The table shows the yield strength, ultimate tensile strength and the elongation at failure for the as fabricated and heat treated samples. A comparison with conventionally manufactured Ti-64 is also shown in the table. The tensile properties are dependant on the microstructures including the phases, grain size, direction of the columnar β grains and also the defects in the component. The as fabricated sample has the highest strength with a value around 1250 MPa but the high strength comes at the cost of ductility. The as fabricated sample gets its high strength from the meta stable acicular α' martensite and also due to a high density of dislocations resulting in dislocation hardening [61]. Stress relief heat treatment which is usually done at temperatures below 800°C do not affect the tensile properties significantly because the low temperatures cannot induce any grain coarsening within a short time period. However, residual stresses are removed which great influences the fatigue properties of the material. Heat treatment below T_β at 850°C leads to decomposition of martensite and a microstructure dominated by α phase in the form of needles with a low volume fraction of the β phase. The decomposition of martensite and the presence of β phase leads to an increase in ductility although this comes at the cost of yield and tensile strength. Heat treatment at a sub transus temperature results in decomposition of α' martensite and evolution of α and β phases by diffusion. At 850°C, the microstructure is dominated by the α phase present as needles. This morphology results in retaining the strength around 1000 MPa while the presence of the β phase provides an increased ductility around 13%. When heat treated above in the super transus temperature range, there is rapid evolution of the β phase as explained in Figure 2.3.2. This results in colonies of α phase when cooled to room temperature. The size of the α colonies is dependant on the residence time above T_β. As the BCC phase is more ductile than the HCP phase, heat treatment above T_β results in lower strengths and increased ductility as seen in Table 2.1. It was also observed that coarser α phase and larger colony sizes decreased the strength of the material [42]. When the material was duplex annealed as studied by Ter Haar et al, it showed a significant increase in ductility, reaching 16-20% due to the presence of a bimodal microstructure containing equiaxed α phase in a matrix of lamellar $\alpha + \beta$ phase [34]. In the case of HIP treatment, a high ductility similar to Ti-64 manufactured by conventional methods is obtained mainly due to the elimination of pores which act as stress concentrators and crack initiation points. The strength of the HIPed sample also reduces when compared to the as fabricated sample due to the decomposition of the martensitic phase at sufficiently high temperatures [60, 45].

Additively manufactured Ti-64 shows anisotropy in tensile properties due to the directional behaviour of the process. An example of anisotropy in tensile properties is shown in Figure 2.9.

Qiu et al studied the tensile properties of the as fabricated and HIPed samples in two orientations, vertical/longitudinal and horizontal/flat [60]. In the vertical orientation, the columnar grains are present parallel to the direction of loading whereas in the horizontal direction, the columnar grains are present perpendicular to the loading direction. It is seen from Figure 2.9 that HIP treatment improves the ductility of the material significantly. It is also seen from the figure that in both the as fabricated and HIPed condition, the vertically oriented sample shows lower strength and higher

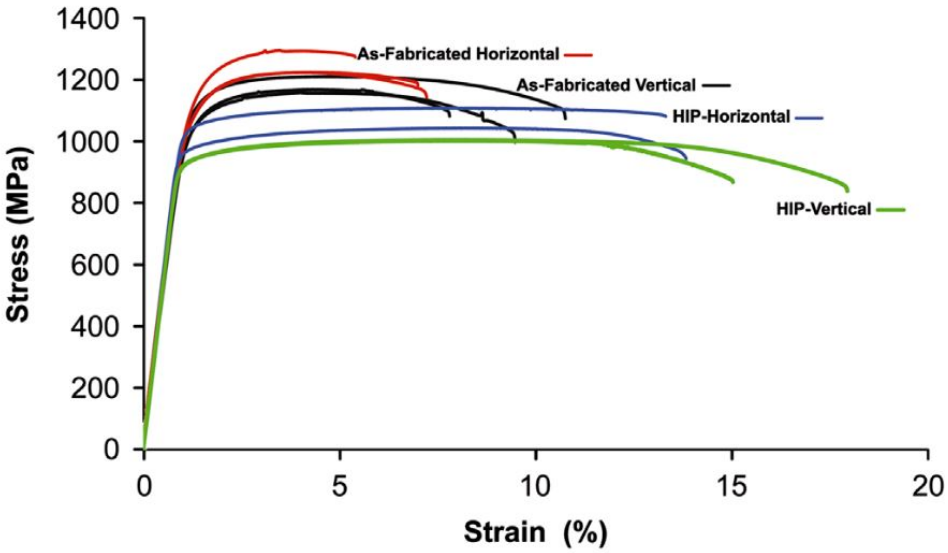


Figure 2.9: Tensile curve showing anisotropy in properties. Reproduced from [60]

ductility than the horizontally oriented sample. This is in agreement with studies done by other researchers [62]. Simonelli et al argue that the vertical samples show lower strength because of the larger number of layers which increases the probability of having incomplete interlayer bonding. However, it is seen from the figure that even after HIP treatment which leads to a 99.9% dense material, anisotropy exists which makes the orientation of the columnar prior β grain the most significant factor regarding anisotropy in tensile properties.

2.5. Introduction to fatigue

Fatigue is defined as the failure of a material below its tensile strength when subjected to repeated cyclic loading. Fatigue could be detrimental to a component/structure as it could lead to sudden failure of the material, as was experienced in the 19th century. To describe fatigue loading, different parameters are used. An illustration of these parameters is shown in Figure 2.10.

The different parameters to describe fatigue loading are:

- σ_{max}: The maximum stress in a loading cycle.
- σ_{min}: The minimum stress in a loading cycle.
- σ_{mean}: The mean stress in a loading cycle.
- $\Delta\sigma$: The stress range in a loading cycle. $\Delta\sigma = \sigma_{max} - \sigma_{min}$.
- $\Delta\sigma_a$: Stress amplitude of the loading cycle. $\Delta\sigma_a = \frac{\Delta\sigma}{2}$
- R: The load/stress ratio in the stress cycle. $R = \frac{\sigma_{min}}{\sigma_{max}}$

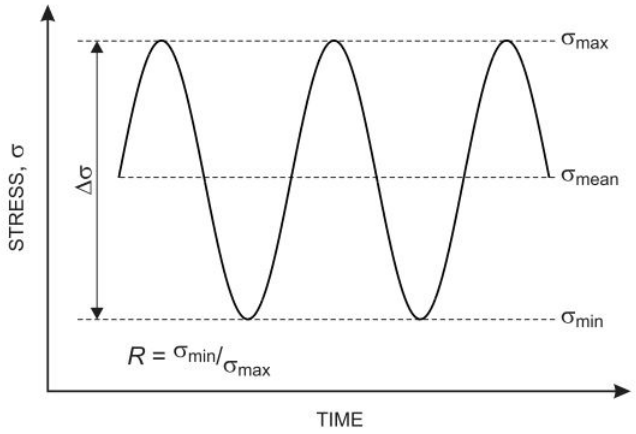


Figure 2.10: Parameters to describe fatigue loading. Reproduced from [6]

The fatigue life of a component is comprised of crack initiation, crack propagation and final failure. Crack initiation usually takes place in the surface of the component at defects or other stress concentrators. Crack initiation is a complex mechanism involving slip bands and slip systems while the orientation of the grain boundaries plays the role of a barrier to further growth of the micro crack. Due to the large number of variables in the mechanism, crack initiation is tedious to analyze and hence, this study focuses on the crack propagation phase.

Crack propagation

Paris et al utilized a concept known as Linear Elastic Fracture Mechanics (LEFM) to study and describe crack propagation in a material [63]. If the loads on a material induces little plastic deformation and the size of the plastic zone is small, the material largely behaves in an elastic manner. In this case, LEFM can be used to study the material. When the loads are high and the size of the plastic zone is large, LEFM cannot be used and instead a concept known as Elastic Plastic Fracture Mechanics (EPFM) is utilized. In LEFM, there are three modes of failure which is shown in Figure 2.11.

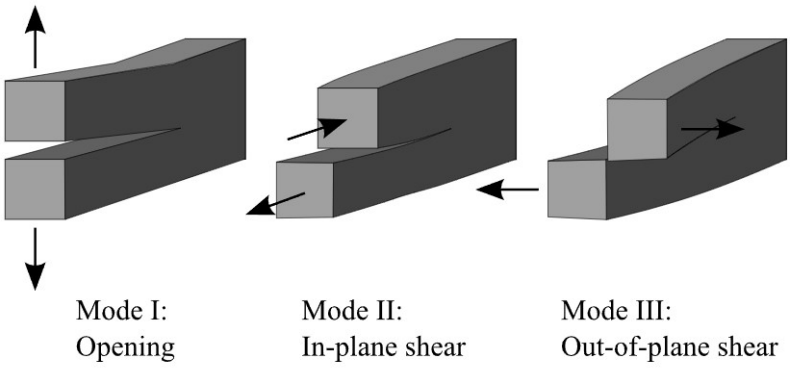


Figure 2.11: LEFM fracture modes. Reproduced from [64]

Mode I failure type which is opening is the most frequent type of failure. Cracks

have a tendency to align themselves to propagate with a mode I type loading [65].

K_t is defined as the stress concentration for notches while K_I is defined as the stress intensity factor for cracks. K_I is calculated for a given stress level using Equation 2.2 [6].

$$K_I = C\sigma\sqrt{\pi a}.f(\frac{a}{W}) \tag{2.2}$$

where C is a material constant, a is the crack length and $f(\frac{a}{W})$ is a geometric function. Using the above equation, all the parameters in Figure 2.10 can be expressed in terms of stress concentrations, K. The different stages can basically be classified into three parts, crack initiation, crack growth and final failure. These stages can be shown in a fatigue crack growth graph which has the crack growth rate, $\frac{da}{dn}$ as the abscissa and the stress intensity range, ΔK as the ordinate. This is shown in Figure 2.12.

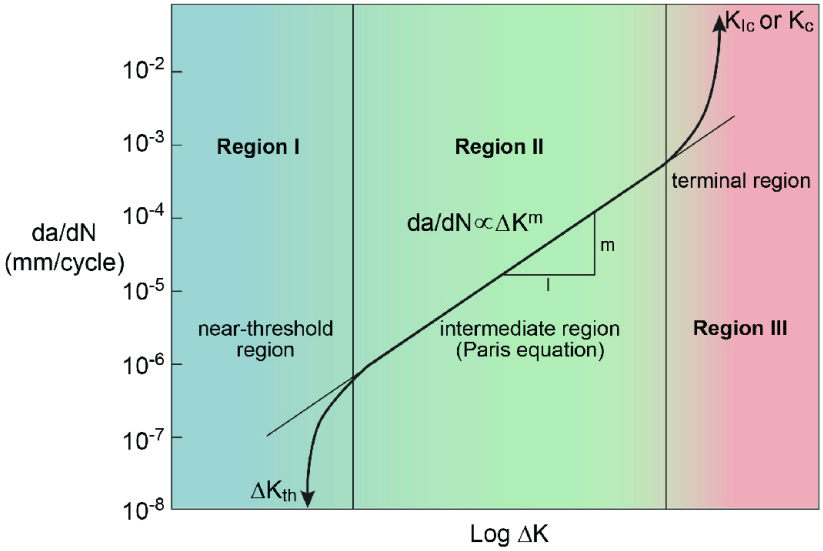


Figure 2.12: Schematic of the $\frac{da}{dn}$ versus ΔK curve showing the different stages. Reproduced from [66].

As seen in the figure, the first region is characterized by a parameter called the fatigue threshold. Fatigue threshold, ΔK_{th} is the stress intensity range above which the crack begins to propagate. In this region, the fatigue crack growth rate (FCGR) is is very low and crack lengths are very small in the nano and sub-micron scales. The crack lengths are in the scale of microstructural features and hence, the microstructure of the materials plays a very important role in this region. The factors affecting the fatigue threshold value is further explained in the upcoming sections.

With increasing stress intensity range, the crack growth rates increases and in the second region, the growth rate usually follows a power law function. In this case, the figure shows the Paris equation which is given as

$$\frac{da}{dn} = C(\Delta K)^m \tag{2.3}$$

where, m is a constant that represents the slope of the linear portion in the second stage. Higher the value of m, the steeper the line. Since the above equation holds true only for the second stage of the crack growth rate curve, the second stage is called the Paris region. Although other equations have been developed to represent the entire curve over all three regions such as Forman's equation, Paris law is the most widely used equation [6]. The third region or terminal region as shown in Figure 2.12 is reached when the stress intensity range is close to the fracture toughness of the material in the plane strain or the plane stress state. In this region, the crack growth rates increases asymptotically leading to rapid failure of the structure/component.

In the following subsection, the fatigue properties of LPBF Ti-64 is discussed with a focus of the near threshold fatigue.

Crack closure

Crack closure is the phenomenon by which the crack flanks are in contact with each other and closed before the minimum load is reached during cyclic loading. Applying the concept of LEFM, the stresses in Figure 2.10 are now represented as stress intensity factors as shown in Figure 2.13.

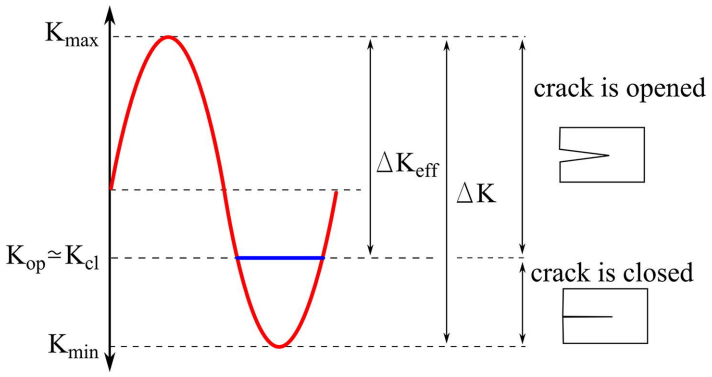


Figure 2.13: Schematic showing ΔK_{eff} as a result of crack closure. Reproduced from [67]

As seen in the figure, the crack is open over a certain stress intensity factor, K_{op} or K_{cl} and closed below that value, before reaching K_{min} represented by the blue line. Hence, effectively a stress intensity range, Δk_{eff} is only acting on the material. Crack closure occurs due to three different mechanisms, plasticity induced crack closure, roughness induced crack closure and oxide induced crack closure. The illustrations of these mechanisms is shown in Figure 2.14.

In the case of plasticity induced crack closure, crack closure occurs due to the residual stresses and out of plane material flow forming a wedge like wake in front of the crack tip during the unloading cycle. Ahead of the crack tip there exists a large elastic zone within which there are smaller monotonic and cyclic plastic zones when K_{max} exceeds the yield strength of the material. During the unloading cycle, due to the elastic spring back, there exists a compressive residual stress ahead of the crack tip and along the plastic wake which closes the crack before the minimum load is reached

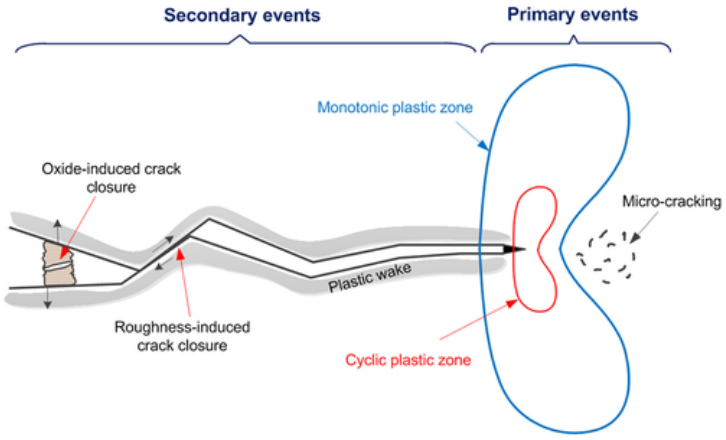


Figure 2.14: Schematic showing different mechanisms of crack closure. Reproduced from [68]

[69].

The closure of the crack due to the microstructurally rough crack flanks containing asperities is called roughness induced crack closure. During unloading, due to the contact of these asperities, the crack is closed before the load reaches it's minimum. During mode I macroscopic loading of the material, locally in the crack, there is mode II loading as seen in Figure 2.14. This leads to the closure of the crack [70, 71].

Oxide induced crack closure is usually witnessed in harsh environments. OICC is caused due to the wedging of the crack by oxide formation or debris leading to premature crack closure as seen in Figure 2.14. Therefore, OICC is more prominent at high temperatures or at moist atmospheres [72].

2.6. Near threshold fatigue properties of LPBF Ti-6Al-4V

In this section, the work by Leuders et al, Edwards et al, Cain et al, Kumar et al, Tarik Hasib et al and Becker et al is summarized and the factors affecting the results in the near-threshold region is discussed [29],[73],[48],[55, 74],[75],[76].

Leuders et al studied near threshold FCGR on two orientations, vertical and edge. The tests were conducted at a stress ratio of R=0.1. The authors tested the as fabricated, heat treated and HIPed samples. The authors observed a threshold stress intensity range of 1.7 MPa$\sqrt{m}$ for the as fabricated condition, around 6.1 for the beta annealed condition and 3.7 for the HIPed sample in the vertical orientation. It was observed that the edge orientation showed lower threshold values compared to the vertical orientation. The authors say that the beta annealed sample shows higher threshold values due to great grain growth over beta transus temperature and the low threshold value in the as fabricated condition is attributed to the martensitic phase and not the presence of defects and pores. They say that residual stresses play a more

significant role than porosity in the near threshold region. This could be due to the effect of residual stresses on the load ratio. No explanation was given regarding the anisotropy of the results in the near threshold region. It should also be noted that since a low R value of 0.1 was chosen, crack closure effects should have been prominent which were also not considered [29].

Edwards et al studied the fatigue crack growth rates of the sample in three orientations, vertical horizontal and edge at a stress ratio of 0.1. For all three orientations, a threshold stress intensity range around 6 MPa$\sqrt{m}$ is seen, showing little anisotropy. No post processing heat treatments were performed and only the as fabricated condition was studied. The higher value of the threshold value could be because the authors did not go until the crack growth rate of 10^{-10} m/cycle as per standards but stopped at a much higher crack growth rate. Once again, the effect of crack closure was not considered at a low value of stress ratio [73].

Cain et al studied the near threshold fatigue crack growth rate in three orientations, vertical, horizontal and edge although the threshold value was not determined. In addition to the as fabricated condition, stress relief and annealed conditions were also studied. Details regarding the stress ratio used in the experiments was not mentioned. It was observed that in the as fabricated condition, the horizontal sample showed the highest resistance to crack growth compared to the other two orientations and this anisotropy was reduced in the stress relief and annealed conditions. The authors say that the anisotropy in the as fabricated condition is caused due to the anisotropy of the residual stresses and not due to the microstructure [48].

Kumar et al studied the near threshold fatigue in the vertical and horizontal orientations under the as fabricated and four heat treatment conditions. Two of the heat treatments were below the beta transus temperature and the other two heat treatments were above the beta transus temperature. A stress ratio of 0.1 was maintained and a threshold value close to 5.5 Mpa$\sqrt{m}$ was reported which is close to the threshold of the conventionally manufactured samples. Upon heat treatments, the threshold value was observed to increase to values in the range of 7.1 to 8 Mpa$\sqrt{m}$. Again, the higher threshold values for the as fabricated condition could be because the authors considered the threshold value as the stress intensity range at a crack growth rate of 2x10^{-9} m/cycle and not 10^{-10} m/cycle according to the standards. The authors did not observe any significant anisotropy in the two orientations. Regarding the microstructure, the authors say that the alpha colony size influences the threshold values and the alpha lath sizes influences the crack growth rates in the near threshold region. Once again, no information regarding crack closure is provided [74],[55].

Becker et al investigated the near threshold fatigue crack growth rates in the vertical, horizontal and edge orientations. In addition to the as fabricated condition, the stress relief condition was also studied. Multiple stress ratio values between 0.1 and 0.9 were chosen. A threshold stress intensity range of around 1.6 MPa$\sqrt{m}$ in the as fabricated condition was obtained regardless of the orientation. In the case of the stress relieved condition, a threshold value of 2.5 to 3 MPa$\sqrt{m}$ was seen at lower stress ratios while the threshold values dropped close to 1.7 to 2 MPa$\sqrt{m}$ at high stress ratios. The low threshold values in the as fabricated condition was attributed to the marten-

sitic phase and a transgranular quasi-cleavage fracture mechanism. Anisotropy in the values were attributed to the microstructure in front of the crack tip. The authors argue that crack branching near the crack tip occurs at the alpha laths and in the larger scale, it occurs along prior beta grain boundaries. The authors attribute the increase in threshold values at lower stress ratios to the phenomenon of roughness induced crack closure. The presence of residual stresses in the as fabricated sample prevented the occurrence of crack closure at lower stress ratios which shifted the FCGR values to higher stress ratio values [75].

Tarik Hasib et al studied the FCGR in the near threshold region for vertical, horizontal and 45°orientations. In addition to the as fabricated condition, three heat treatment conditions were also studied. The first two are annealing below the beta transus temperature along with HIP while the third heat treatment was performed above the beta transus temperature. A stress ratio of 0.1 was chosen for the tests. The results obtained by the authors is shown in Figure 2.15 [76].

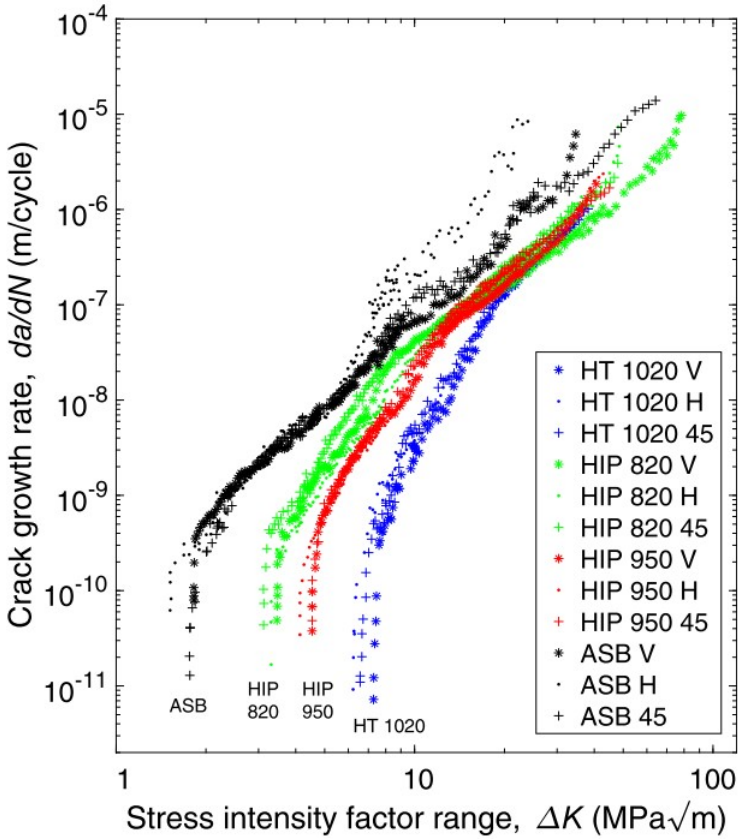


Figure 2.15: FCGR curves obtained by Tarik Hasib et al [76]

As seen from the figure, the as fabricated sample showed a threshold value of 1.5 to 1.8 MPa$\sqrt{m}$, the sample HIPed at 820°C showed a threshold close to 3.3 MPa$\sqrt{m}$, the sample HIPed at 950°C has a threshold value of 4.5 MPa$\sqrt{m}$ and the sample annealed at 1020°C showed a threshold close to 7 MPa$\sqrt{m}$. It can be seen that the orientation of the samples is not significant to the threshold values. Regarding the microstructure, the authors mention that with an increase in grain size, there is an

increase in the threshold values. The effect of crack closure was studied and a minor roughness induced crack closure is observed.

Factors influencing near threshold fatigue

Based on the literature available on near threshold fatigue of LPBF Ti-64, there are four factors that play an important role in this region.

- Residual stresses
- Porosity and surface roughness
- Load/stress ratio
- Microstructure

As mentioned previously, there exists tensile residual stresses on the surface of a component fabricated by LPBF. These residual stresses act as driving forces for crack initiation and as a result, the threshold value is reduced. Tensile residual stresses also prevents crack closure, thus ”raising” the value of stress ratios. Additionally, based on the build direction, scan pattern and orientation, there could exist an anisotropy in residual stresses leading to anisotropy of properties in the near threshold fatigue region. The presence of these defects are detrimental to the mechanical properties of the material. Specific to near threshold fatigue, porosity and surface roughness act as crack initiation sites and hence reduce the fatigue threshold value of the material.

Load ratio plays an important role in the near threshold fatigue properties of the material. Generally, it can be said that increasing the load ratio decreases the threshold value and increases the fatigue crack growth rate of the material but the influence could vary for different materials. This is mainly due to the presence of crack closure effects playing a role in the lower load ratios. This is seen in Figure 2.16.

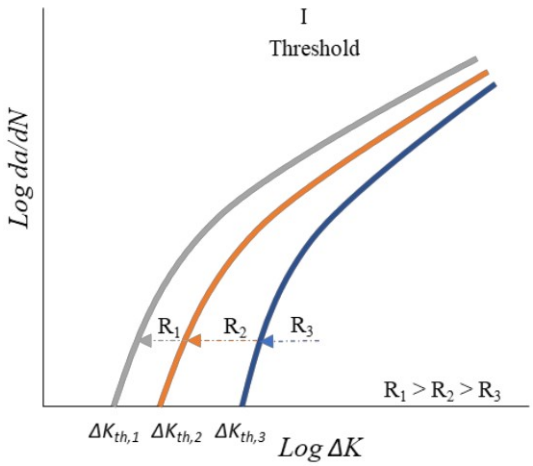


Figure 2.16: Effect of load ratio in the near threshold fatigue region. Reproduced from [77]

While the previously mentioned factors are extrinsic in nature, microstructure is

an intrinsic feature that greatly influences the near threshold region properties of the material. In the absence of porosity and surface roughness, crack initiation occurs due to the formation of persistent slip bands as a result of the repeated slip. These slip bands leads to the formation of inclusions and as a result a crack initiates at a rate of 10^{-9} m/cycle. At this length scale, the microstructure plays an important role because the slip bands move along the crystallogrpahic planes [78]. Based on the available literature, the most significant microstructural features are alpha lath/colony sizes and the prior beta grain boundaries. The effect of alpha colony/lath sizes is schematically explained by Galarraga et al in Figure 2.17.

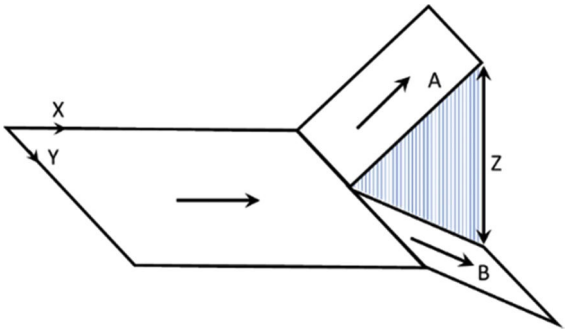


Figure 2.17: Schematic showing the influence of microstructural features on fatigue crack propagation. Reproduced from [79].

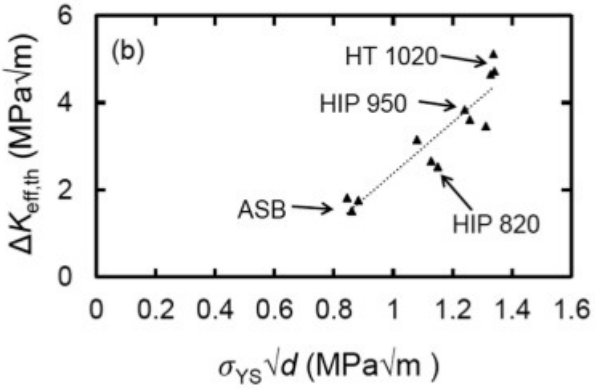


Figure 2.18: Effect of microstructure size on fatigue threshold. Reproduced from [76].

As already mentioned, the crack propagates through specific crystallographic planes and Galarraga et al say that when a crack propagating through a plane comes in contact with microstructural features having different slip planes, the crack bifurcates across the two features. In order for the crack to move forward, it has to travel a distance ”z” as shown in the figure in an unfavorable slip plane. Hence, greater the distance ”z”, greater the fatigue crack propagation resistance and threshold values. In the context of Ti-64, these microstructural features are realized as alpha colonies and greater the colony size, greater the distance the crack has to propagate in unfavorable directions, thus increasing the fatigue threshold values of the materials [79]. Tarik Hasib et al also observed an increase in the fatigue threshold of the material with increasing microstructure sizes of alpha colonies and laths. This is clearly seen in Figure 2.18. Beta annealed Ti-64 shows greater threshold values because above the beta transus temperature, there is unhindered beta grain growth and when cooled to room temperature, the alpha colonies and laths are greater in size.

Another important microstructural feature that plays an important role in the near threshold region is the prior beta grain boundaries. The orientation of these grains leads to anisotropy in the propagation of the crack. When the sample is orientated in the horizontal orientation, the PBG boundaries are orientated perpendicular to the crack propagation direction while the scan layers are orientated parallel whereas in the vertical direction, the PBG boundaries are parallel to crack propagation direction and the scan layers are perpendicular. When PBG boundaries are perpendicular to the crack, the crack propagates across the minor axis of the PBG whereas in the other

orientation, the crack starts branching along the PBG boundaries leading to increased crack tortuosity.

Near threshold fatigue testing

Near threshold fatigue testing is generally done according to the ASTM standard E647-Standard Test Method for Measurement of Fatigue Crack Growth Rates [80]. According to the standard, the standard specimen shapes are either a compact tension (CT) specimen, Middle tension (MT) specimen or Single Edge Notch Tension (SENT) specimen. Fracture mechanics is used to calculate the stress intensities and FCGR curve is to be plotted and the threshold stress intensity range (ΔK_{th}) is to be selected as the stress intensity value at which the crack growth rate is 10^{-10} m/cycle. In order to avoid the effect of crack closure, high stress ratios are to be employed and for this a type of testing called constant K_{max} tests are used. An illustration of the K_{max} type of tests is shown in Figure 2.19.

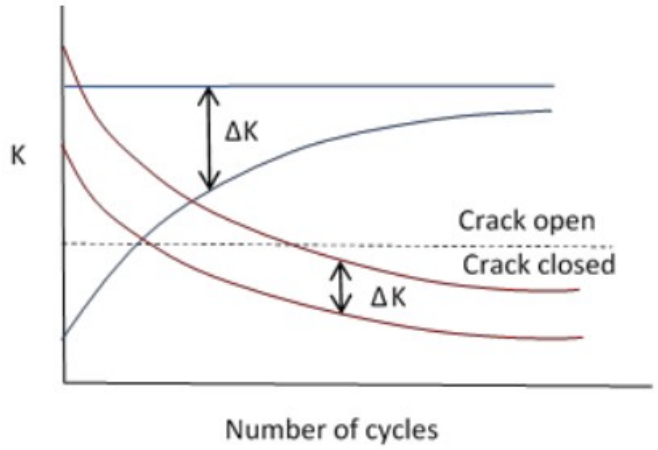


Figure 2.19: Illustration of the R constant (red) and constant K_{max} (blue) tests. Reproduced from [77].

It can be seen from the blue line on the figure that the maximum stress intensity value is a constant during the entire duration of the test. By selecting a certain R and ΔK value, the K_{max} value is calculated using Equation 2.4. K_{min} on the other hand is to be incremented gradually during the test to decrease the ΔK value until the fatigue crack growth rate is 10^{-10} m/cycle. The K_{min} at each point is calculated using Equation 2.5 where K_0 is the initial K_{min}, C is called the stress intensity gradient, a is the instantaneous crack length and a_0 is the initial crack length.

$$K_{max} = \frac{\Delta K}{1 - R} \tag{2.4}$$

$$K_{min} = K_0 exp(C(a - a_0)) \tag{2.5}$$

Ghorbanpour et al employed an interesting method to study the near threshold region of inconel 718 using a single edge notched bending (SENB) specimen following the ASTM E399 standard [81],[82]. The authors however reached a crack growth rate of 10^{-9} m/cycle to decide the threshold value.

Before starting the fatigue test, a pre-fatigue loading is performed to initiate a crack from the notch. According to the ASTM standards, the K_{max} when ending the pre-fatigue test should be lower than the starting K_{max} for the actual near threshold testing.

2.7. Conclusions

Based on the information gained from the literature review, the following conclusions were made.

- Additive manufacturing and LPBF in specific is a very promising manufacturing method for the fabrication of Ti-64 components requiring high accuracy.
- LPBF is a process with a complex thermal behaviour leading to the evolution of inevitable defects in the components, namely porosity, surface roughness, residual stresses and anisotropy. These defects can however be eliminated by further post processing.
- Microstructure of Ti-64 manufactured by LPBF contains acicular α' martensitic phase, HCP α phase and prior beta grain boundaries.
- Post process heat treatments are crucial to obtain optimal mechanical properties. Stress relief eliminates residual stresses, annealing leads to decomposition of martensite and evolution of favorable microstructures while HIP achieves both elimination of porosity and decomposition of martensite.
- LPBF as fabricated Ti-64 shows very high strengths and low ductility due to the presence of the martensitic phase. Annealing heat treatments significantly improves the ductility due to the evolution of a two phase microstructure leading to slip transfer between the two phases.
- Near threshold fatigue of LPBF Ti-64 is studied very less when compared to fatigue life testing.
- Porosity, surface roughness, load ratio and microstructure affects the near threshold values. Crack closure effects play an important role in low load ratios. Coarser microstructure increases fatigue threshold value while prior beta grain boundaries increases crack branching.
- Most of the literature involving near threshold fatigue performed tests at a load ratio of 0.1 and most of them did not acknowledge the effect of crack closure. Very little literature is available for load ratios over 0.6.

2.7.1. Research gaps

Based on the conclusions of the literature review, the following research gaps were identified.

- The volume of research regarding near threshold fatigue of LPBF Ti-64 is very less when compared to fatigue life testing.
- Very few studies reached a fatigue crack growth rate of 10^{-7} mm/cycle to characterize the fatigue threshold of the material.
- In all of the literature regarding near threshold fatigue of Ti-64, only ”standard” sized samples were used and the scope of smaller sized samples to reduce material wastage has not been explored.

2.8. Research Objectives

Based on the research gaps observed in the literature, the following research objective has been put forth.

- Can sub-sized specimens be used for accurately determining the fatigue threshold of Ti-6Al-4V manufactured by Laser powder bed fusion?

To realize the research objective, the following research questions were framed.

- What are the differences in microstructures of conventionally manufactured and LPBF components subjected to different heat treatments.
- What is the influence of microstructure on near threshold fatigue properties.
- What is the influence of sample size on the fatigue threshold value.

3

Materials and Methods

3.1. Materials

A number of different types of samples were used in this research to answer the research questions. A general classification and categorization of these samples are provided in this section and the subsequent sub-sections.

3.1.1. Manufacturing and heat treatment

The Ti-6Al-4V samples used in this study can be divided into two categories based on the manufacturing method, the first are the samples manufactured by conventional manufacturing processes (referred to as conventional) and the second are the samples manufactured by Laser powder bed fusion (referred to as LPBF).

The conventional material was obtained in the form of cylinders in the hot forged and mill annealed condition. Mill annealing is a common heat treatment process involving heating to a temperature of 705°C, a hold time of 3 hours followed by air cooling to room temperature. The geometry and dimensions of the final samples are mentioned in the subsequent sub-section.

The processing parameters of the LPBF process is shown in Table 3.1. The entire LPBF process was conducted in an atmosphere of Argon to prevent the oxidation of the material.

Table 3.1: Laser powder bed fusion process parameters

Laser power (W)	Scan speed (mm/s)	Layer thickness (μm)	Laser spot diameter (μm)	Hatch distance (μm)	Volume energy density (J/mm^2)
170	1200	30	80	100	47

As mentioned in chapter 2, the component in the as-fabricated condition after the LPBF process contains a martensitic microstructure and is hence very brittle in nature.

Heat treatment is therefore performed to achieve a more favourable microstructure. Two types of heat treatments are investigated in this study, annealing and stress relief heat treatment. In annealing, a peak temperature of 920°C is maintained for 3 hours followed by furnace cooling and in the stress relief treatment, a temperature of 610°C is maintained for a duration of 1 hour followed by air cooling. An illustration of the heat treatments for the LPBF and the conventional samples is shown in Figure 3.1

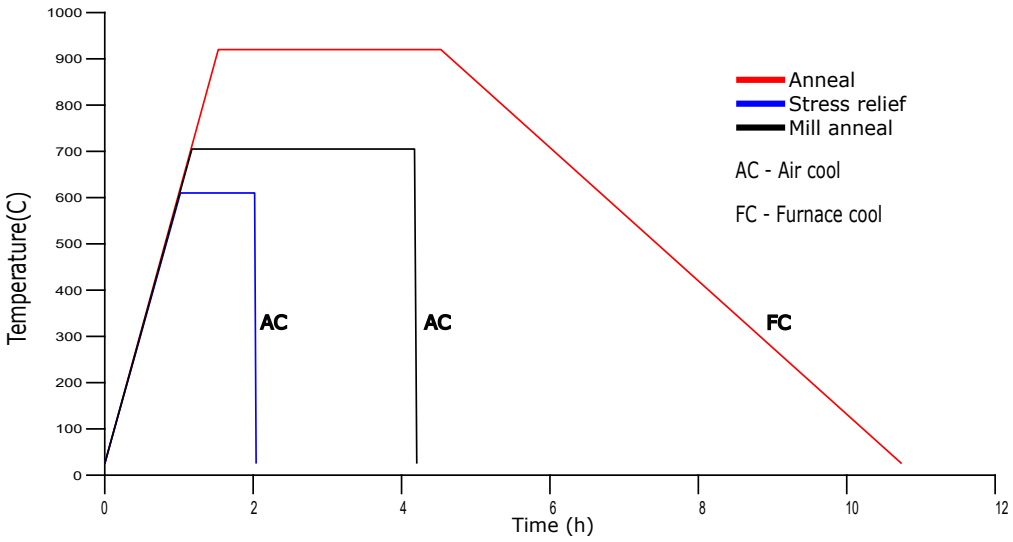


Figure 3.1: Different heat treatments on the conventional and LPBF samples.

In general, the heating rate during the heat treatment is taken as 10°C/min. For air cooling, the cooling rate is usually 7°C/sec while for furnace cooling, the cooling rate is 0.04°C/sec [42]. To avoid the diffusion of oxygen and nitrogen atoms into the sample at elevated temperatures, the heat treatments were also performed in an atmosphere of Argon.

3.1.2. Geometry and dimensions

All the test specimens used in this study had the same Single Edge Notch Bending (SENB) specimen geometry as prescribed by ASTM E-399 for fatigue testing [81]. Two broad classifications are made based on the dimensions of the specimens used in this study. Samples having the dimensions 70x10x5 mm are referred to as the ”large” samples in this report from here on while the specimens having the same geometry but with the dimensions 35x5x2.5 mm are referred to as the ”small” samples in this study from here on. The projected views of the large and small sample is shown in Figure 3.2 and Figure 3.3

Parts produced by LPBF were done in two orientations, vertical and horizontal orientation. A schematic showing the differences in the two is shown in Figure 3.4. The samples were received as rectangular blocks and the notch was then machined using Electrical Discharge Machining. For the vertical orientation, the notch was machined such that the crack propagated along the ’X’ axis and the crack plane was parallel

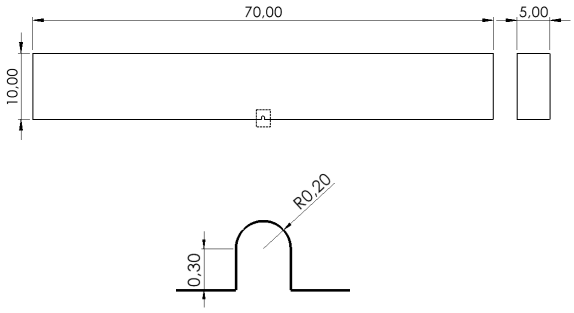


Figure 3.2: Projected views of the large SENB sample

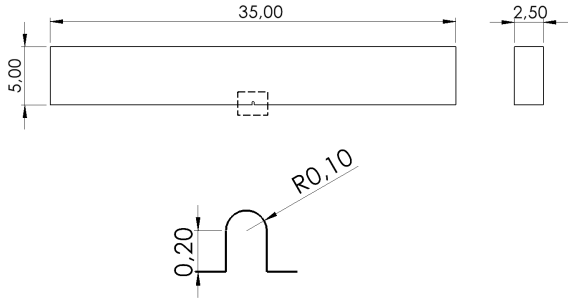


Figure 3.3: projected views of the small SENB sample

to the XY plane in the figure. For the horizontal orientation, the notch was machined such that the direction of crack propagation was along the 'Y' axis and the crack plane was parallel to the YZ plane in the figure.

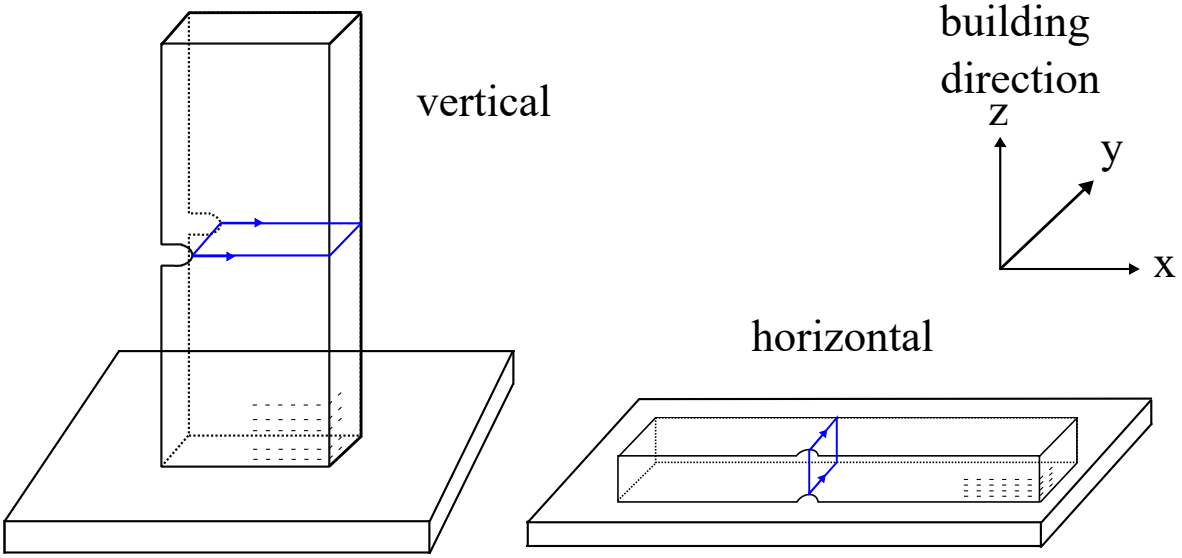


Figure 3.4: Schematic showing the different orientations and the crack planes.

3.2. Microstructure Characterization

All types of samples were characterized using optical microscopy, Scanning elec-

tron microscopy, X-Ray diffraction and hardness tests.

3.2.1. Microscopy

To observe the microstructure of the material, a segment of the SENB specimen is cut from two different planes and hot mounted on a conductive resin to ensure easier handling of the sample. The samples are first plane ground using the coarse grit P80 and P180 SiC sanding papers to ensure a flat surface and then ground using finer grit sanding papers all the way to the P2000 paper to eliminate large scratches on the surface of the sample using the Struers Labopol-25 machines. A summary of the sanding steps is shown in Table 3.2.

Table 3.2: Steps for sanding of Ti-6Al-4V

Sanding paper	Grit size (μm)	Rotation speed (rpm)	Time (s)
P80	196	250	20
P180	75	250	20
P320	46	250	20
P800	21.8	250	30
P1200	15.2	250	60
P2000	10	250	120

The next step after sanding the sample is to remove the fine scratches on the sample. This is achieved by polishing. As the usual $3\mu m$ and $1\mu m$ diamond slurry induces deformations on the surface that are really difficult to remove. To avoid the deformations, water based diamond suspensions from Struers, DP suspensions are used. Suspension sizes of $9\mu m$, $6\mu m$ and $3\mu m$ are used on an MD-Mol cloth to achieve a mirror-like finish to eliminate most scratches. The final step is to perform active oxide polishing using an OP-S solution having colloidal silica particles of size 0.25 μm on an MD-Chem cloth. While polishing with OP-S, the sample is cleaned using 2-isopropanol solution in regular intervals to prevent premature etching. The sample is completely scratch free after the polishing process. The final step before examining the sample under the microscope is etch the sample to selectively corrode the sample to show the different features in the microstructure. Kroll's reagent containing 87.9 ml H_2O, 9.4 ml HNO_3 and 2.7 ml HF is used as an etchant. The sample is carefully dipped into the etchant until the microstructural features are visible under the optical microscope. The sample is then flushed using 2-isopropanol and cleaned using an ultrasonic bath to prevent further etching.

Optical microscopes Leica DMLM and Olympus optical microscopes and Keyence digital microscopes are used for microstructure analysis. Microstructural features such as grains, grain boundaries and different phases were observed under the microscope. Grain sizes in the microstructure are determined using the intercept method based on ASTM E-112 [83]. For a microstructure with equiaxed grains, a straight line is drawn across the microstructure and the number of intercepts of the line with the

grain boundaries is determined and an average value of the grain size is calculated. The scanning electron microscope Jeol JSM IT-100 was used to observe the fracture surfaces and for Energy Dispersive X-Ray Spectroscopy (EDS). To calculate the roughness of the fracture surfaces, SEM images of the fracture surfaces were taken and imageJ software was used to calculate the surface roughness. For each surface, 5 measurements were taken and the average value was calculated.

3.2.2. Hardness

Hardness tests were performed on a Struers Durascan hardness tester. Hardness tests were performed as there is an empirical relationship between hardness and yield strength. As yield strength is dependant on microstructural features like grain sizes and different phases, the measured hardness also proves to be an indicator of the size of the microstructural features. The yield strength calculated from the hardness was used to determine the minimum uncracked ligament size and the plastic zone size which is explained in the subsequent section. 20 measurements with sufficient distance between each were taken for each sample with a load of 0.3 Kgf with a dwell time of 15 seconds, hence giving HV 0.3 hardness values. All measurements were taken in the XZ plane of the sample, at a sufficient distance from the surface as shown in Figure 3.5.

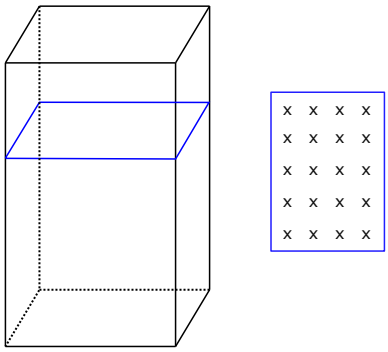


Figure 3.5: Plane of measurement for the hardness tests.

3.2.3. X-Ray Diffraction

X-Ray Diffraction (XRD) was performed with the objective of identifying and confirming the presence of phases in the microstructure and estimating the phase fractions of the different phases. The samples were in the polished condition before XRD analysis. A Bruker D8 Advance diffractometer Bragg- Brentano geometry and Lynxeye detector was used for the analysis. A Cu Kα radiation of 45 kV and 40 mA was used to conduct the analysis. A Rietveld fitting was utilized to estimate the phase fractions of the phases.

3.3. Fatigue testing

Large sample test setup

Figure 3.6a shows an zoomed out view and Figure 3.6b shows a zoomed in view of the fatigue test setup used in this study for the large samples. The components numbered in the figures are as follows, (1),(4) test platform, (2) current supply from the current generator, (3) voltage probe across the crack, (4) 3 point bending roller, (5) cameras, (6) Glass fibre insulation, (7) rollers, (8) Poly methyl meta acrylate (PMMA) support, (9) test sample.

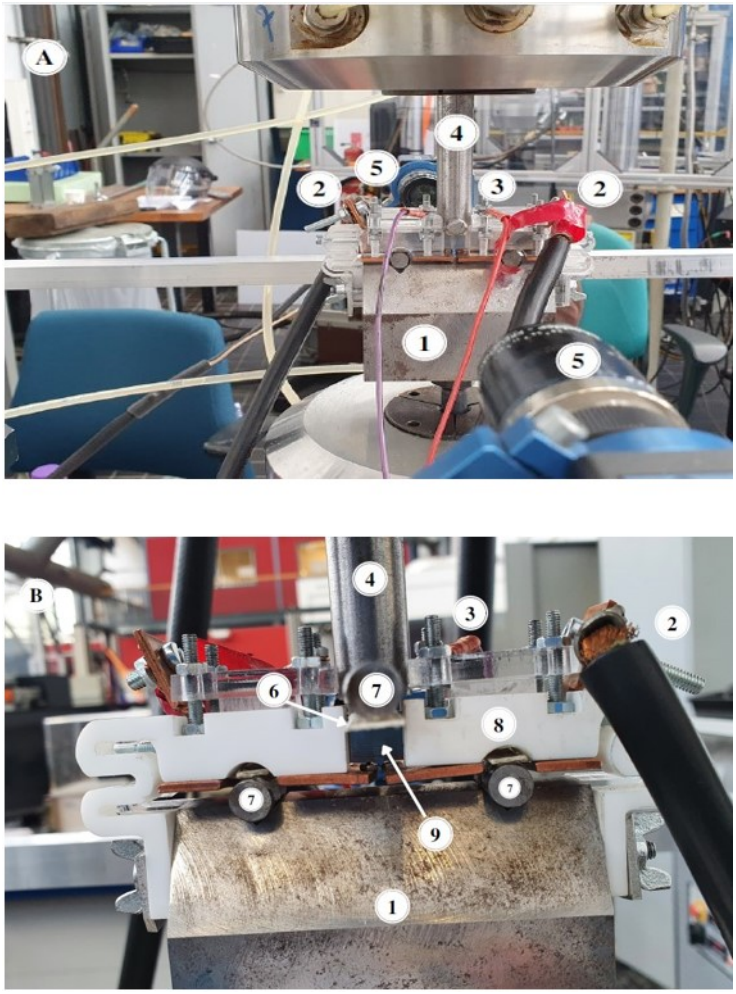


Figure 3.6: Large sample fatigue test setup a) zoomed out, b) zoomed in

An MTS 858 table top system using a hydraulic servo machine with a maximum load capacity of 25 kN was used for loading. The load resolution of the machine was 125 N. A platform and rollers made of stainless steel acted as the contact points for the 3 point bending tests. The distance between the rollers were designed according to the ASTM E399 standard [81]. Digital cameras by Limess were used to visually calibrate the crack length during the test on both sides of the sample. A Direct Current Potential Drop (DCPD) technique is used to accurately monitor the crack length. The DCPD system which is not shown in the figures also acts as a current generator. The PMMA support houses the test sample and the voltage probes. The PMMA support

also ensures easy alignment of the notch with the roller. Two sets of voltages are measured, the first one which is directly across the crack is called the 'X' voltage drop and the second voltage drop is called the reference potential to eliminate the thermo-electric effects or the 'Y'. Ideally, the reference potential would also be measured at the far ends of the test sample to be independent of the crack but due to the saturation limit of the DCPD setup, another Ti-6Al-4V sample was connected in parallel to the test sample and the reference potential was measured on the second sample. The second sample which is not shown in the figure, also acts as a shunt to reduce the potential drop on the test sample to prevent saturation of the voltage.

Small sample test setup

For the small samples, a few changes are made to the test setup to accommodate for the smaller dimensions of the sample. The setup is shown in Figure 3.7.

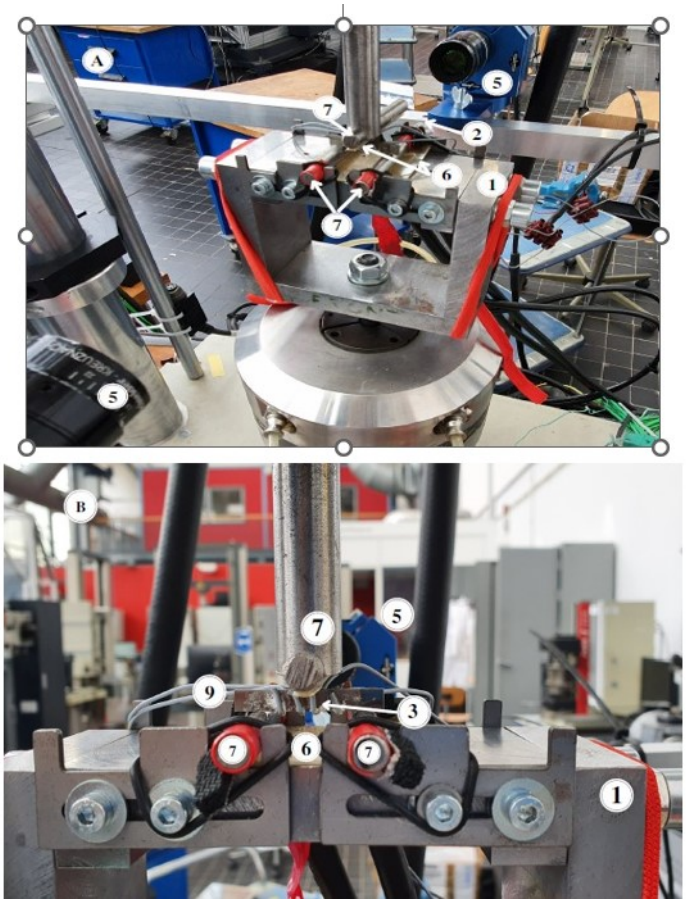


Figure 3.7: Small sample fatigue test setup a) zoomed out, b) zoomed in

As seen in the figures, a different platform is used to support the rollers and the sample. The distance between the rollers for this setup were also according to ASTM E399. Current is supplied to the sample through the rollers. Due to this, the effect of current fluctuation has to be eliminated. As a result, the reference 'Y' probes are placed on the test sample at a distance which makes it largely independent of the crack

length. The purpose of the shunt which is not shown in the figures is solely to split the current to prevent voltage saturation. A block of aluminium is used instead as a shunt instead of Ti-6Al-4V because of it's higher conductivity. In addition to the rollers being insulated with glass fibre, the platform is also insulated. The voltage probes were connected to the sample using a combination of conductive adhesives and super glue. Schematics of the large and small sample test setups is shown in Figure 3.8. Before testing, straight lines at regular intervals were scribed on the sample. For the large samples, the lines were at 0.5 mm intervals and for the small samples, the lines were at 0.3 mm intervals. The distance of the lines from the notch was accurately measured using an optical microscope.

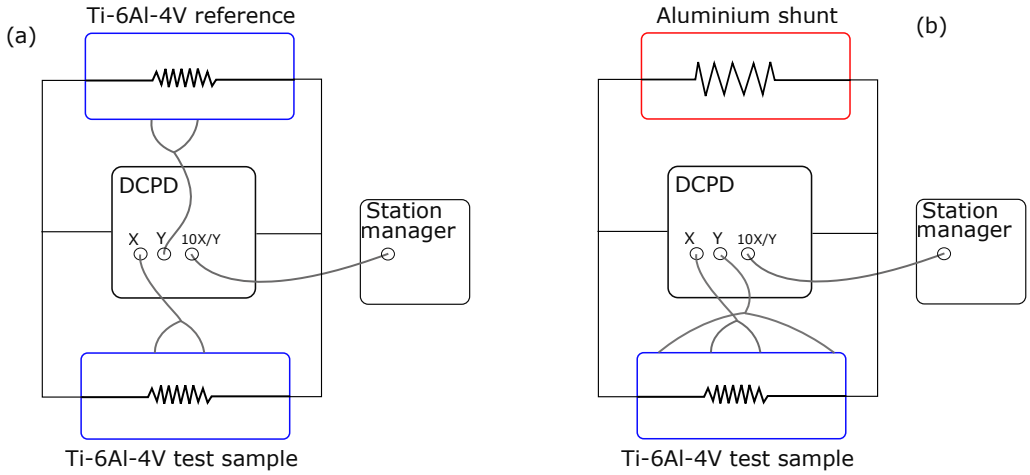


Figure 3.8: Schematic of a) large sample , b) small sample test setup.

Threshold test

The main objective of the fatigue test design is to determine the threshold stress intensity range of the material. The procedure to determine the same is given in this section. The test design for the large and small samples are similar with a few differences.

The stress intensity range value for 3 point bending specimens is calculated using the following equation

$$\Delta K = \frac{\Delta P S}{B W^{3/2}} . f(\frac{a}{W}) \tag{3.1}$$

where K is the stress intensity value, P is the load, S is the span length, B is the thickness and W is the width of the sample. f(a/W) is a function of the crack length and width which is calculated using Equation 3.2.

$$f(\frac{a}{W}) = 3\sqrt{\frac{a}{W}} . \frac{1.99 - (\frac{a}{W})(1 - \frac{a}{W})[2.15 - 3.93\frac{a}{W} + 2.7(\frac{a}{W})^2]}{2(1 + 2\frac{a}{W})(1 - \frac{a}{W})^{3/2}} \tag{3.2}$$

Before the actual threshold test, a fatigue precrack is to be grown. The purpose of a fatigue precrack is to ensure the growth of a straight crack and eliminating the effects of the machining of the notch. The precrack was grown to a size of at least 0.1B as per ASTM E647. The forces were also step down such that the smaller load would result in an increase in crack length that was larger than the plastic zone size resulting from the previous load. The monotonic plastic zone size was calculated according to the equation given below

$$R_P = (\frac{1}{3\pi})(\frac{K'_{max}}{\sigma_{YS}})^2 \tag{3.3}$$

where R_P is the plastic zone size, K'_{max} is the Kmax value from the latest load history and σ_{YS} is the yield strength of the material. Another event to take into consideration is the crack symmetry after pre-fatigue. It was ensured that the crack length on both sides of the test sample did not differ by more than 0.25B. During the pre-fatigue, the DCPD system was also calibrated. This was done using the scribe lines on the sample. The voltage at each line was observed and a linear relationship between the crack length and voltage was established. DCPD calibration had to be done before every test as the distance between the voltage probes across the crack for both the large and small samples was not a constant.

To determine the threshold intensity range, constant Kmax tests were performed. An illustration of the constant Kmax tests is shown in Figure 3.9.

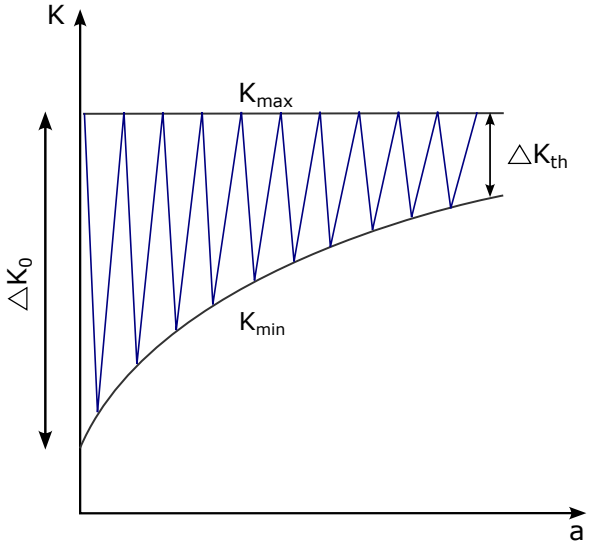


Figure 3.9: Illustration of the constant Kmax test.

As the name suggests, Kmax is maintained at a constant value for the entire test while the Kmin value is gradually increased. The Kmax value is determined according to Equation 2.4

$$K_{max} = \frac{\Delta K}{1 - R}$$

It was ensured that the selected Kmax value was higher than the Kmax value during the final pre-fatigue load cycle. The value of Kmin was increased gradually according to the equation Equation 2.5.

$$K_{min} = K_0 exp(C(a - a_0))$$

where K_0 is the initial Kmin value, a_0 is is the crack length after pre-fatigue, a is the instantaneous crack length and C is the stress intensity gradient. ASTM standards suggest a C value of 80 mm^{-1} but due to feasibility regarding the minimum uncracked ligament size, a stress intensity gradient value of 95 mm^{-1} was chosen for both the large and the small samples. The minimum uncracked ligament size for the sample was calculated using according to ASTM E647.

$$W - a \geq (\frac{4}{\pi})(\frac{K_{max}}{\sigma_{YS}})^2 \tag{3.4}$$

For the large samples, a Kmax of 14.5 MPa$\sqrt{m}$ was used while for the small samples, a Kmax of 14.5 as well as 17 MPa$\sqrt{m}$ was used. It was ensured that the minimum load applied was still greater than the load resolution of the machine which is 125 N. The Kmin value was incremented for every 0.1 mm increase in crack length. For the large samples, a frequency of 60 Hz was employed while for the small samples, a frequency of 70 Hz was used. After the constant Kmax tests, a da/dn vs ΔK FCGR curves are plotted and the fatigue threshold value is determined as the ΔK at which a crack growth rate of 10^{-10} m/cycle is achieved.

For confirmation of the reliability of the constant Kmax test, a constant ΔK was performed. A particular ΔK was selected with the same Kmax such that a steady crack growth rate was observed. This crack growth rate was then compared to the crack growth rate for the same ΔK in the da/dn vs ΔK plot obtained from the constant Kmax tests. The results of the constant Δk test is shown in Appendix C.

3.4. Summary of fatigue tests

A summary of the fatigue tests performed on the different samples is shown in Figure 3.10.

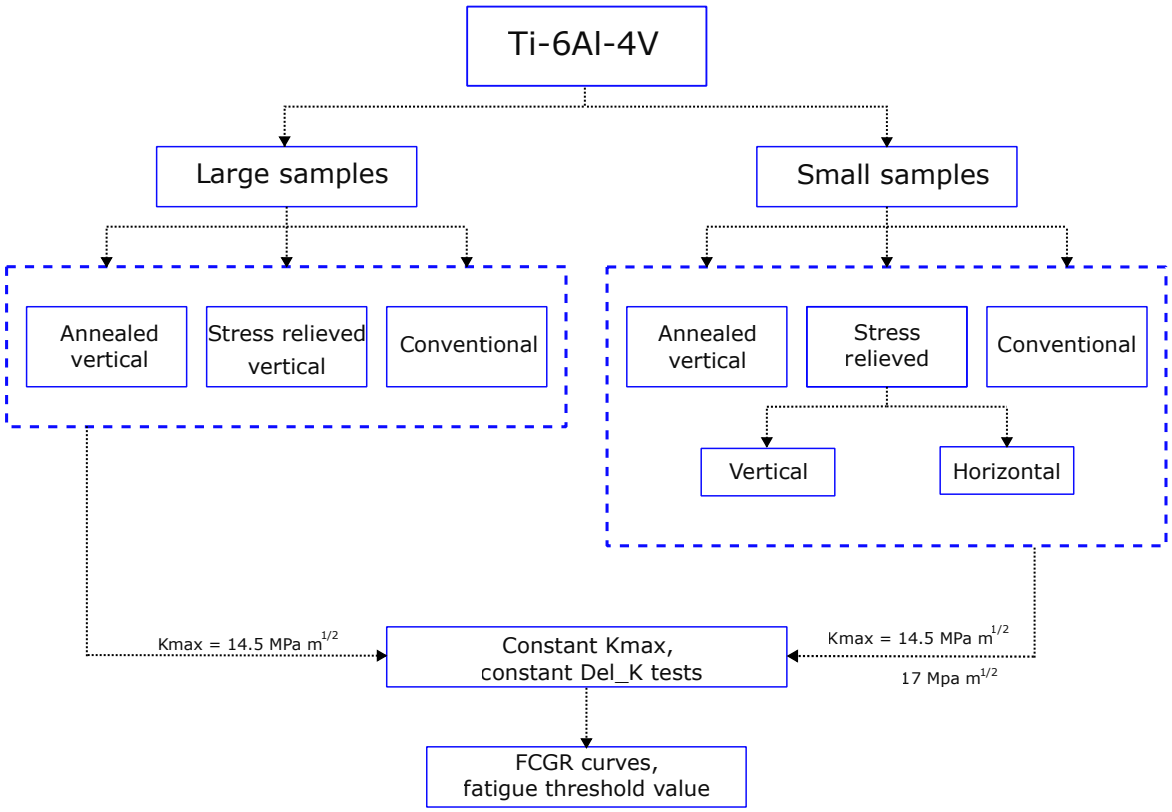


Figure 3.10: Summary of the fatigue tests

4

Results and discussion

4.1. Effect of heat treatment on microstructure

A series of increasingly zoomed in optical micrographs of the three different microstructures/conditions used in the study are shown in Figure 4.1, Figure 4.2 and Figure 4.3.

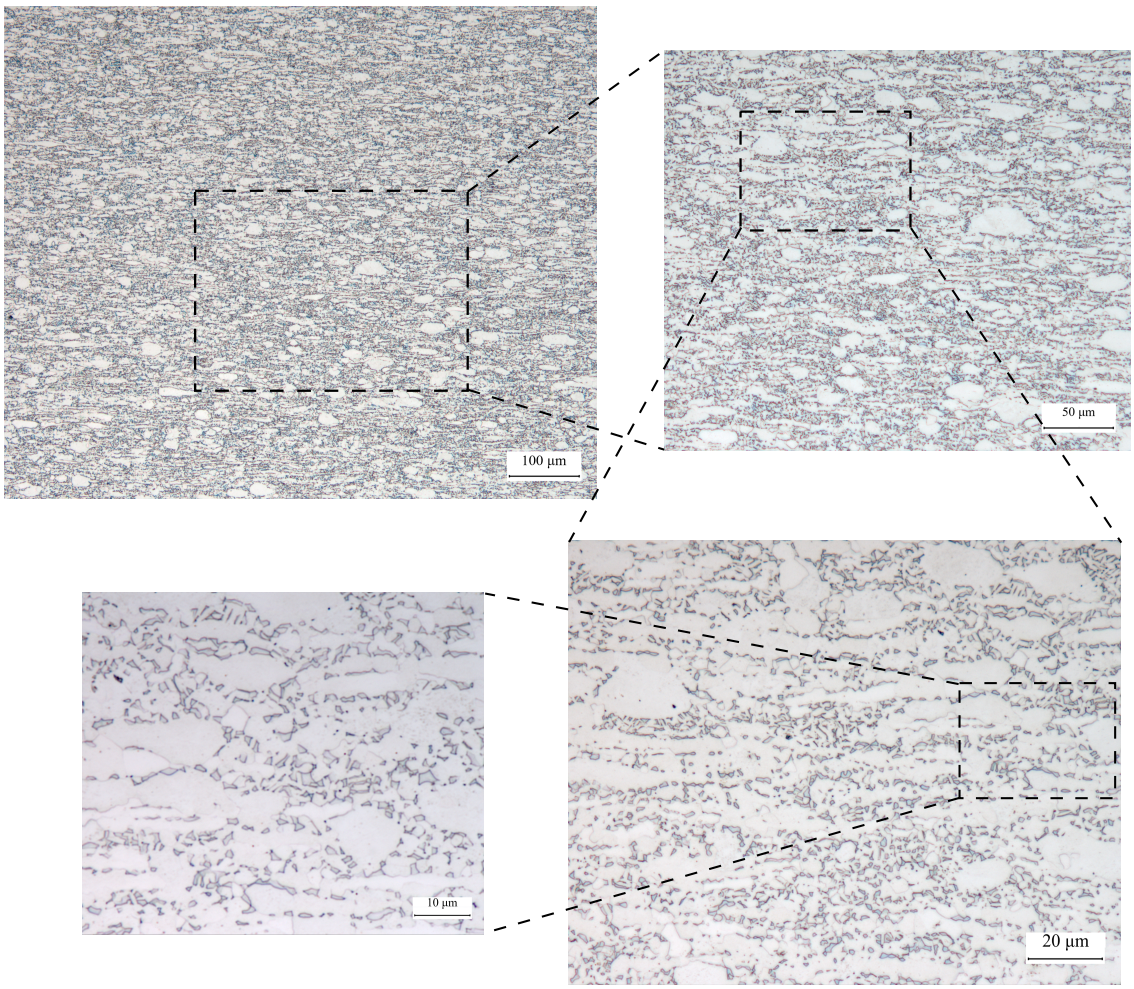


Figure 4.1: Optical micrographs of the conventional microstructure.

In all optical micrographs, the alpha phase is shown in white while the beta phase which is formed in the grain boundaries is shown in black. All micrographs were taken on the XZ plane of the sample. Figure 4.1 shows the microstructure of the conventional material in the as received condition. It can be seen that the grains are equiaxed with a grain size of around 15 μm with a preferred orientation. This preferred orientation of the grains could be a result of the rolling direction. The small grain size of 15 μm is a result of the mechanical processing of the material resulting in the fragmentation of the larger grains. The presence beta phase is also seen in black at the grain boundaries of the equiaxed alpha phase.

Figure 4.2 shows the optical micrograph of the stress relieved microstructure. As the lower magnifications did not reveal the features clearly, only a high magnification optical micrograph of the stress relieved sample was taken.

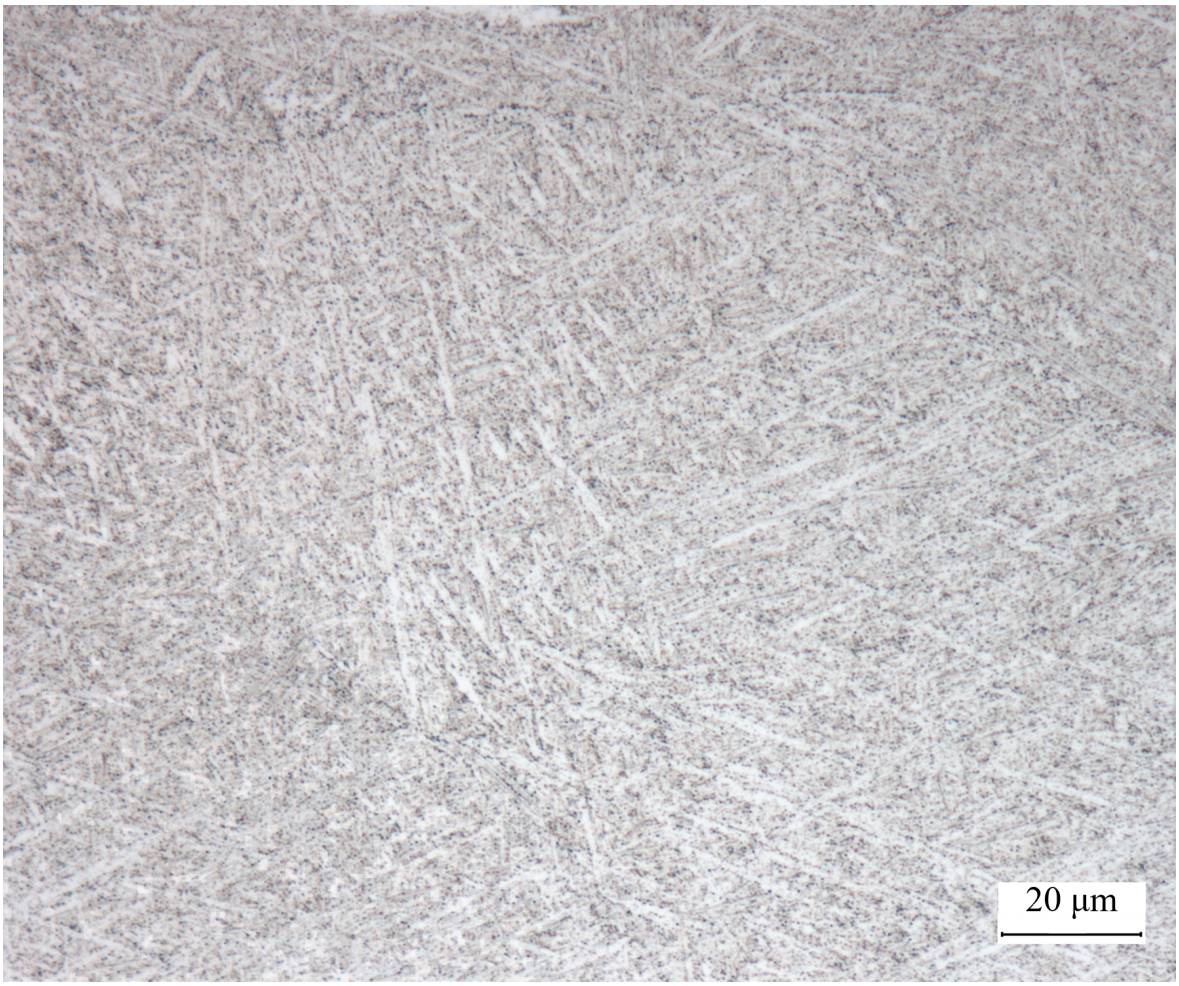


Figure 4.2: Optical micrograph of the stress relieved microstructure.

It can be clearly seen that a microstructure consisting of acicular martensite and lamellar alpha phase is obtained. As explained in chapter 2, acicular martensite is a result of the high temperatures and cooling rates used in the LPBF process. The stress relief heat treatment results in a partial decomposition of the martensitic needles to lamellar alpha phase. Nucleation of beta phase at the grain boundaries of the α' and

α laths as black spots is observed. Elongated prior beta grains were also observed on the XZ plane as a result of the complex thermal behavior of the LPBF process. The elongated PBGs has a length of a few hundred micrometers and a width close to 80 μm which corresponds to the dimensions observed in the literature. The length and width of the PBGs is dependant on the thermal gradient and hatch spacing employed in the fabrication of the sample.

Optical micrographs of the microstructure obtained after the annealing heat treatment is shown in Figure 4.3.

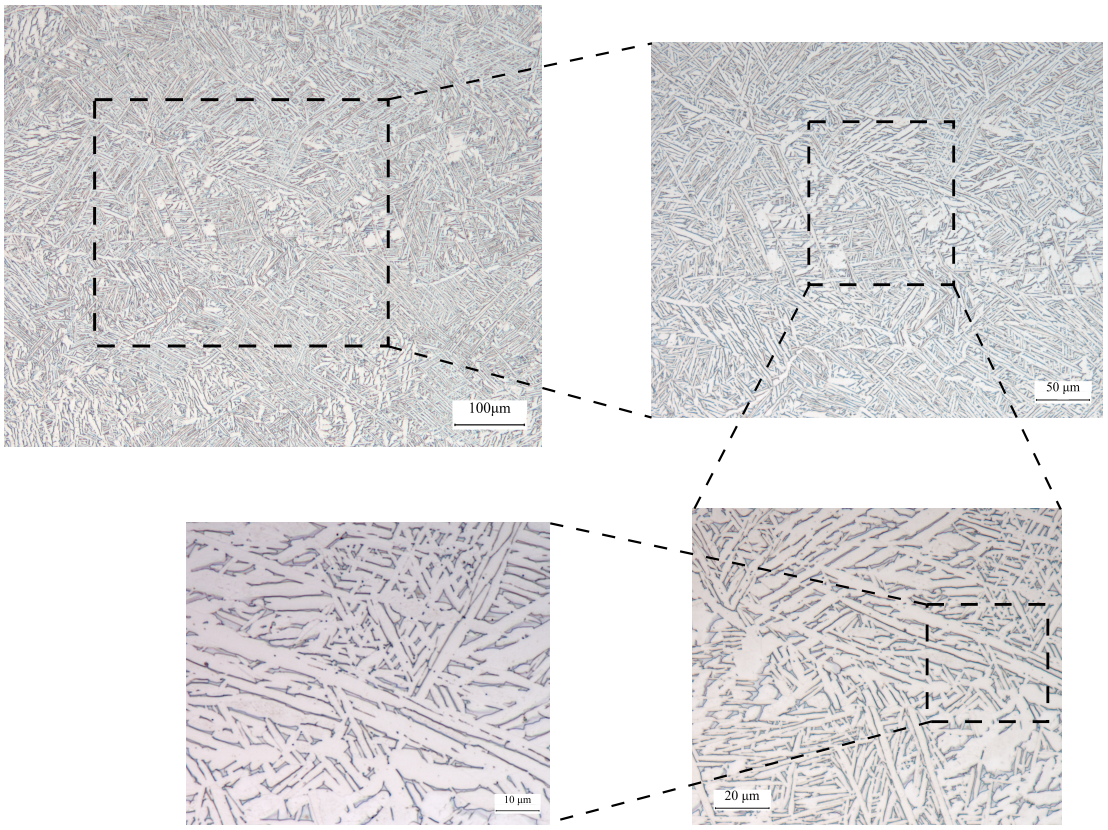


Figure 4.3: Optical micrographs of the annealed microstructure.

The heat treatment of heating the sample to 920 °C for 2 hours followed by air cooling to 400 °C and then furnace cooling to room temperature leads to the development of a lamellar microstructure with small quantities of globular alpha phase. Heating of the sample to 920 °C results in the complete decomposition of the martensite phase and increased nucleation of beta phase at the grain boundaries. The holding time of 2 hours leads to the growth of the alpha laths with a width of 2-5 μm. Unhindered growth of the alpha laths is not possible due to the presence of beta phase which also tries to grow in size. PGBs are also present in this microstructure with similar dimensions as that in the stress relieved microstructure. The alpha lamellae nucleate at the PBG boundaries and grow inwards.

Figure 4.4 shows SEM micrographs of the large samples.

In the SEM micrographs, the dark regions are the alpha phase while the white

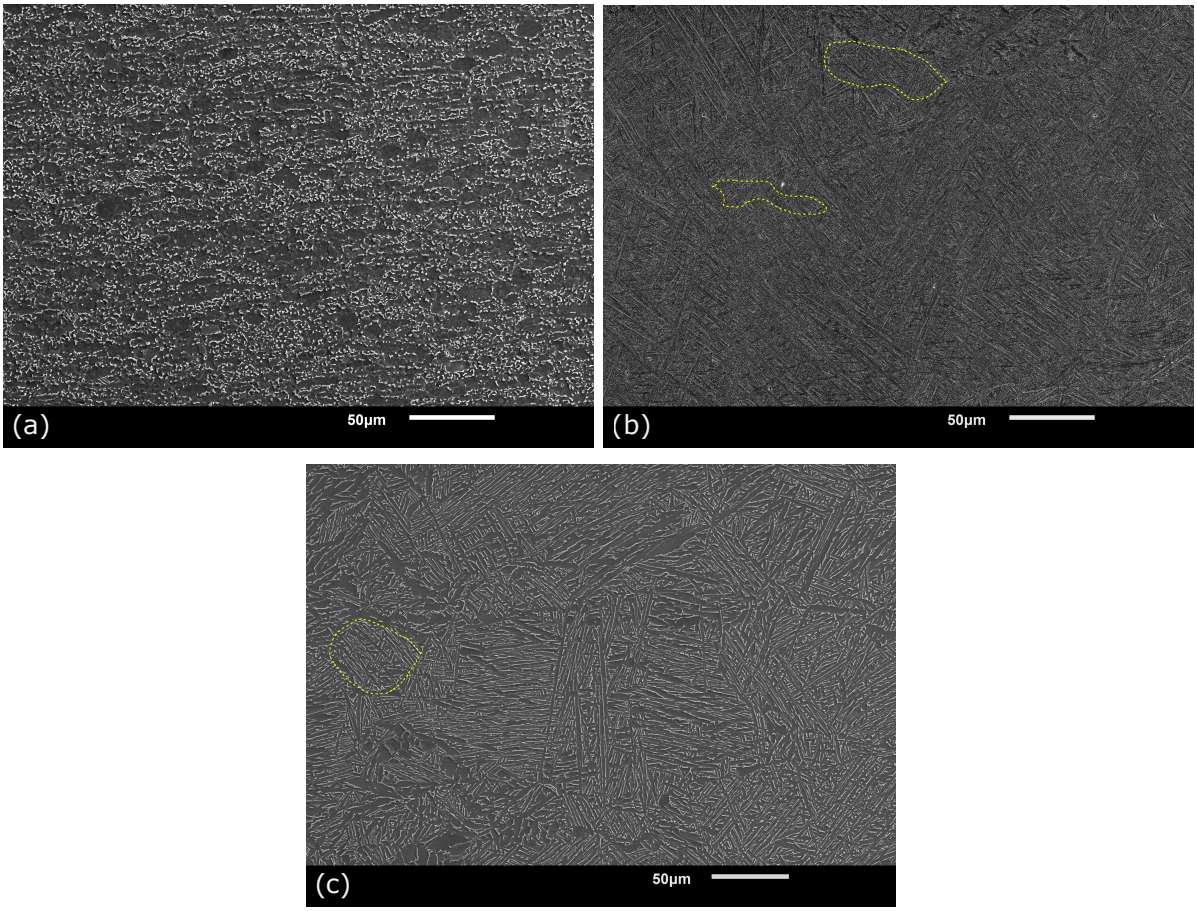


Figure 4.4: SEM micrographs of large a) conventional, b) Stress relieved and c) annealed microstructures. Dashed lines in (b) and (c) show PBG and alpha colony respectively.)

regions are beta phase. Figure 4.4a shows the conventional microstructure with equiaxed grains orientated towards the rolling direction. Figure 4.4b shows the SEM micrograph of the stress relieved microstructure. The prior beta grain is highlighted in yellow in the figure. Figure 4.4c shows the SEM micrograph of the annealed sample showing the lamellar microstructure. The alpha colony is highlighted in yellow in this figure. The SEM micrographs of the small samples is shown in Figure 4.5.

It can be seen that there is no change in microstructure between the large and small LPBF samples. For the conventional sample, an equiaxed microstructure is still observed but it could be said that the grain size could be smaller than the large sample. This could be due to a different heat treatment employed for the small samples.

4.2. XRD analysis

The main purpose of performing XRD analyses is to confirm the presence of different phases and to quantify the amount of the different phases. All XRD tests were done on the ZX plane of the vertical sample. The results from the XRD test for the conventional, stress relieved and annealed samples is shown in Figure 4.6.

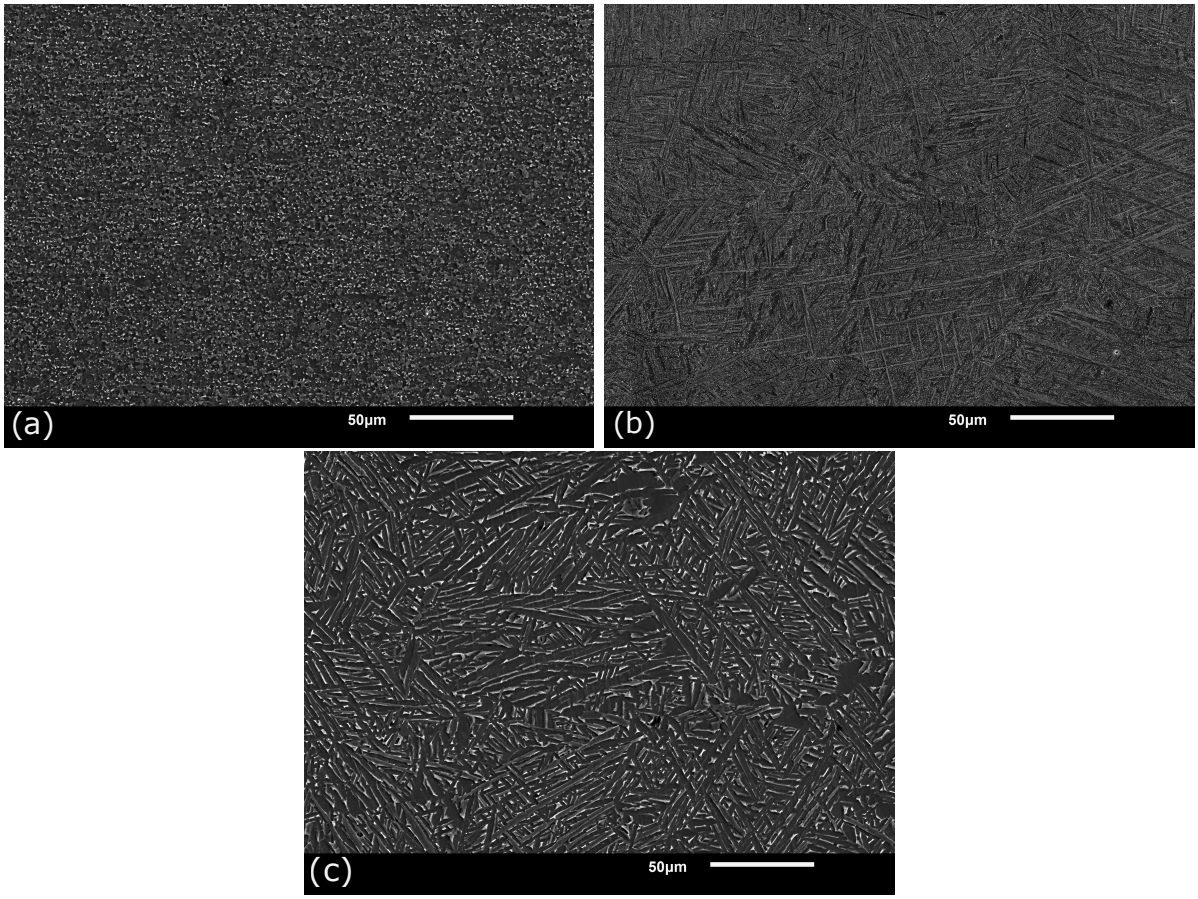


Figure 4.5: SEM micrographs of small a) conventional, b) Stress relieved and c) annealed microstructures.

The base line for the conventional sample is different from the other two as a different method for sample preparation was used. The conventional sample was embedded in a resin for easier polishing while the stress relieved and annealed samples were not embedded. It is clearly seen that all three samples are dominated by the alpha (hcp) phase. Around a 2θ angle of 39°, small peaks are seen on the conventional and annealed samples corresponding to the beta phase. This has also been seen by Facchini et al [45]. To quantify the phase fractions, a Rietveld fitting was performed and the resultant phase fractions in the different samples is shown in Table 4.1.

Table 4.1: Phase fractions in the different samples determined by XRD.

Sample	Alpha	Beta
Conventional	93.4 %	6.6 %
Stress relieved	96.5 %	3.5 %
Annealed	92.9 %	7.1 %

It can be seen that the stress relieved sample contains the least amounts of beta phase with 3.5% followed by conventional and annealed samples with 6.6% and 7.1%. These varying fractions of the different phases play an important role in the mechanical properties which is explained in the following sections.

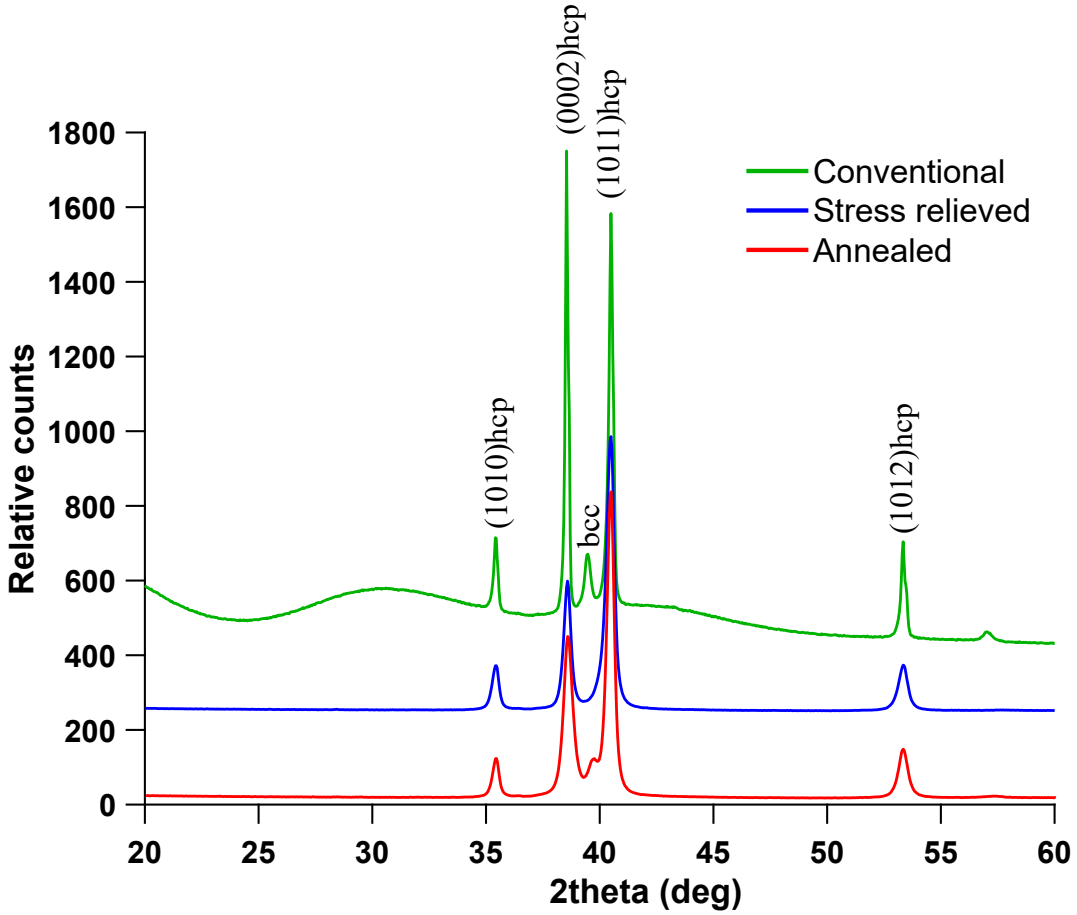


Figure 4.6: XRD results of a) Conventional, b) Stress relieved and c) Annealed samples.

4.3. Hardness

Micro-hardness tests were performed on the XY plane of the vertical samples at a distance from the surface. The results from the hardness tests is shown in Figure 4.7.

It can be seen that for the large samples, the conventional sample has the lowest hardness of 332 HV, annealed sample with a hardness of 345 HV and stress relieved with the highest hardness of 394 HV. This variation in hardness is directly correlated to grain sizes and the phase fractions in the microstructure. As explained in chapter 2, the beta phase is the softer phase while the alpha phase contributes to the higher strength of a material. The hardness is correlated to grain size with the well known Hall-Petch equation which says

$$\sigma_y = \sigma_0 + kd^{-1/2} \tag{4.1}$$

where d is the grain size in the microstructure. As the grain size decreases, the yield strength or the hardness increases due to grain boundary strengthening. The stress relieved sample shows the highest hardness due to the presence of thin acicular martensitic needles and also high dislocation densities in the grain boundaries. Al-

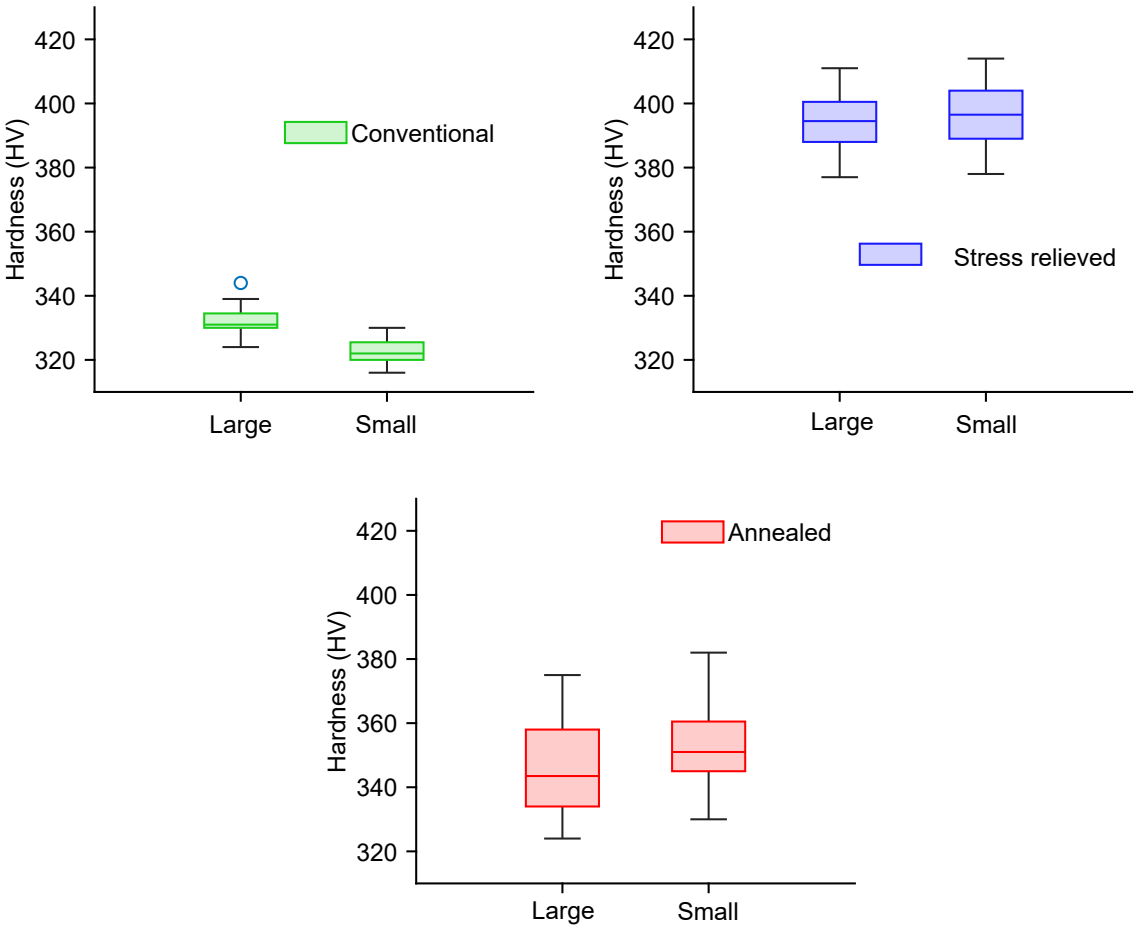


Figure 4.7: Hardness of the different samples

though the annealed sample has lesser amounts of beta phase than the conventional sample, it has a higher hardness due to the presence of a lamellar microstructure with a lath thickness close to 5 μm while the equiaxed conventional sample has a grain size close to 15 μm.

When the sample size is reduced, it can be seen that while the stress relieved and annealed samples does not show any significant change in hardness, the conventional sample drops in hardness from 332 to 322 HV. This decrease in hardness could be a result of a different heat treatment subjected to the small samples.

4.4. Fatigue behaviour

4.4.1. Effect of heat treatment

The fatigue crack growth rates for the large samples is shown in Figure 4.8. The fatigue threshold value is the stress intensity range when the fatigue crack growth rate reaches a value of 10^{-8} mm/cycle. The annealed microstructure shows the highest threshold value of 2.6 MPa$\sqrt{m}$, the conventional shows a value of 2.1 MPa$\sqrt{m}$ and the stress relieved microstructure has a fatigue threshold value of 1.8 MPa$\sqrt{m}$.

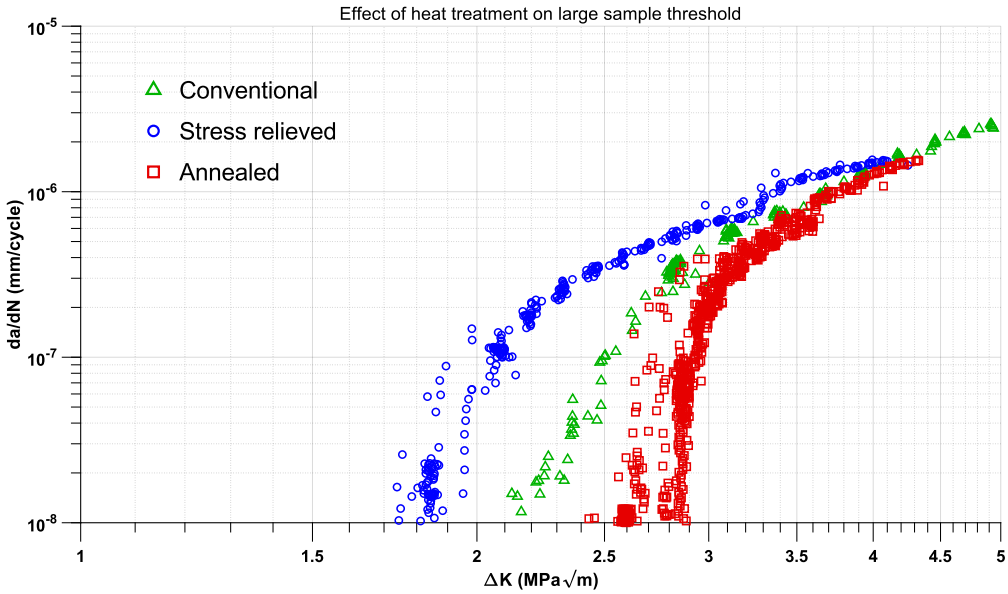


Figure 4.8: Effect of heat treatment on large sample fatigue threshold

The fatigue crack growth rates for the small samples is shown in Figure 4.9. In the case of the small samples, the conventional and annealed microstructures show a decrease in fatigue threshold values to 1.6 MPa$\sqrt{m}$ and 2.1 MPa$\sqrt{m}$. The stress relieved sample on the other hand shows the same threshold of 1.8 MPa$\sqrt{m}$. The small samples have a larger number of data points as additional tests with a Kmax of 17 MPa$\sqrt{m}$ and a frequency of 70 Hz. It can be seen that the change in Kmax and frequency to slightly higher values did not affect the fatigue threshold values. The effect of the sample size on the fatigue threshold is explained in the upcoming sections.

Fatigue cracks initiate and propagate according to the favourable slip systems available. The most favourable slip system is dependant on two factors, the Schmid factor and the critically resolved shear stress. The Schmid factor provides information regarding the orientation of the grain to the loading axis while the critically resolved shear stress is the amount of shear stress required to initiate the slip. Bantounas et al studied the dominant slip systems in Ti-64 and found that fatigue cracks mostly initiate at the alpha phase [84]. The alpha phase which is a HCP structure has three slip systems, the basal, prismatic and pyramidal slip systems. The authors also found that

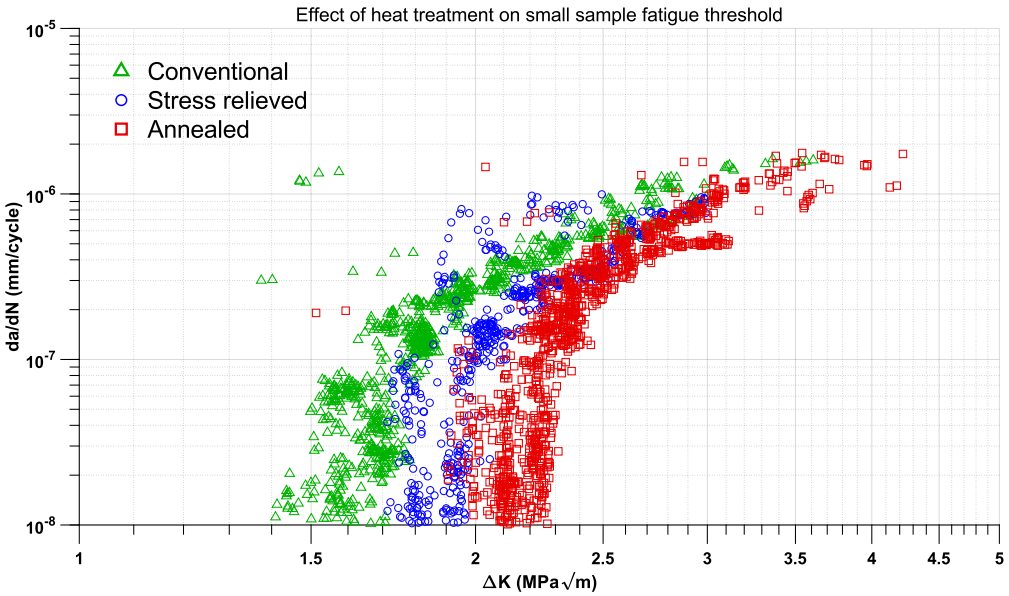


Figure 4.9: Effect of heat treatment on small sample fatigue threshold

slip initiated at the alpha phase with faceted feature which relates to basal slip [107]. Lunt et al however propose that the favourable slip system is dependant on other factors as well and the most favorable slip system is still unclear for dual phase Ti alloys [108]. As explained earlier, the LPBF process produces a unique microstructure with multiple distinct features like the prior beta grains and alpha colonies. These features themselves and the morphology of the microstructure, both play a role in the fatigue threshold values. As seen, for the large samples, the stress relieved microstructure showed the least threshold intensity range close to 1.8 MPa$\sqrt{m}$. This can be explained by the different microstructural features. The stress relieved microstructure contains acicular martensite which is a very brittle phase and some amounts of alpha and beta phase as well. As the martensitic phase is very brittle in nature, the plastic zone size formed in front of the crack tip is very small leading to easier plastic flow through the material and less energy dissipation at the crack tip. This leads to crack propagation without significant hindrance.

In the case of the annealed microstructure, the alpha laths are greater in thickness and there is also larger fractions of the beta phase than the stress relieved microstructure. The beta phase which is more ductile in nature results in a larger plastic zone size ahead of the crack tip which retards the propagation of the crack due to the increased amounts of energy that is dissipated at the crack tip. This explains the higher threshold value for the annealed microstructure.

The conventional large sample shows a fatigue threshold value of 2.2 MPa$\sqrt{m}$. This can be explained by differences in the microstructure when compared to the annealed sample. In the case of the conventional equiaxed microstructure, features such as PBG and alpha colonies, characteristic of LPBF samples are absent. This would mean that the possibility of deflection of the crack at those features is not available at those features leading to a lower degree of crack tortuosity and smaller threshold

value.

4.4.2. Effect of anisotropy

To briefly touch upon the effect of anisotropy of microstructure on the fatigue threshold values, a small stress relieved sample with a flat orientation was tested. Figure 4.9 shows the FCGR curve for the same test. It can be seen that a change in orientation from edge to flat resulted in a decrease of the fatigue threshold from 1.8 MPa$\sqrt{m}$ to around 1.5 MPa$\sqrt{m}$. This can be attributed to the orientation of the PBG boundary to the crack profile. A schematic of the crack profile orientation with the PBG boundaries in the edge and flat orientation is shown in Figure 4.15. It can be seen that in the edge orientation, the crack front perceives a long columnar PBG boundary while in the flat orientation, the crack front confronts only a smaller equiaxed PBG boundary. This would result in a larger crack deflection at the PBG boundary in the edge orientation than the flat orientation hence increasing the crack tortuosity and the fatigue threshold value.

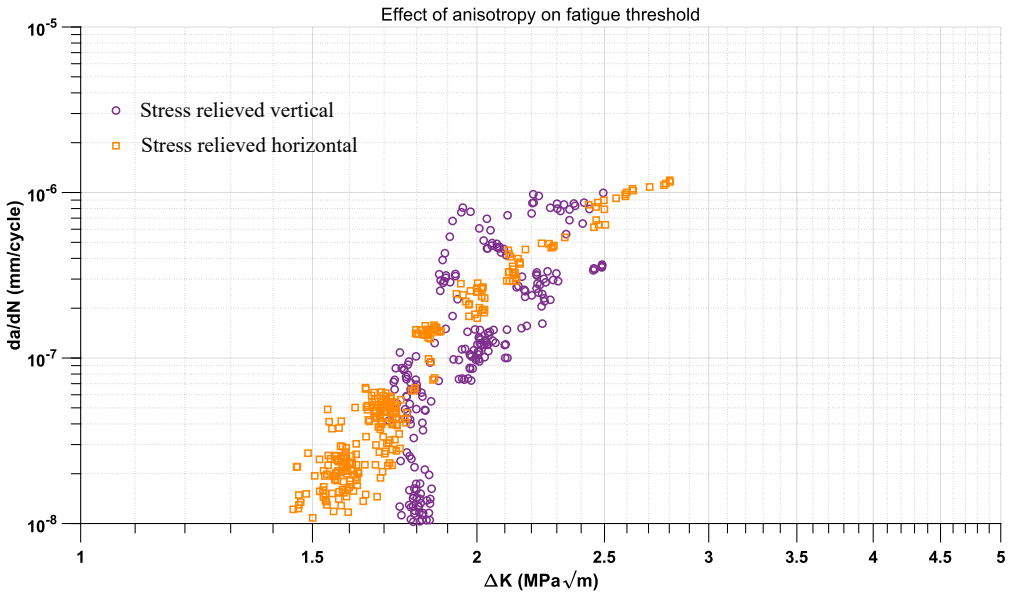


Figure 4.10: Fatigue crack growth rate curve of stress relieved microstructure in the vertical and horizontal orientations.

A summary of the constant Kmax fatigue threshold test results is shown in Table 4.2. From the table, it can be seen that even when the load ratio at threshold values is slightly different for the small samples for two different Kmax values, the threshold value does not change.

4.4.3. Influence of microstructure on crack propagation

The microstructure of the sample plays a crucial role in the fatigue properties of the materials. Analysis of the propagation of the crack through the microstructure provides important information regarding the influence of the microstructure.

Table 4.2: Summary of the threshold fatigue test results

Microstructure	Size	Orientation	K_{max} (MPa$\sqrt{m}$)	ΔK_{th} (MPa$\sqrt{m}$)	Final load ratio
Conventional	Large	-	14.5	2.2±0.1	0.86
	Small	-	14.5	1.6±0.2	0.89
			17		0.91
Stress relieved	Large	vertical	14.5	1.8±0.2	0.88
	Small	vertical	14.5	1.8±0.2	0.88
			17		0.89
		horizontal	14.5	1.5	0.90
Annealed	Large	vertical	14.5	2.6±0.2	0.82
	Small	vertical	14.5	2.1±0.2	0.86
			17		0.88

Images of the crack propagation through the different microstructures was taken for both the large and the small samples.The specimen was sectioned and a crack plane around the middle of the sample was analysed to ensure the analysis of crack propagation in the plane strain state.

In all crack profile images, figures a and b correspond to the large samples while figures c and d correspond to the small samples. In addition, figures a and c are the crack profiles in the steady growth rate regime while figures b and d show the crack profile in the threshold regime. In all the images, direction of crack propagation is upwards. This is shown as CD in the figures. The building direction is also shown in the figures as BD. For the conventional sample, the BD is taken as the direction of rolling/deformation.

The crack profile through the conventional microstructure is shown in Figure 4.11. It be seen that for both the large and the small samples, the crack propagation is trans-granular in nature. with the crack cutting through the grains instead of travelling along the grain boundaries. This can be attributed to an absence of grain boundary weakening features such as dislocations or precipitates. The threshold regime for both the large and the small samples show a larger degree of crack deflections and branching than the steady growth regime. One such bifurcation of the crack is enlarged and shown. This can be attributed to the absence of PBG boundaries along which the crack usually deflects in the steady growth regime.

The crack tortuosity in the threshold regime usually occurs at the grain boundaries when the crack changes it's slip system to the most favourable one.It can also be observed that the small sample displays a greater degree of crack tortuosity. This could be a result of the higher crack tip energy in the smaller sample. Cracks also display branching when the crack tip energy is very high and is dissipated by branch-

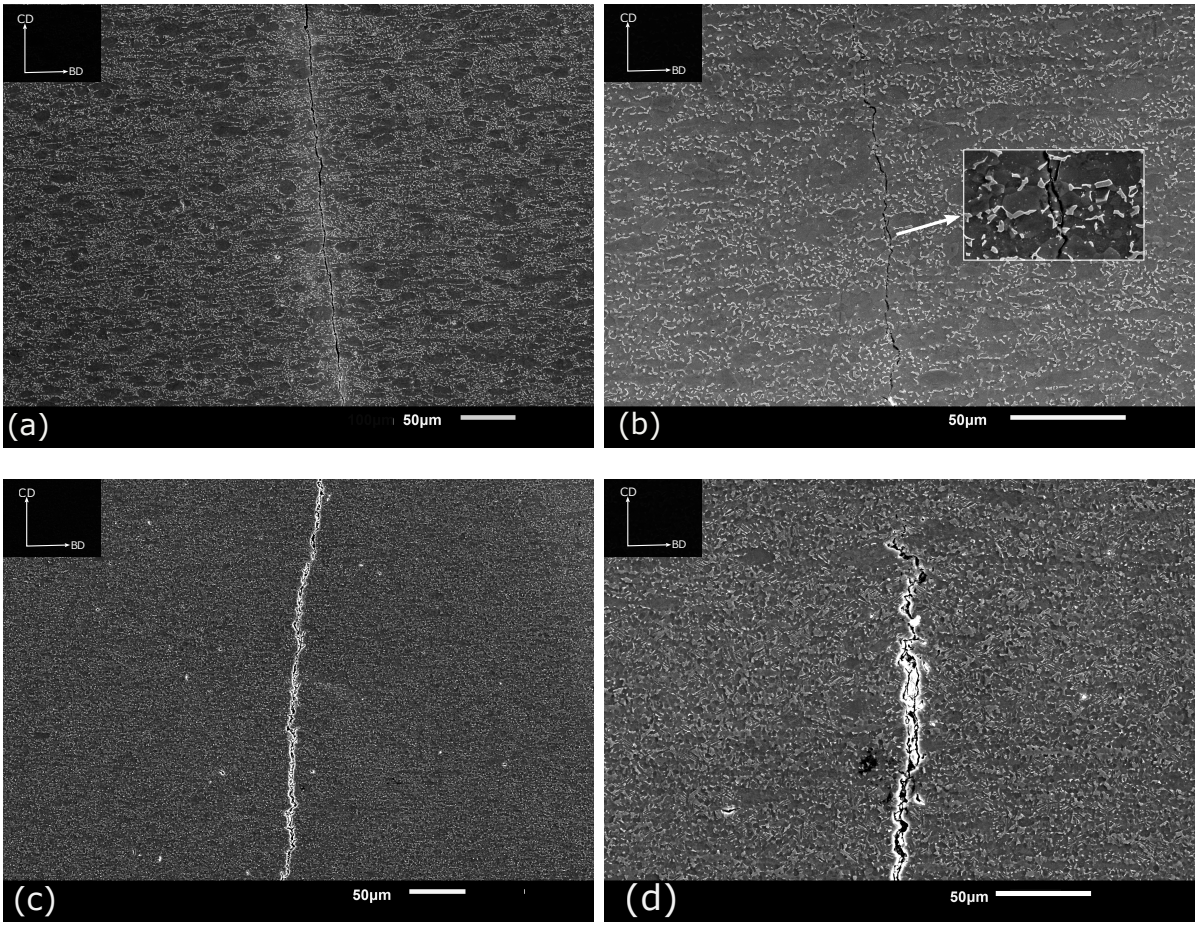


Figure 4.11: Crack profile through the conventional microstructure. (a),(b) large sample steady growth and threshold regime, (c),(d) small sample steady growth and threshold regime. Arrow directs to an enlarged bifurcation in (b).

ing to secondary crack planes. When the crack tip energy has been dissipated, the branched secondary crack stops growing and the primary crack on the primary crack plane which is the plane of loading, starts growing again. The crack tip energy in the smaller samples are higher due to higher constraint at the crack tip, the effect of which on the fcgr is explained in the upcoming sections.

The crack profile through the stress relieved microstructure is shown in Figure 4.12. In the threshold regime it can be seen that the cracks tend to propagate along the martensitic grain boundaries as they provide a more energetically favourable path. This is due to the increased dislocation density as a result of the high cooling rate of the LPBF process and the brittle nature of martensite weakening the grain boundaries. From the figure, it is observed that the crack propagation is a combination of both transgranular and intergranular mechanisms. The enlarged portions in Figure 4.12 shows intergranular crack propagation for both the large and the small samples which explains the low fatigue threshold value of 1.8 MPa$\sqrt{m}$.

The crack profile through the annealed microstructure is shown in Figure 4.13. It can be seen that in the steady growth regime, the crack has bee deflected along a

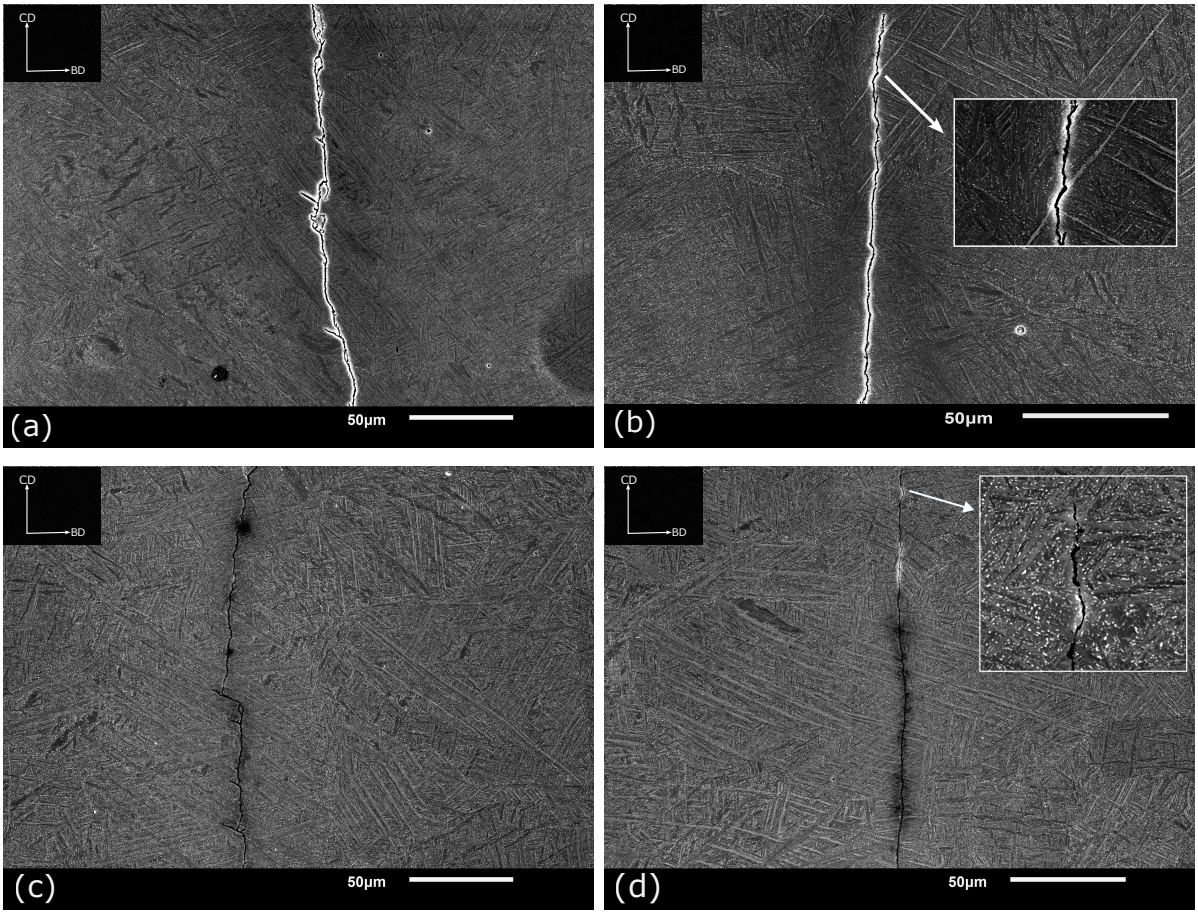


Figure 4.12: Crack profile through the stress relieved microstructure. (a),(b) large sample steady growth and threshold regime, (c),(d) small sample steady growth and threshold regime. Enlarged figures represent intergranular crack propagation in (b),(d).

PBG boundary as shown by a dotted yellow line in Figure 4.13a. Kumar et al proposed that the crack tortuosity is influenced by microstructural features in the same length scale as the monotonic plastic zone size which is a factor of the Kmax used in the test [74]. The plastic zone size was calculated according to Equation 3.3. Sadananda et al suggested that for the crack to be influenced by the microstructural features, the plastic zone size should be less than 1.5xl where l is the size of the microstructural features [85]. In this study the largest microstructural feature in the LPBF samples is the PBG which is of the order of a couple of hundred microns. The maximum monotonic plastic zone size ahead of the crack tip in the different microstructures which is a function of the yield strength of the material is shown in Table 4.3.

In the threshold regime, as the plastic zone size is much smaller compared to the steady growth regime, microstructural features such as laths and alpha colonies play a bigger role in the crack tortuosity. This is clearly seen in Figure 4.13b,d where there are a number of crack deflections and branching. The number degree of crack tortuosity is greater in the small samples just like in the conventional microstructure which is explained again by the amount of crack tip energy due to a higher constraint at the crack tip. The crack travels along a certain slip system in a lath and at a grain

Table 4.3: Monotonic plastic zone size ahead of the crack tip for the different microstructures.

Sample	Plastic zone size, R_p (μm)
Conventional	30.8
Stress relieved	22.3
Annealed	27.5

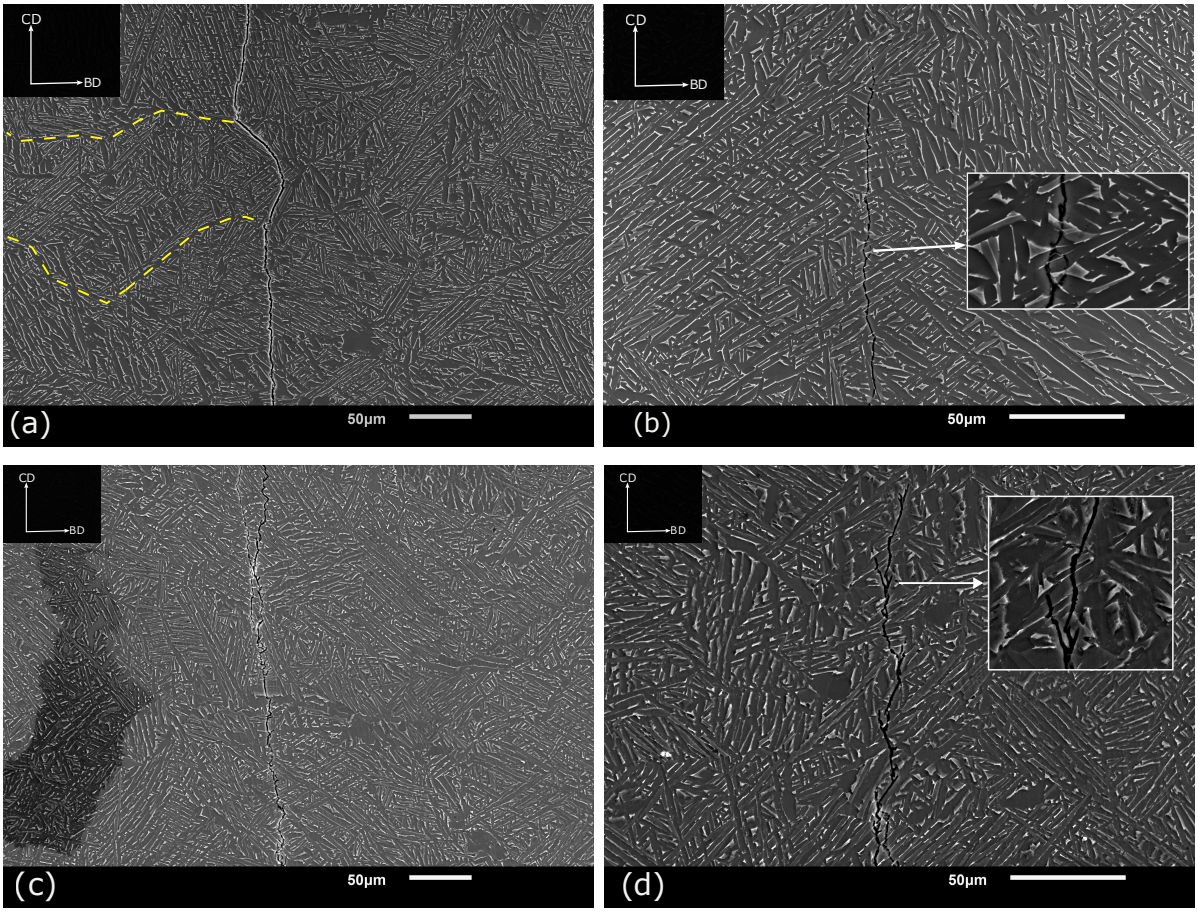


Figure 4.13: Crack profile through the annealed microstructure. (a),(b) large sample steady growth and threshold regime, (c),(d) small sample steady growth and threshold regime. Yellow line shows a PBG boundary in (a). Enlarged figures show crack tortuosity in (b),(d).

boundary, it comes into contact with the beta phase and a new slip system is traversed. The crack propagates transgranularly in both the large and the small samples.

4.4.4. Fracture surface analysis

Fractography analysis provides more information regarding the fracture mecha-

nisms which was not seen in the crack profile images. Secondary electron images were taken to analyze the features on the fracture surface. All fracture surface images were taken in the threshold regime. A clear distinction can be observed between the fatigue fracture surface and the monotonic overload surface. In all the fracture surface figures, the direction of crack propagation is upwards.

Figure 4.14 shows the fracture surfaces of the large and small conventional samples. It can be observed that both the large and the small samples display a ductile, featureless fracture surface. Such a featureless surface has observed previously by Morrissey et al [38]. It is not possible to determine from the fracture surfaces if the crack propagation was transgranular or intergranular.

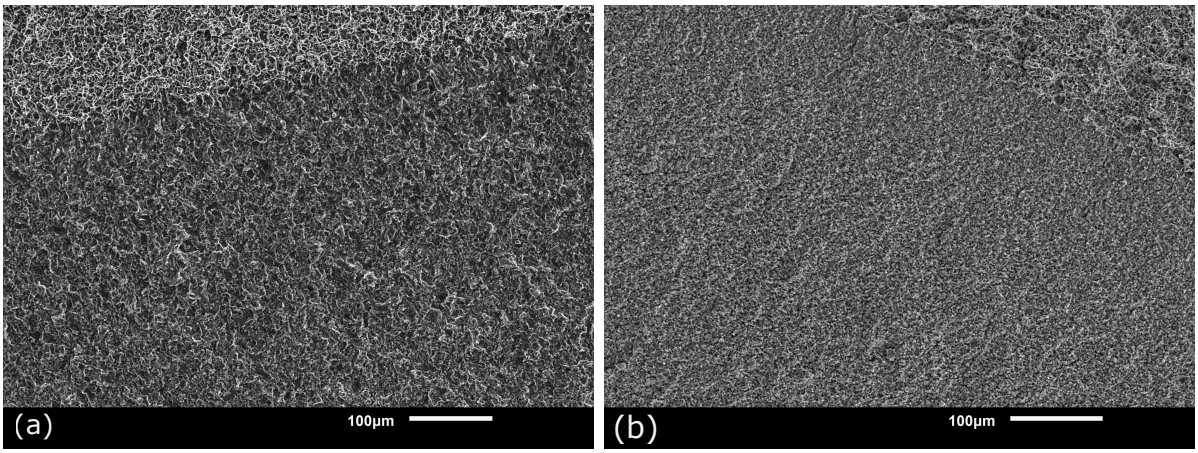


Figure 4.14: SEM micrograph showing the fracture surface of the conventional sample (a) Large, (b) Small.

Figure 4.15 shows the fracture sufaces of the large and small stress relieved samples. It can be seen that the stress relieved fracture surface is completely different from the conventional surface. Features such as ridges and stairs are observed ash shown in the figure for both the large and the small samples.

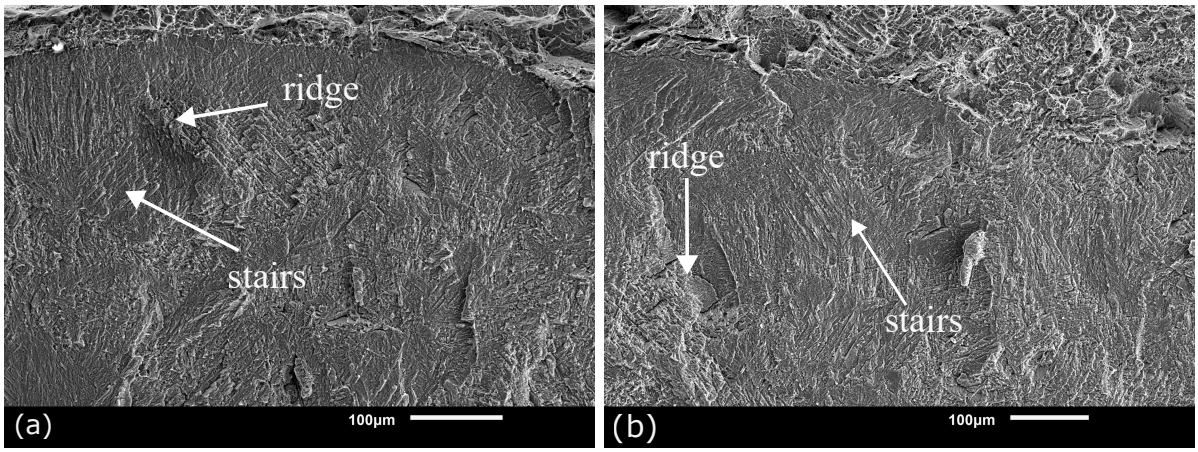


Figure 4.15: SEM micrograph showing the fracture surface of the stress relieved sample (a) Large, (b) Small. White arrows point to stairs and ridges on the surface.

Ridges are characteristic of quasi-cleavage fracture along which the cracks change direction [86]. This is also observed by Becker et al [75]. The stairs on the other hand are characteristic of brittle fracture due to the presence of martensite [87]. Although it is tempting to attribute the stair like features as striations, the spacing between the stairs are too large for the fatigue crack growth rates at this region. The fracture surfaces of the large and small samples are similar which means that in combination with the crack profiles, the fracture mechanism in both the cases are of transgranular and intergranular quasi-cleavage fracture, partly brittle in nature. This explains the lower threshold values of the stress relieved sample.

Figure 4.16 shows the fracture surfaces of the large and small annealed samples. The presence of ridges is clearly observed in both the large and the small samples. However the stair like features in the stress relieved microstructure is not seen in this case.

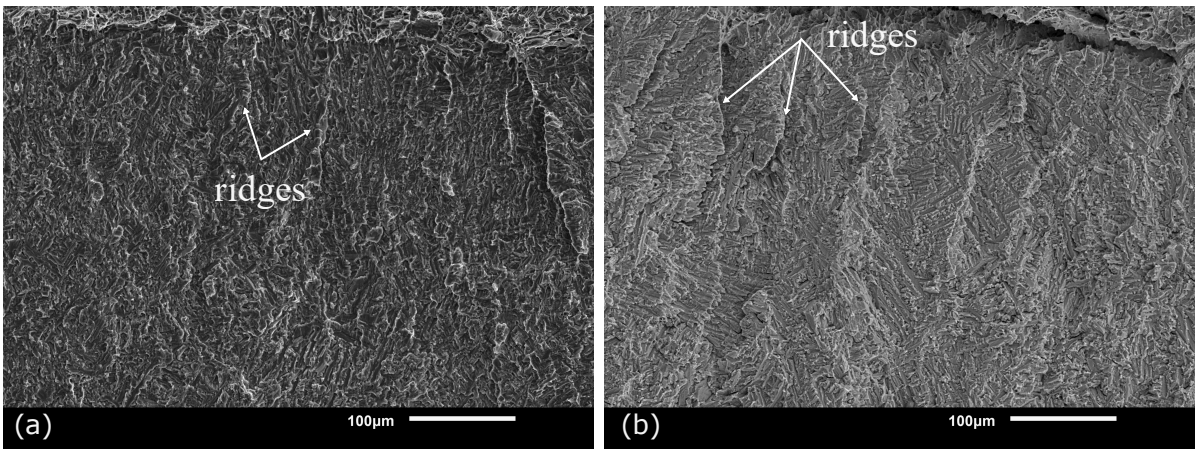


Figure 4.16: SEM micrograph showing the fracture surface of the annealed sample (a)Large, (b) Small. White arrows point to ridges in the surface.

The beta phase plays an important role in increasing the ductility of the material and hence the fatigue threshold. This is seen on the fracture surfaces of the annealed samples as smooth ridge like features. At a glance, although these features look like ridges, under careful observation, they are identified as micro plastic ductile tearing which is shown in Figure 4.17.

This characteristic was also observed by Dhansay in his doctorate thesis [77]. This would mean that in combination with the crack profile, a transgranular quasi-cleavage fracture mechanism which is mostly ductile in nature is seen in the annealed samples resulting in the higher threshold values.

4.4.5. Effect of sample size

The fatigue crack growth rates of the conventional, stress relieved and annealed microstructures while comparing the large and small samples is shown in Figure 4.18. For the conventional microstructure, the threshold values dropped from 2.1 to around 1.6 MPa$\sqrt{m}$ and for the annealed microstructure, the value dropped from 2.6 to 2.1 MPa$\sqrt{m}$ when the small samples were used for testing. On the other hand, the stress

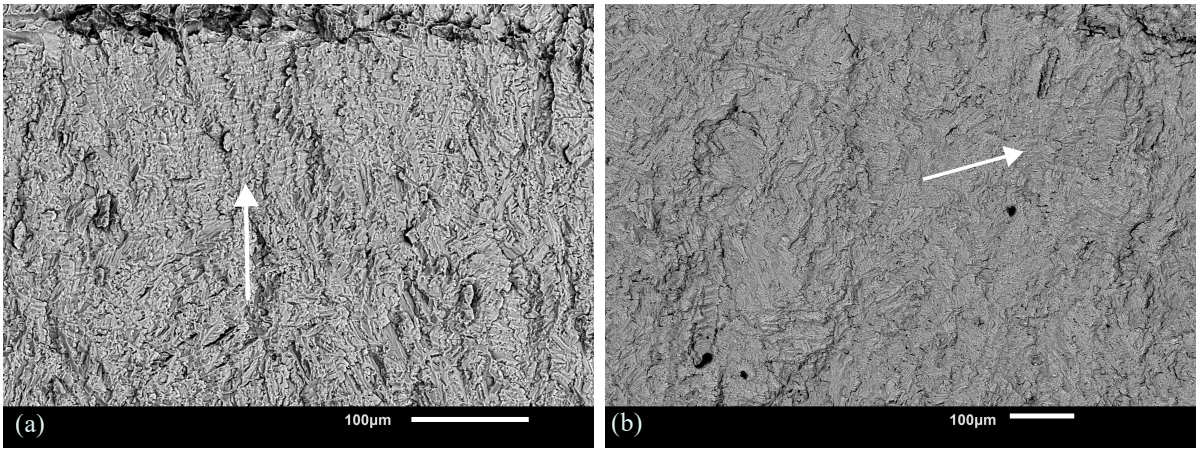


Figure 4.17: SEM micrograph of the annealed fracture surface with the arrow showing ductile tearing in the (a) large, (b) small sample.

relieved microstructure showed the same threshold value of around 1.8 MPa$\sqrt{m}$ for both the large and the small samples. The scatter bands shows a 95% confidence interval with the magenta coloured bands for the large samples and the yellow coloured bands for the small samples. Scatter exists in the fatigue crack growth rate curves for two reasons, the first is the resolution of the DCPD system at small crack length increments. The second is the influence of microstructure. As mentioned previously, the microstructure plays an important role in the crack propagation and hence the fatigue threshold. As the crack never interacts the exact same way with the microstructural features in two different tests, a scatter exists. This scatter could be reduced by performing a number of replicate tests. The variation in threshold values between the large and small samples is hypothesised to be due to the variance of two important mechanisms in the large and the small samples, influence of crack closure and influence of crack tip constraint.

Influence of crack closure

As mentioned previously in chapter 2, there are three main types of crack closure mechanisms namely, plasticity induced crack closure (PICC), Oxide induced crack closure (OICC) and Roughness induced crack closure (RICC). As all tests in this study were performed in a laboratory environment without any influence of harsh conditions, it can be safely assumed that OICC does not have any influence on the fatigue threshold values.

Roughness induced crack closure occurs when there is a mode II type loading on the crack flanks behind the crack tip leading to the closure of the crack. A schematic showing the mechanism of RICC is shown in Figure 4.19.

It can be seen that during one half of the load cycle, the crack is closed due to the roughness of the crack profile. This roughness of the crack surfaces can be attributed to the various crack branching and deflections of the crack profile. As mentioned previously, the crack is is deflected at the α/α' lath boundaries, PBG boundaries and

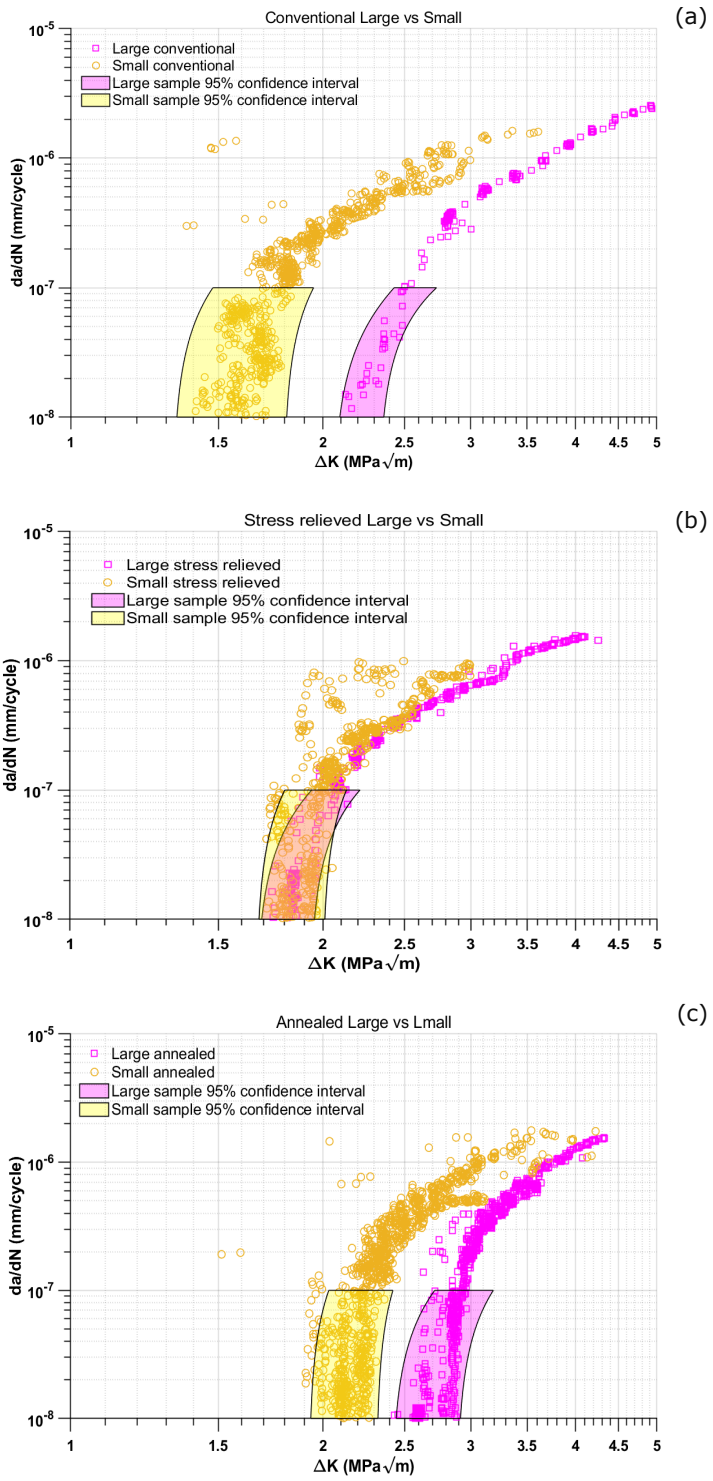


Figure 4.18: Fatigue crack growth rates of a) conventional, b) stress relieved and c) annealed microstructures.

even the equiaxed alpha grain boundaries. Several studies have previously been done correlating the roughness of the fracture surfaces to the amount of RICC [89, 90, 91, 92]. It is believed that that degree of RICC increases with an increase in fracture surface roughness. To get a clear image of the fracture surface morphology,

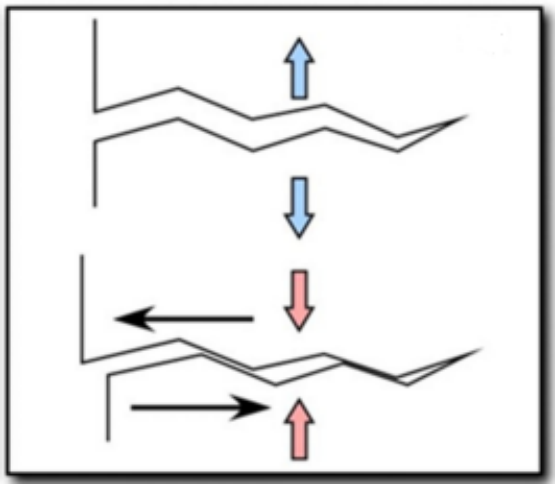


Figure 4.19: Schematic showing the mechanism of roughness induced crack closure. Reproduced from [88].

back scatter election (BSE) images were taken. The BSE fracture surface morphology of the different samples are shown in Figure 4.20.

Figure 4.20a,b shows the fracture surface profiles of the large and small conventional samples. It can be seen that the large sample has a fracture surface with a higher surface roughness than that of the small sample. Figure 4.20c,d shows the fracture surfaces of the large and small stress relieved samples. It can be seen also for the stress relieved microstructures that the fracture surface of the large samples looks rougher than the fracture surface of the small sample. Figure 4.20e,f shows the fracture surfaces of the large and small annealed samples. Once again, following the trend, the large sample shows greater surface roughness than the small sample. Although PBGs play a significant role in the fracture surface mechanisms, they were difficult to spot on the fracture surface itself.

To get a quantified value of surface roughness, ImageJ was utilized. A summary of the fracture surface roughness values measured using the imageJ in the near threshold regime is shown in Table 4.4

As mentioned, the stress relieved microstructure showed the least surface roughness in both the large and the small samples. This could be explained by the display of an intergranular fracture mechanism On the other hand, the conventional microstructure showed the higher surface roughness but only for the large samples. In an interesting trend, the surface roughness of all the microstructures were lower in value in the smaller samples than in the larger samples. For the conventional sample, the roughness dropped from 74 to 51 $\mu m$for the stress relieved sample, the value dropped from 64 to 50 μm and for the annealed sample, the average surface roughness went down from 68 μm to 60 μm. Taking in isolation only the surface roughness values of the large and the small samples could explain the difference in threshold values between the two categories as the larger samples would show a higher degree of RICC. However, it is also important to understand the reason behind why the small samples show a lower roughness. Studies have reported that the fracture surface roughness

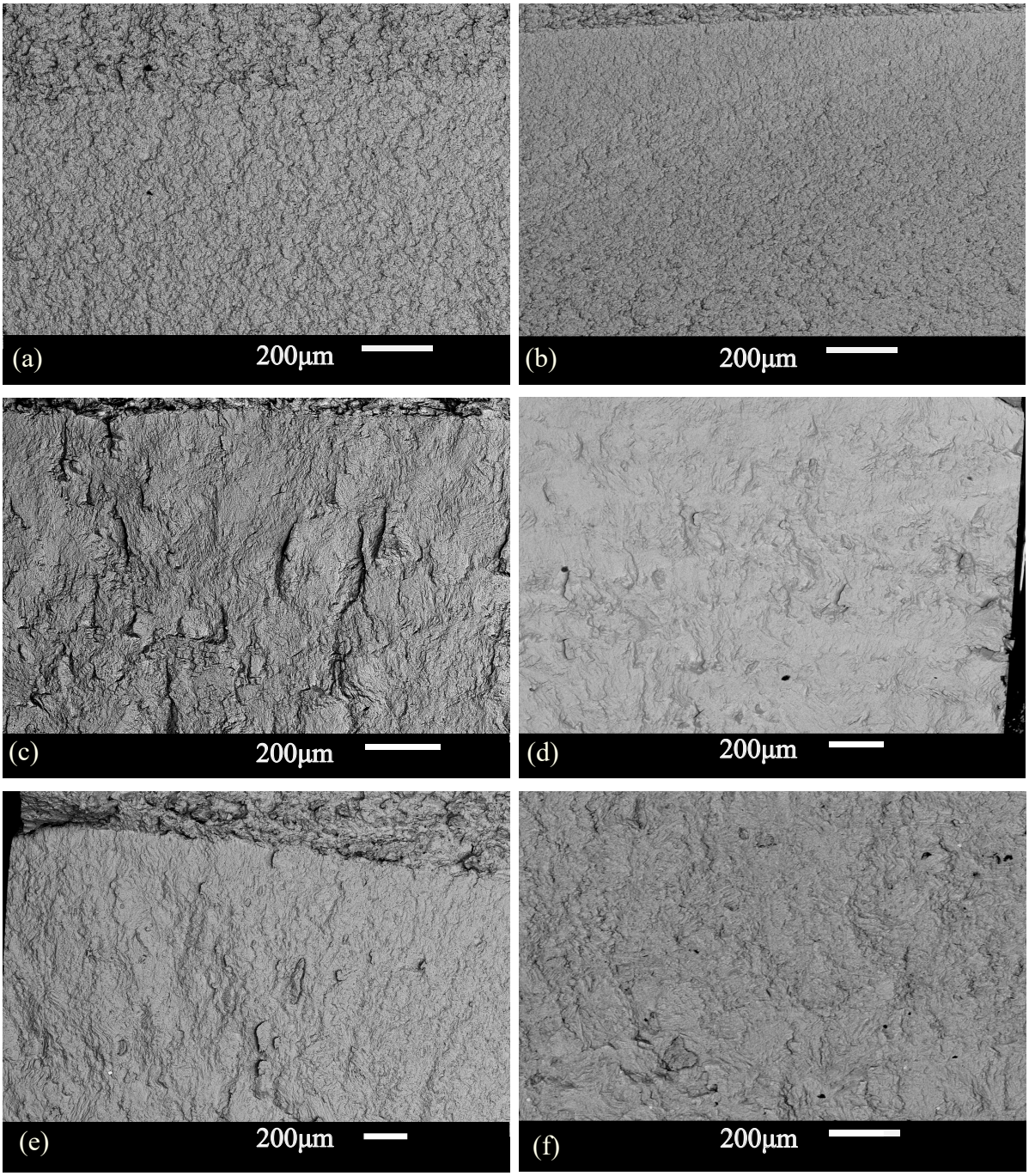


Figure 4.20: BSE micrographs of the fracture surfaces in the threshold regime of a) Large conventional, b) small conventional, c) large stress relieved, d) small stress relieved, e) large annealed and f) small annealed

of a sample would be higher with increased crack deflections and branching [93, 55]. However from the crack profiles shown in Figure 4.11, Figure 4.12 and Figure 4.13, it can be seen that the degree of crack tortuosity is around the same in the large and small samples for the conventional and stress relieved microstructures and higher in the small samples for the annealed microstructure. This would mean that the smaller samples would show around the same degree or higher fracture surface roughness

Table 4.4: Fracture surface roughness of the different samples

Sample	Size	Fracture surface roughness, R_a (μm)
Conventional	Large	74 ± 1
	Small	51 ± 1.6
Stress relieved	Large	64 ± 4
	Small	50 ± 3
Annealed	Large	68 ± 4
	Small	60 ± 2

than the large samples. Hence, although it could be said that RICC could play a small part in the larger samples showing higher thresholds, further research has to be conducted behind the mechanisms playing a role in the same. It is also observed that although the fracture surface roughness of the large and small stress relieved samples are different, they show the same fatigue threshold of 1.8 MPa$\sqrt{m}$. This would suggest that the fracture mechanism could be playing a more prominent role than RICC in the case of intergranular fracture. The role of plasticity induced crack closure is discussed in parallel with the effect of constraint on threshold values in Table 4.4.5.

Influence of constraint

Constraint at the crack tip is defined as the difference between the stress levels obtained from the stress intensity factor and the actual stress state at the crack tip in a multi dimensional sense. This led to the origin of a parameter called T-stress, to balance the variance in stress fields ahead of the crack tip. Therefore, in combination with the stress intensity factor, the T-stresses make up a two parameter description of the 3-dimensional stress field ahead of the crack tip in LEFM. It has also been reported that the amount of constraint is a function of the specimen geometry and the crack depth [94]. For the SENB sample, it has been reported that the sample with a greater crack depth (higher a/W ratios) would experience a higher constraint than the same specimen with a lower crack depth.

The presence of T-stress has a significant effect of the plastic zone size ahead of the crack tip. Studies have found out that an increase in T-stresses which increases the constraint ahead of the crack tip would result in a lower plastic zone size [95, 96]. It is also known that a material in plane stress shows a larger plastic zone size than the same material in plane strain. Hence, in a very crude sense, it can be said that an increase in constraint could be seen as an increase in the degree of plane strain and a decrease in constraint could be seen as an increase in the degree of plane

stress in the material. This difference in the plastic zone size could play a role in the amount of plasticity induced closure in the material affecting the threshold. Blason et al who stuided the effect of sample size on the threshold values of steel reported an increase of threshold values in the smaller samples as a result of lower constraint and hence higher PICC [10]. However, as the geometries used in this study is different, the degree of constraint is different as well. The crack depth at the threshold value for all samples in this study is shown in Table 4.5.

Table 4.5: a/W values at threshold for the different samples

Sample	Large	Small
Conventional	0.31	0.4
Stress relieved	0.3	0.41
Annealed	0.29	0.41

It can be seen that the crack depth at threshold is consistently higher for the small samples regardless of the microstructure. This would mean that the large samples could be showing a slightly higher degree of PICC. To determine this, the degree of crack tunnelling of the crack front was calculated from the fracture surface of all the samples. Fracture surfaces showing the crack fronts is shown in Figure 4.21 - Figure 4.23. The process of determining the degree of crack curvature is by finding the distance between the the crack length at the edges and the crack length in the middle. This is shown in more detail in Appendix B.

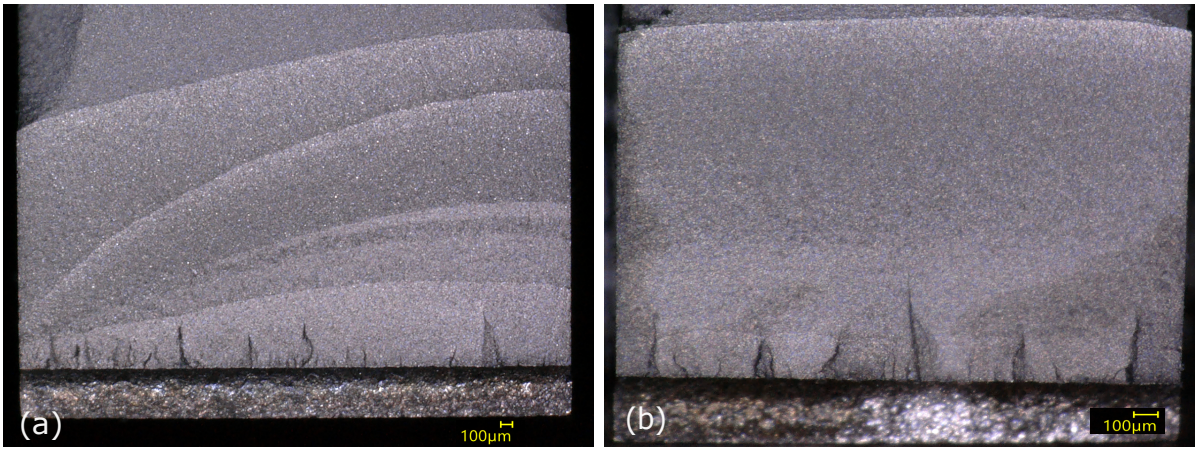


Figure 4.21: Crack front in the conventional sample (a) Large, (b) Small

It can be seen in Figure 4.21 that the crack grew in a very asymmetrical nature. However it was ensured that the level of asymmetry in the crack within the accepted limits as prescribed in the ASTM E647 standard. The accepted limit is given by a

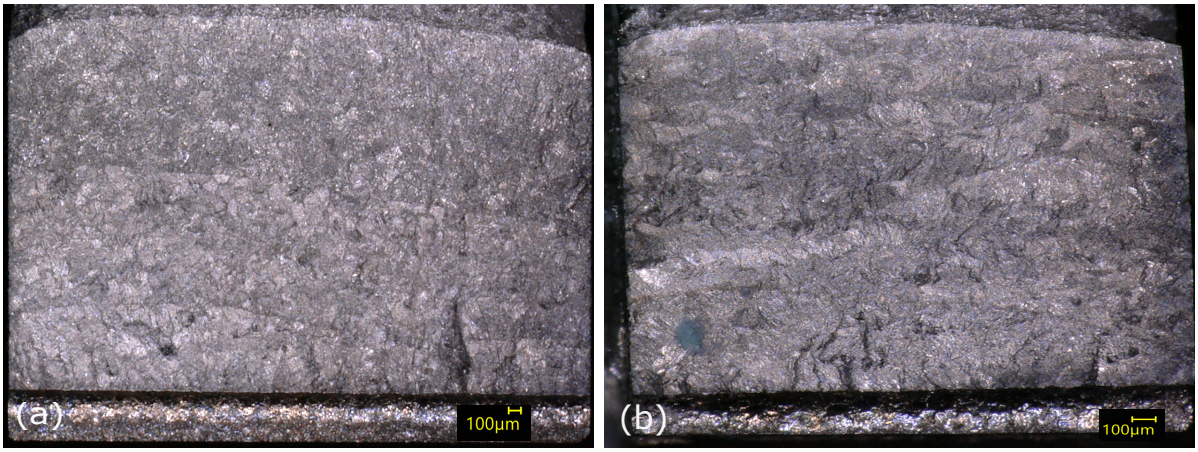


Figure 4.22: Crack front in the stress relieved sample (a) Large, (b) Small

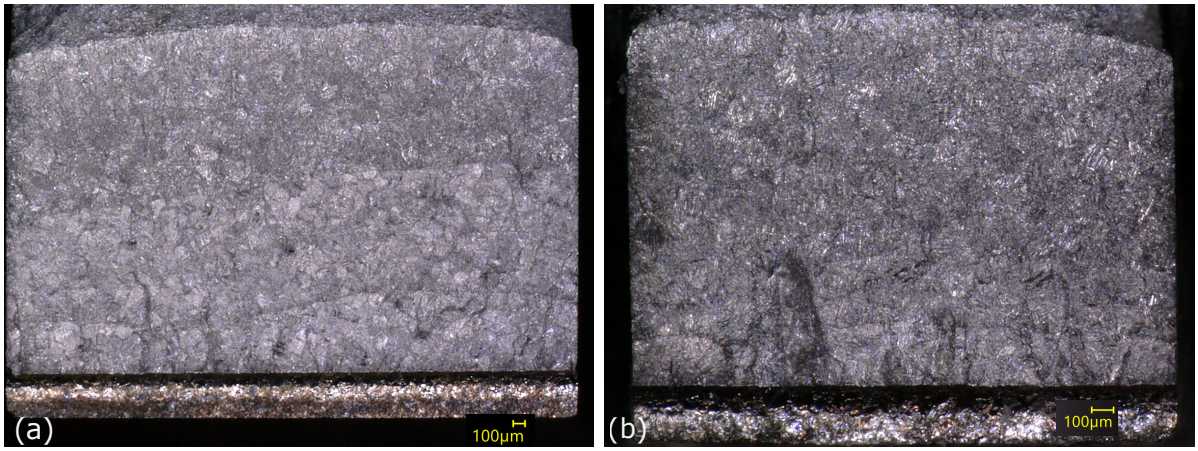


Figure 4.23: Crack front in the annealed sample (a) Large, (b) Small

maximum difference between the crack lengths on the two sides as $0.25B$. A summary of the degree of crack curvature in all the samples is shown in Table 4.6.

Table 4.6: Degree of crack curvature in all samples. All values are in μm.

Sample	Large	Small
Conventional	208	74
Stress relieved	254	127
Annealed	292	169

From Table 4.6, it is seen that the degree of crack curvature is consistently larger for the large samples. This is in agreement with the presented hypothesis of the large samples having a higher degree of plane stress and hence showing more PICC than

the small samples. It should be noted that the presented discussion is only hypothesised and careful research should be conducted using CTOD testing in the future to confirm the same.

Roychowdhury et al studied the effects of T-stresses and specimen dimensions on 3-D crack closure in the small scale yielding regime. The authors reported the following relation of the form

$$\frac{K_{op}}{K_{max}} = F\left(\frac{K_{max}}{\sigma_0\sqrt{B}}, \frac{T_{max}}{\sigma_0}, \frac{z}{B}, \frac{\Delta a}{B}, R, \frac{E_T}{E}, \nu\right) \tag{4.2}$$

where K_{op} is the opening stress intensity factor, σ_0 is the flow stress of the material which is the average of the yield and tensile strengths, B is the thickness, T_{max} is the maximum T stress value ahead of the crack tip, z is the crack length at the centre plane, E_T is the tangential modulus, E is the Young's modulus and ν is the Poisson's ratio of the material. For simplicity, it is assumed that only the first two terms in the function has a size effect. For convenience, the first two terms are also analyzed in isolation. For both the large and the small samples, the Kmax and σ_0 values are the same.

The first term $\frac{K_{max}}{\sigma_0\sqrt{B}}$ is defined as the plastic zone size relative to the thickness of the sample. Lets assume this term to be called as F. This would mean

$$K_{op} = F.K_{max}$$

We know that, $K_{th} = K_{max} - K_{op}$. This would give us

$$K_{th} = K_{max}(1 - F) \tag{4.3}$$

The term F is larger for smaller samples as the thickness is smaller. This would mean, from Equation 4.3 that the value of threshold is greater for the larger samples explained in terms of the plastic zone size in the material which could be an explanation for the results obtained in this study. The same process could be repeated for the second term, $\frac{T_{max}}{\sigma_0}$ giving the same outcome of a higher threshold for the larger samples. However it should be noted that a very simplified form of the model presented by Roychowdhury et al has been assumed to corroborate the results in this study further research regarding the accurate measurements of T stress and opening loads should be performed.

5

Conclusions and future recommendations

5.1. Conclusions

The following conclusions were framed accordingly to answer the research questions put forth in section 2.8.

1. **What are the differences in microstructures of conventionally manufactured and LPBF components subjected to different heat treatments?**

    - The conventional microstructure in the wrought and mill annealed condition showed a microstructure of equiaxed alpha grains. A beta phase fraction of 6.6% was observed.

    - The stress relieved microstructure contains a combination of acicular martensite and lamellar alpha phase with beta phase nucleating at the grain boundaries. Columnar prior beta grains were also identified in the microstructure. A beta phase fraction of 3.5% was observed.

    - The annealed microstructure consisted of a fully lamellar alpha phase with beta phase in the grain boundaries. Columnar prior beta grains and alpha colonies were identified in the microstructure. A beta phase fraction of 7.1% was observed.

2. **What is the influence of microstructure on near threshold fatigue properties?**

    - In the conventional sample, the crack was deflected and branching at the equiaxed grain boundaries showing a fatigue threshold of 2.2±0.1 MPa$\sqrt{m}$ for the large sample. Larger grains increased the distance over which slip takes place, hence increasing the fatigue threshold value.

    - The stress relieved sample showed a threshold of 1.8±0.2 MPa$\sqrt{m}$ for the

large sample. The lower value was due to the presence of acicular martensite which is a very brittle phase reducing the crack tortuosity and promoting intergranular fracture.

- The annealed sample showed a threshold 2.6±0.2 MPa$\sqrt{m}$ for the large sample. The higher value was due to the presence of ductile beta phase and increased crack tortuosity due to the presence of alpha colonies, PBG boundaries and alpha lath boundaries.

3. **What is the influence of sample size on the fatigue threshold value?**

   - It has been hypothesised that for the small samples, the higher value of crack depth at threshold leads to an increase in crack tip constraint resulting in a lower degree of PICC which results in a lower threshold for the small samples. This was also backed up by the degree of crack front curvature with the large sample showing larger curvature. A model developed by Roychowdhury et al also supported this hypothesis [97].

   - The fracture surface roughness showed a consistent trend, reducing in value when small samples were used. Although the roughness values themselves might not be the most accurate as they were measured on ImageJ, the trend of decreasing surface roughness could be accurate.

   - The stress relieved sample did not show any change in threshold value when small samples were used. This was argued to be due to the intergranular fracture mechanism playing a more prominent role than crack closure. The conventional and annealed samples however showed lower threshold values when small samples were used. This was discussed to be due to the decrease in degree of RICC in the small samples. It is still unclear as to which closure mechanism plays a more prominent role in fatigue threshold values.

General conclusions

In this study, a test setup was designed for the near threshold fatigue testing using sub sized samples of conventionally manufactured and LPBF Ti-6Al-4V. The use of smaller samples yielded a fatigue threshold lower by a value of 0.5 MPa$\sqrt{m}$ for 2 out of 3 different types of samples used. Although this slight decrease in threshold value could be found to be negligible but when the component is part of a high precision application or very expensive project, even a slight decrease in fatigue threshold value could prove to be detrimental. In the grand scheme of things, this study shows promising signs in using sub-sized samples to evaluate fatigue properties to reduce material wastage, decrease costs of manufacturing and standardizing additively manufactured part certification.

5.2. Future recommendations

Based on the learning from this study, the following directions are suggested for future research

- The sample sizes could be further scaled down to a size of 17.5x2.5x1.25 mm to check the feasibility to evaluate the fatigue properties.
- Finite element analysis could be performed to check the stress state in front of the crack tip for samples of different sizes to account for the change in fatigue threshold value.
- EBSD analysis could be performed to accurately reconstruct the prior beta grains in the microstructure.
- Sub-sized samples in the duplex annealed condition could be tested to check if the bimodal microstructure has significant effects on the threshold value in the smaller scales.
- CTOD tests could be designed and developed for the small samples to determine the crack opening stress intensity and hence, the amount of crack closure.
- Confocal laser scanning microscopy could be used to accurately measure the fracture surface roughness of the large and small samples to evaluate the influence of roughness induced crack closure.
- The variation and influence of defect population in the small samples on the near threshold fatigue properties could be studied using X-ray computed tomography.
- Digital image correlation tests could be performed and a model could be developed to calculate the T-stress stresses at the crack tip to evaluate the effect of constraint.

A

Fatigue test fixtures drawing

A.1. Large sample fixture drawing

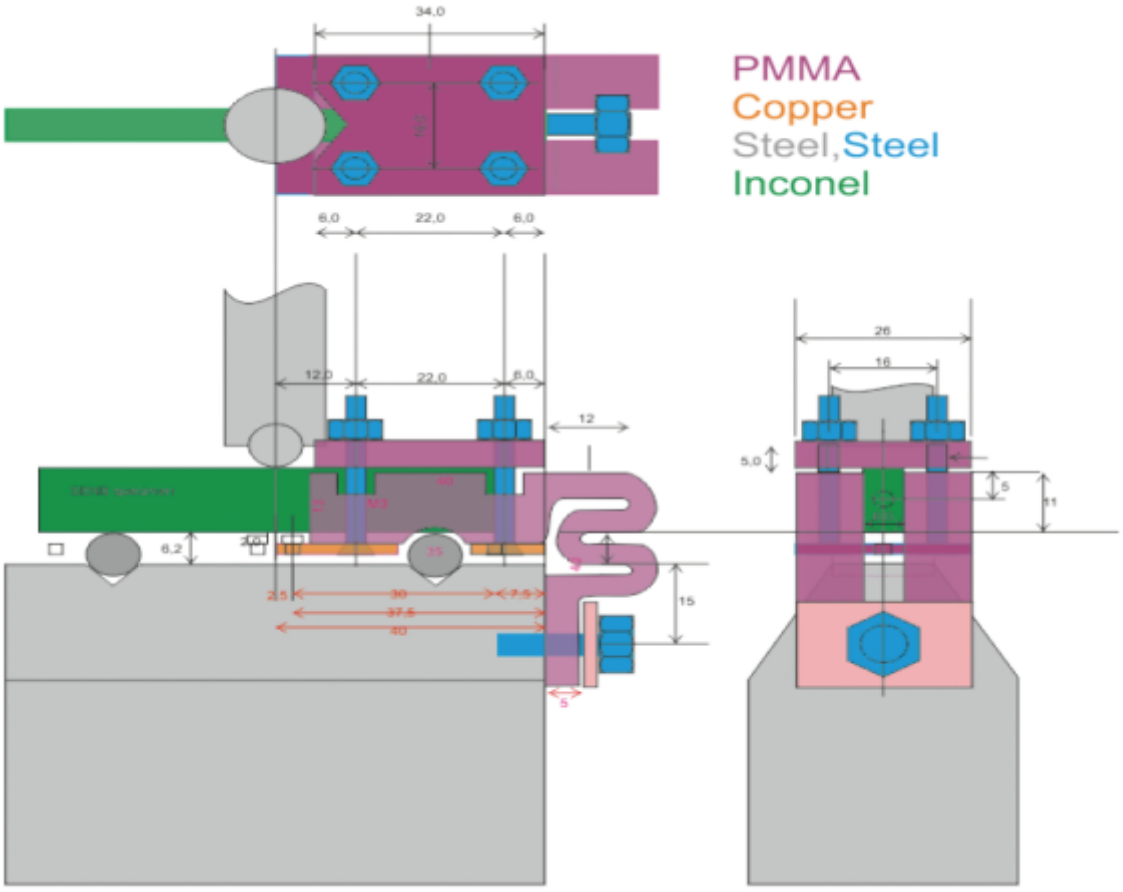


Figure A.1: Drawing of the large sample fixture [98]

A.2. Small sample fixture drawing

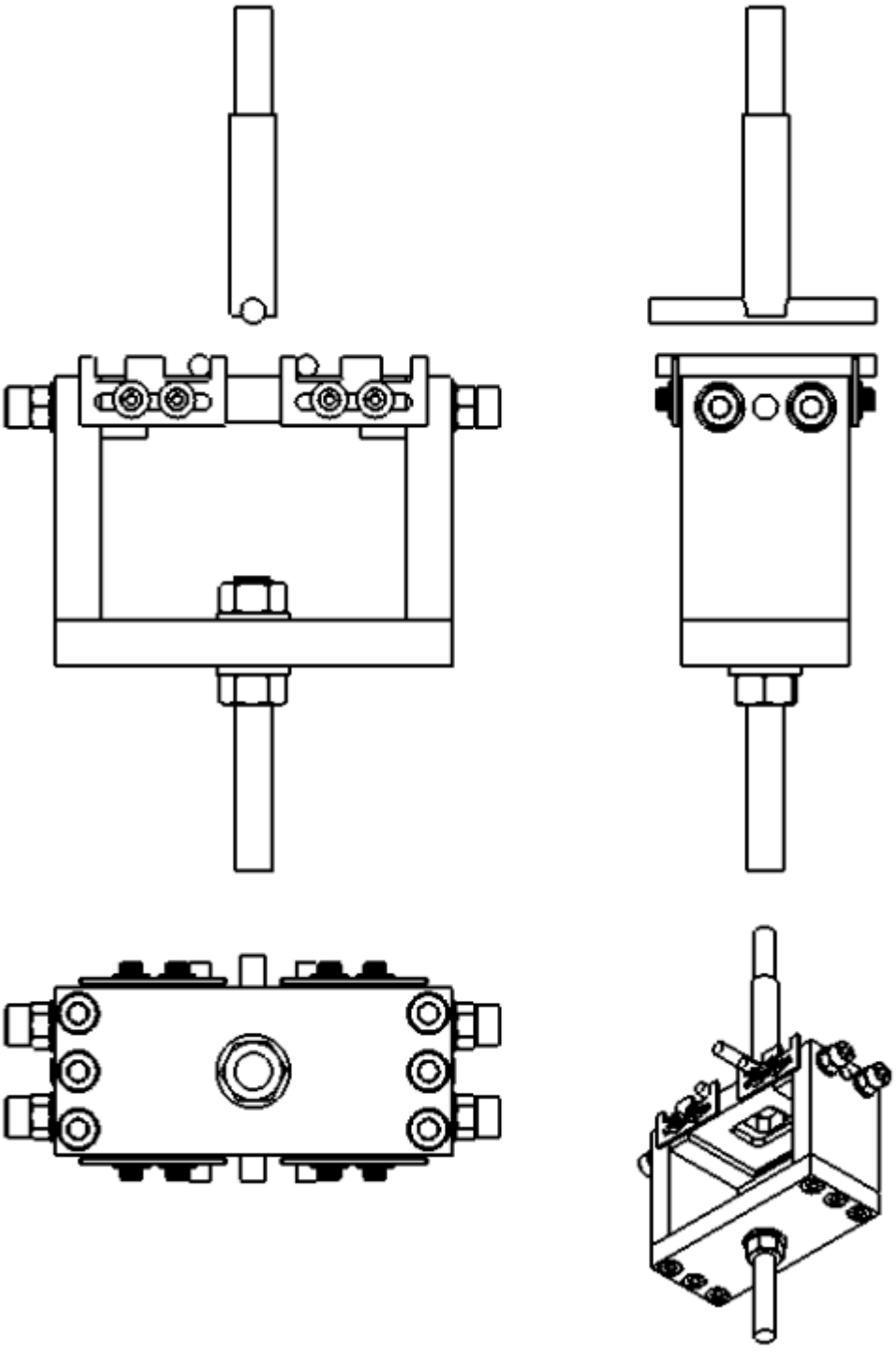


Figure A.2: Drawing of the small sample fixture

B

Crack curvature measurement

Figure B.1 shows the accurate measurement of the degree of crack curvature in the large stress relieved sample. The same procedure was employed for all samples.

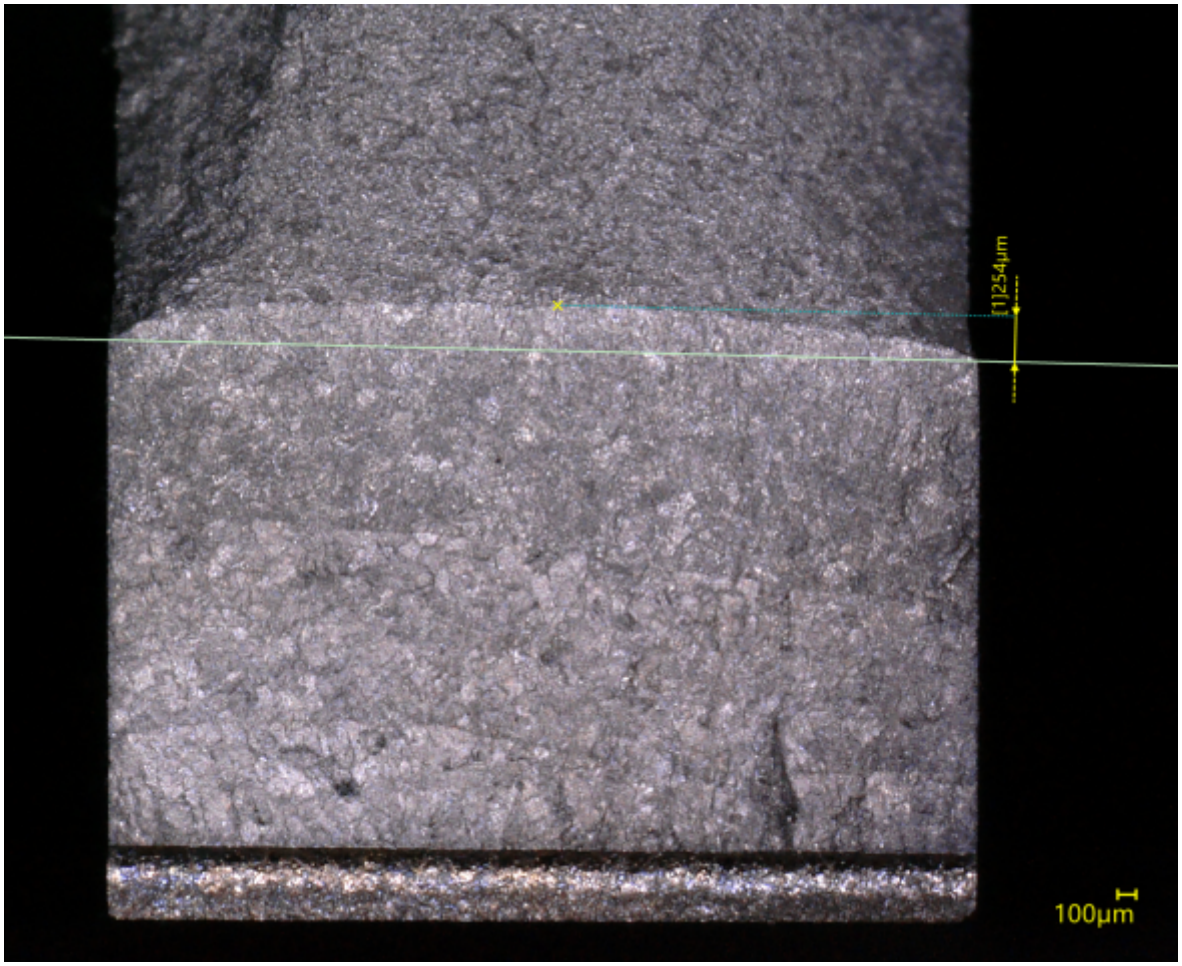


Figure B.1: Measurement of crack curvature in the large stress relieved sample

C

Validity of fatigue tests

To check the validity of the fatigue tests, a constant ΔK test was performed. In a constant ΔK test, as the crack grows, the applied stress intensity is maintained at a constant and the da/dN is calculated as a function of the crack length. The result from the constant ΔK test is shown in Figure C.1.

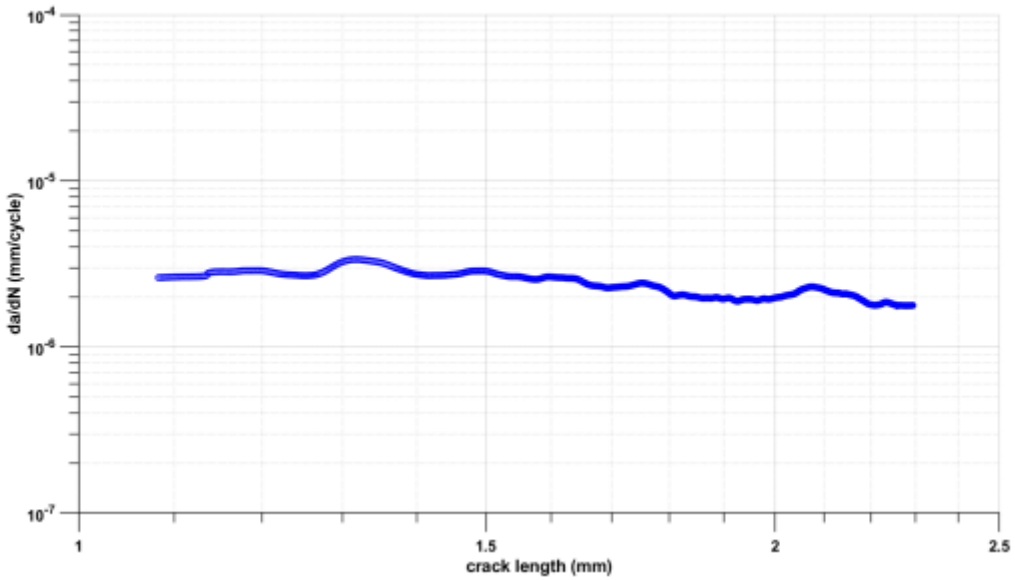


Figure C.1: Constant ΔK test result.

It can be seen that although the da/dN value is fairly constant over the entire test with slight variations. These variations is a result of a combination of two factors. The first factor is the resolution and noise of the DCPD system. The second factor is due to human error with DCPD calibration during visual inspection of the crack length in the pre-fatigue stage. This reduce in accuracy could explain the presence of the scatter bands in the FCGR curves in Figure 4.18.

D

Matlab codes

The first step reduces the data per cycle.

```
function [ a , n , delP]=reducean ( cracklength , cycles , force , ...
    skipvariable )%Input
%variables in order: peak valley cracklength, force is force values
%peak valey segment(not cycle) number ,peak -valley force values ,a ...
    skip
 %variable to skip data points in case of too many data points
 [ maxdata ,~]= size ( cracklength ) ; %to find out the size of the ...
     input
%variables
 %Initialize all variables to be used
 a=zeros (100000 ,1) ;
 tempa=zeros (100000 ,1) ;
 tempn=zeros (100000 ,1) ;
n=zeros (100000 ,1) ;
delP=zeros (10000 ,1) ;
 tempdelP=zeros (100000 ,1) ;
 i=1;
 j=1;

 while j<maxdata %move along the input variables till last
 tempdelP (i)=abs ( force (j)-force (j+1) ) ; %calculate Δ P
 tempn (i)=floor ( cycles (j+1) /2) ; %calualte cycle number
 tempa (i)=(cracklength (j)+cracklength (j+1) ) / 2; %calculate average
%crack length in that cycle
 j=j+2; %increment j by 2 as in the input file two data points will be
%transformed to one
 i=i+1;%increment i by 1 as this is the output variable
 end

 k=1;
 w=1;
 [ newmax ,~]= size ( tempdelP ) ; %calculate size of newly formed Δ P
%variable
 while k<newmax %procedure to skip datapoints
 delP (w)=tempdelP (k) ; %save temporary variable values to final ...
     output
```

```
%variables
 n(w)=tempn (k) ;
 a(w)=tempa (k) ;
 k=k+skipvariable ; %skip data points here
 w=w+1;
 end
 delP=delP ( delP~=0) ; %since the variables were initialized by zeros ...
     , this
%removes the remaining zeros
 n=n(n~=0) ;
 a=a(a~=0) ;
end
```

The second step and final step uses the reduced data from the previous step to obtain the da/dn vs ΔK values.

```
function [dadn, del_K]=dadnsecant(B,W,cracklength,n,del_P,offset)
%offset is the amount of data to skip
%For average crack length
S=25;calcID=offset; %For small samples. S for large samples is ...
    different
dadn=[];del_PP=[];cracklength_avg=[];del_K=[];j=1;i=1;
for i=1:size(cracklength,1)-1
    if i==calcID
dadn(j,1)=(cracklength(i+1)-cracklength(i+1-offset))/(n(i+1)-n(i+1-offset));
del_PP=(del_P(i+1)+del_P(i+1-offset))/2;
%del_PP=del_P(i-1);
cracklength_avg=(cracklength(i+1)+cracklength(i+1-offset))/2;
ff=geometric(cracklength_avg./W);
disp([cracklength_avg ff del_PP del_P(i+1) del_P(i+1-offset) i]);
%0.0361 conversion from N mm to MPa m
del_K(j,1)=((del_PP.*ff.*S)./(B*(W^(3/2))))/31.6228;
j=j+1;calcID=calcID+offset;
    end
end

end
```

Bibliography

[1] Shunyu Liu and Yung C. Shin. “Additive manufacturing of Ti6Al4V alloy: A review”. In: *Materials & Design* 164 (Feb. 2019), p. 107552. ISSN: 0264-1275. DOI: 10.1016/J.MATDES.2018.107552.

[2] Paramjit Singh, Harish Pungotra, and Nirmal S. Kalsi. “On the characteristics of titanium alloys for the aircraft applications”. In: *Materials Today: Proceedings* 4.8 (2017), pp. 8971–8982. ISSN: 22147853. DOI: 10.1016/j.matpr.2017.07.249. URL: https://doi.org/10.1016/j.matpr.2017.07.249.

[3] Yu Lin Hao, Shu Jun Li, and Rui Yang. “Biomedical titanium alloys and their additive manufacturing”. In: *Rare Metals* 35.9 (2016), pp. 661–671. ISSN: 18677185. DOI: 10.1007/s12598-016-0793-5.

[4] A. S. Oryshchenko et al. “Marine titanium alloys: Present and future”. In: *Inorganic Materials: Applied Research* 6.6 (2015), pp. 571–579. ISSN: 2075115X. DOI: 10.1134/S2075113315060106.

[5] Runze Huang et al. “Energy and emissions saving potential of additive manufacturing: the case of lightweight aircraft components”. In: *Journal of Cleaner Production* 135 (Nov. 2016), pp. 1559–1570. ISSN: 0959-6526. DOI: 10.1016/J.JCLEPRO.2015.04.109.

[6] Michael Janssen, Jan Zuidema, and Russel Wanhill. *Fracture Mechanics*. 2nd Editio. CRC Press, 2002. ISBN: 9781402068072.

[7] R. J. Puigh et al. “Miniaturized fatigue crack growth specimen technology and results”. In: *Journal of Nuclear Materials* 104.C (Jan. 1981), pp. 1501–1504. ISSN: 0022-3115. DOI: 10.1016/0022-3115(82)90812-1.

[8] D.A Mervyn and A. M. Ermi. “Miniature specimen technology for postirradiation fatigue crack growth testing”. In: *IEEE* 4 (1979).

[9] T. Tsuchiya et al. “Tensile and tensile-mode fatigue testing of microscale specimens in constant humidity environment”. In: *Experimental Mechanics* 50.4 (Apr. 2010), pp. 509–516. ISSN: 00144851. DOI: 10.1007/S11340-009-9258-1/FIGURES/11. URL: https://link-springer-com.tudelft.idm.oclc.org/article/10.1007/s11340-009-9258-1.

[10] Sergio Blasón et al. “Determination of fatigue crack growth in the near-threshold regime using small-scale specimens”. In: *Theoretical and Applied Fracture Mechanics* 118.December 2021 (2022). ISSN: 01678442. DOI: 10.1016/j.tafmec.2021.103224.

[11] Bartłomiej Wysocki et al. “Laser and Electron Beam Additive Manufacturing Methods of Fabricating Titanium Bone Implants”. In: *Applied Sciences 2017, Vol. 7, Page 657* 7.7 (June 2017), p. 657. ISSN: 2076-3417. DOI: 10.3390/APP7070657. URL: https://www.mdpi.com/2076-3417/7/7/657/htm%20https://www.mdpi.com/2076-3417/7/7/657.

[12] *Empa - Coating Competence Center - Selective Laser Melting (SLM)*. URL: https://www.empa.ch/web/coating-competence-center/selective-laser-melting.

[13] S. Kumar. *Selective Laser Sintering/Melting*. Vol. 10. Elsevier, 2014, pp. 93–134. ISBN: 9780080965338. DOI: 10.1016/B978-0-08-096532-1.01003-7. URL: http://dx.doi.org/10.1016/B978-0-08-096532-1.01003-7.

[14] H. Shipley et al. “Optimisation of process parameters to address fundamental challenges during selective laser melting of Ti-6Al-4V: A review”. In: *International Journal of Machine Tools and Manufacture* 128.January (2018), pp. 1–20. ISSN: 08906955. DOI: 10.1016/j.ijmachtools.2018.01.003. URL: https://doi.org/10.1016/j.ijmachtools.2018.01.003.

[15] Silvia Vock et al. “Powders for powder bed fusion: a review”. In: *Progress in Additive Manufacturing* 4.4 (Dec. 2019), pp. 383–397. ISSN: 23639520. DOI: 10.1007/S40964-019-00078-6.

[16] Erfan Maleki, Sara Bagherifard, and Mario Guagliano. “Application of artificial intelligence to optimize the process parameters effects on tensile properties of Ti-6Al-4V fabricated by laser powder-bed fusion”. In: *International Journal of Mechanics and Materials in Design* 18 (2022), pp. 199–222. DOI: 10.1007/s10999-021-09570-w. URL: https://doi.org/10.1007/s10999-021-09570-w.

[17] Haider Ali et al. “In-situ residual stress reduction, martensitic decomposition and mechanical properties enhancement through high temperature powder bed preheating of Selective Laser Melted Ti6Al4V”. In: *Materials Science and Engineering: A* 695 (May 2017), pp. 211–220. ISSN: 0921-5093. DOI: 10.1016/J.MSEA.2017.04.033.

[18] Xianfeng Xiao et al. “Progress on Experimental Study of Melt Pool Flow Dynamics in Laser Material Processing”. In: *Liquid Metals* (Apr. 2021). DOI: 10.5772/INTECHOPEN.97205. URL: https://www.intechopen.com/chapters/76127.

[19] I. Yadroitsev, P. Krakhmalev, and I. Yadroitsava. “Selective laser melting of Ti6Al4V alloy for biomedical applications: Temperature monitoring and microstructural evolution”. In: *Journal of Alloys and Compounds* 583 (2014), pp. 404–409. ISSN: 09258388. DOI: 10.1016/j.jallcom.2013.08.183. URL: http://dx.doi.org/10.1016/j.jallcom.2013.08.183.

[20] Samy Hocine et al. “Operando X-ray diffraction during laser 3D printing”. In: *Materials Today* 34 (Apr. 2020), pp. 30–40. ISSN: 1369-7021. DOI: 10.1016/J.MATTOD.2019.10.001.

[21] Bi Zhang, Yongtao Li, and Qian Bai. “Defect Formation Mechanisms in Selective Laser Melting: A Review”. In: *Chinese Journal of Mechanical Engineering (English Edition)* 30.3 (May 2017), pp. 515–527. ISSN: 21928258. DOI: 10.1007/S10033-017-0121-5/FIGURES/17. URL: https://link.springer.com/articles/10.1007/s10033-017-0121-5%20https://link.springer.com/article/10.1007/s10033-017-0121-5.

[22] P. Li et al. “Critical assessment of the fatigue performance of additively manufactured Ti–6Al–4V and perspective for future research”. In: *International Journal of Fatigue* 85 (Apr. 2016), pp. 130–143. ISSN: 0142-1123. DOI: 10.1016/J.IJFATIGUE.2015.12.003.

[23] P. Edwards and M. Ramulu. “Fatigue performance evaluation of selective laser melted Ti-6Al-4V”. In: *Materials Science and Engineering A* 598 (Mar. 2014), pp. 327–337. ISSN: 09215093. DOI: 10.1016/J.MSEA.2014.01.041. URL: http://dx.doi.org/10.1016/j.msea.2014.01.041.

[24] Zhuoer Chen et al. *Additive Manufacturing for the Aerospace Industry*. Elsevier, Jan. 2019, pp. 283–299. ISBN: 9780128140635. DOI: 10.1016/B978-0-12-814062-8.00015-7.

[25] Aref Yadollahi and Nima Shamsaei. “Additive manufacturing of fatigue resistant materials: Challenges and opportunities”. In: *International Journal of Fatigue* 98 (May 2017), pp. 14–31. ISSN: 0142-1123. DOI: 10.1016/J.IJFATIGUE.2017.01.001.

[26] P. J. Withers and H. K.D.H. Bhadeshia. “Residual stress part 1 - Measurement techniques”. In: *Materials Science and Technology* 17.4 (2001), pp. 355–365. ISSN: 02670836. DOI: 10.1179/026708301101509980.

[27] Peter Mercelis and Jean Pierre Kruth. “Residual stresses in selective laser sintering and selective laser melting”. In: *Rapid Prototyping Journal* 12.5 (2006), pp. 254–265. ISSN: 13552546. DOI: 10.1108/13552540610707013.

[28] Tatiana Mishurova et al. “Exploring the Correlation between Subsurface Residual Stresses and Manufacturing Parameters in Laser Powder Bed Fused Ti-6Al-4V”. In: *Metals 2019, Vol. 9, Page 261* 9.2 (Feb. 2019), p. 261. ISSN: 2075-4701. DOI: 10.3390/MET9020261. URL: https://www.mdpi.com/2075-4701/9/2/261/htm%20https://www.mdpi.com/2075-4701/9/2/261.

[29] S. Leuders et al. “On the mechanical behaviour of titanium alloy TiAl6V4 manufactured by selective laser melting: Fatigue resistance and crack growth performance”. In: *International Journal of Fatigue* 48 (Mar. 2013), pp. 300–307. ISSN: 0142-1123. DOI: 10.1016/J.IJFATIGUE.2012.11.011.

[30] Galina Kasperovich and Joachim Hausmann. “Improvement of fatigue resistance and ductility of TiAl6V4 processed by selective laser melting”. In: *Journal of Materials Processing Technology* 220 (June 2015), pp. 202–214. ISSN: 0924-0136. DOI: 10.1016/J.JMATPROTEC.2015.01.025.

[31] G. Lütjering. “Influence of processing on microstructure and mechanical properties of (α+β) titanium alloys”. In: *Materials Science and Engineering: A* 243.1-2 (Mar. 1998), pp. 32–45. ISSN: 0921-5093. DOI: 10.1016/S0921-5093(97)00778-8.

[32] Trina Majumdar et al. “Understanding the effects of PBF process parameter interplay on Ti-6Al-4V surface properties”. In: *PLoS ONE* 14.8 (2019), pp. 1–24. ISSN: 19326203. DOI: 10.1371/journal.pone.0221198.

[33] T. Ahmed and H. J. Rack. “Phase transformations during cooling in α+β titanium alloys”. In: *Materials Science and Engineering: A* 243.1-2 (Mar. 1998), pp. 206–211. ISSN: 0921-5093. DOI: 10.1016/S0921-5093(97)00802-2.

[34] Gerrit Matthys Ter Haar and Thorsten H Becker. “Selective Laser Melting Produced Ti-6Al-4V : Post-Process Heat Treatments to Achieve Superior Tensile Properties”. In: *Materials* 11.146 (2018). DOI: 10.3390/ma11010146.

[35] Yanzhou Ji et al. “Theoretical Assessment on the Phase Transformation Kinetic Pathways of Multi-component Ti Alloys : Application to Ti-6Al-4V”. In: *Journal of Phase Equilibria and Diffusion* 37.1 (2016), pp. 53–64. ISSN: 1863-7345. DOI: 10.1007/s11669-015-0436-9.

[36] G. Q. Wu et al. “Effect of microstructure on the fatigue properties of Ti–6Al–4V titanium alloys”. In: *Materials & Design* 46 (Apr. 2013), pp. 668–674. ISSN: 0261-3069. DOI: 10.1016/J.MATDES.2012.10.059.

[37] R K Nalla et al. “Influence of Microstructure on High-Cycle Fatigue of Ti-6Al-4V : Bimodal vs . Lamellar Structures”. In: 33.March (2002), pp. 899–918.

[38] R. J. Morrissey, D. L. McDowell, and T. Nicholas. “Frequency and stress ratio effects in high cycle fatigue of Ti-6Al-4V”. In: *International Journal of Fatigue* 21.7 (Aug. 1999), pp. 679–685. ISSN: 0142-1123. DOI: 10.1016/S0142-1123(99)00030-4.

[39] Justin Mezzetta et al. “Microstructure-Properties Relationships of Ti-6Al-4V Parts Fabricated by Selective Laser Melting”. In: *International Journal of Precision Engineering and Manufacturing-Green Technology* 5.5 (2018), pp. 605–612. DOI: 10.1007/s40684-018-0062-1.

[40] Lore Thijs et al. “A study of the microstructural evolution during selective laser melting of Ti–6Al–4V”. In: *Acta Materialia* 58.9 (May 2010), pp. 3303–3312. ISSN: 1359-6454. DOI: 10.1016/J.ACTAMAT.2010.02.004.

[41] T. Vilaro, C. Colin, and J. D. Bartout. “As-fabricated and heat-treated microstructures of the Ti-6Al-4V alloy processed by selective laser melting”. In: *Metallurgical and Materials Transactions A: Physical Metallurgy and Materials Science* 42.10 (2011), pp. 3190–3199. ISSN: 10735623. DOI: 10.1007/s11661-011-0731-y.

[42] Bey Vrancken et al. “Heat treatment of Ti6Al4V produced by Selective Laser Melting: Microstructure and mechanical properties”. In: *Journal of Alloys and Compounds* 541 (Nov. 2012), pp. 177–185. ISSN: 0925-8388. DOI: 10.1016/J.JALLCOM.2012.07.022.

[43] Gerrit Matthys Ter Haar and Thorsten H Becker. “Low temperature stress relief and martensitic decomposition in selective laser melting produced Ti6Al4V”. In: *Materials Design and Processing Communications* November 2019 (2021), pp. 2–7. DOI: 10.1002/mdp2.138.

[44] E. Sallica-Leva et al. “Ductility improvement due to martensite α' decomposition in porous Ti–6Al–4V parts produced by selective laser melting for orthopedic implants”. In: *Journal of the Mechanical Behavior of Biomedical Materials* 54 (Feb. 2016), pp. 149–158. ISSN: 1751-6161. DOI: 10.1016/J.JMBBM.2015.09.020.

[45] Luca Facchini et al. “Ductility of a Ti-6Al-4V alloy produced by selective laser melting of prealloyed powders”. In: *Rapid Prototyping Journal* 16.6 (2010), pp. 450–459. ISSN: 13552546. DOI: 10.1108/13552541011083371.

[46] M. Thöne et al. “Influence of Heat-Treatment of Selective Laser Melting Products - e.g. Ti6Al4V”. In: *International Solid Freeform Fabrication Symposium*. 2012, pp. 492–498. URL: http://dx.doi.org/10.26153/tsw/15368.

[47] Qianli Huang et al. “Specific heat treatment of selective laser melted Ti–6Al–4V for biomedical applications”. In: *Frontiers of Materials Science* 9.4 (2015), pp. 373–381. ISSN: 20950268. DOI: 10.1007/s11706-015-0315-7.

[48] V. Cain et al. “Crack propagation and fracture toughness of Ti6Al4V alloy produced by selective laser melting”. In: *Additive Manufacturing* 5 (Jan. 2015), pp. 68–76. ISSN: 2214-8604. DOI: 10.1016/J.ADDMA.2014.12.006.

[49] Anatoliy Popovich et al. “Microstructure and mechanical properties of Ti-6AL-4V manufactured by SLM”. In: *Key Engineering Materials* 651-653 (2015), pp. 677–682. ISSN: 16629795. DOI: 10.4028/www.scientific.net/KEM.651-653.677.

[50] Qi Chao, Peter D. Hodgson, and Hossein Beladi. “Ultrafine grain formation in a Ti-6Al-4V alloy by thermomechanical processing of a martensitic microstructure”. In: *Metallurgical and Materials Transactions A: Physical Metallurgy and Materials Science* 45.5 (2014), pp. 2659–2671. ISSN: 10735623. DOI: 10.1007/s11661-014-2205-5.

[51] Xiang Yu Zhang et al. “Effect of subtransus heat treatment on the microstructure and mechanical properties of additively manufactured Ti-6Al-4V alloy”. In: *Journal of Alloys and Compounds* 735 (Feb. 2018), pp. 1562–1575. ISSN: 0925-8388. DOI: 10.1016/J.JALLCOM.2017.11.263.

[52] I. Katzarov, S. Malinov, and W. Sha. “Finite element modeling of the morphology of β to α phase transformation in Ti-6Al-4V alloy”. In: *Metallurgical and Materials Transactions A: Physical Metallurgy and Materials Science* 33.4 (2002), pp. 1027–1040. ISSN: 10735623. DOI: 10.1007/s11661-002-0204-4.

[53] R. Pederson et al. “Use of high temperature X-ray diffractometry to study phase transitions and thermal expansion properties in Ti-6Al-4V”. In: *Materials Science and Technology* 19.11 (2003), pp. 1533–1538. ISSN: 02670836. DOI: 10.1179/026708303225008013.

[54] F. J. Gil et al. “Formation of α-Widmanstätten structure: Effects of grain size and cooling rate on the Widmanstätten morphologies and on the mechanical properties in Ti6Al4V alloy”. In: *Journal of Alloys and Compounds* 329.1-2 (2001), pp. 142–152. ISSN: 09258388. DOI: 10.1016/S0925-8388(01)01571-7.

[55] Punit Kumar and Upadrasta Ramamurty. “Microstructural optimization through heat treatment for enhancing the fracture toughness and fatigue crack growth resistance of selective laser melted Ti6Al4V alloy”. In: *Acta Materialia* 169 (May 2019), pp. 45–59. ISSN: 1359-6454. DOI: 10.1016/J.ACTAMAT.2019.03.003.

[56] W. Xu et al. “In situ tailoring microstructure in additively manufactured Ti-6Al-4V for superior mechanical performance”. In: *Acta Materialia* 125 (2017), pp. 390–400. ISSN: 13596454. DOI: 10.1016/j.actamat.2016.12.027.

[57] Marlo Simonelli, Yau Yau Tse, and C Tuck. “The formation of α + β microstructure in as-fabricated selective laser melting of Ti-6Al-4V”. In: *Journal of Materials Research* 29.17 (2014), pp. 2028–2035. DOI: 10.1557/jmr.2014.166.

[58] W. Xu et al. “Additive manufacturing of strong and ductile Ti-6Al-4V by selective laser melting via in situ martensite decomposition”. In: *Acta Materialia* 85 (2015), pp. 74–84. ISSN: 13596454. DOI: 10.1016/j.actamat.2014.11.028.

[59] M. Benedetti et al. “The effect of post-sintering treatments on the fatigue and biological behavior of Ti-6Al-4V ELI parts made by selective laser melting”. In: *Journal of the Mechanical Behavior of Biomedical Materials* 71.February (2017), pp. 295–306. ISSN: 18780180. DOI: 10.1016/j.jmbbm.2017.03.024. URL: http://dx.doi.org/10.1016/j.jmbbm.2017.03.024.

[60] Chunlei Qiu, Nicholas J.E. Adkins, and Moataz M. Attallah. “Microstructure and tensile properties of selectively laser-melted and of HIPed laser-melted Ti-6Al-4V”. In: *Materials Science and Engineering A* 578 (2013), pp. 230–239. ISSN: 09215093. DOI: 10.1016/j.msea.2013.04.099. URL: http://dx.doi.org/10.1016/j.msea.2013.04.099.

[61] Jingjing Yang et al. “Formation and control of martensite in Ti-6Al-4V alloy produced by selective laser melting”. In: *Materials & Design* 108 (Oct. 2016), pp. 308–318. ISSN: 0264-1275. DOI: 10.1016/J.MATDES.2016.06.117.

[62] M Simonelli, Y Y Tse, and C Tuck. “Effect of the build orientation on the mechanical properties and fracture modes of SLM Ti – 6Al – 4V”. In: *Materials Science & Engineering A* 616 (2014), pp. 1–11. ISSN: 0921-5093. DOI: 10.1016/j.msea.2014.07.086. URL: http://dx.doi.org/10.1016/j.msea.2014.07.086.

[63] P. Paris and F. Erdogan. “A critical analysis of crack propagation laws”. In: *Journal of Basic Engineering* 85.4 (1963), pp. 528–533. ISSN: 1528901X. DOI: 10.1115/1.3656900.

[64] *Fracture mechanics - Wikipedia*. URL: https://en.wikipedia.org/wiki/Fracture_mechanics.

[65] T. L. Anderson. *Fracture mechanics : fundamentals and applications*. Boca Raton : CRC Press/Taylor & Francis, 2017, xvii, 661 pages : ISBN: 9781498728133.

[66] Russel Wanhill, Simon Barter, and Loris Molent. “Historical Review”. In: *Fatigue Crack Growth Failure and Lifing Analyses for Metallic Aircraft Structures and Components*. Springer, Dordrecht, 2019. Chap. 1, pp. 1–20. ISBN: 9789402416756. DOI: 10.1111/j.1468-0483.1951.tb01033.x.

[67] P. Pokorný et al. “Crack closure in near-threshold fatigue crack propagation in railway axle steel EA4T”. In: *Engineering Fracture Mechanics* 185 (2017), pp. 2–19. ISSN: 00137944. DOI: 10.1016/j.engfracmech.2017.02.013.

[68] J. Tong. “Full-field characterisation of crack tip deformation and fatigue crack growth using digital image correlation—a review”. In: *Fatigue & Fracture of Engineering Materials & Structures* 41.9 (Sept. 2018), pp. 1855–1869. ISSN: 1460-2695. DOI: 10.1111/FFE.12859. URL: https://onlinelibrary-wiley-com.tudelft.idm.oclc.org/doi/full/10.1111/ffe.12859%20https://onlinelibrary-wiley-com.tudelft.idm.oclc.org/doi/abs/10.1111/ffe.12859%20https://onlinelibrary-wiley-com.tudelft.idm.oclc.org/doi/10.1111/ffe.12859.

[69] R Pippan and A Hohenwarter. “Fatigue crack closure: a review of the physical phenomena”. In: *Fatigue Fract Engng Mater Struct* 40 (2017), pp. 471–495. DOI: 10.1111/ffe.12578.

[70] K Minakawa and A.J McEvily. “ON CRACK CLOSURE IN THE NEAR-THRESHOLD REGION”. In: *Scripta Metallurgica* 15.6 (1981), pp. 633–636.

[71] S. SURESH and R. O. RITCHIE. “Geometric Model for Fatigue Crack Closure Induced By Fracture Surface Roughness.” In: *Metall Trans a* V 13A.N 9 (1982), pp. 1627–1631. ISSN: 03602133. DOI: 10.1007/bf02644803.

[72] R. P. Skelton and J. R. Haigh. “Fatigue crack growth rates and thresholds in steels under oxidising conditions”. In: *Materials Science and Engineering* 36.1 (1978), pp. 17–25. ISSN: 00255416. DOI: 10.1016/0025-5416(78)90191-X.

[73] P Edwards and M Ramulu. “Effect of build direction on the fracture toughness and fatigue crack growth in selective laser melted Ti-6Al-4 V ORIGINAL CONTRIBUTION”. In: (2015). DOI: 10.1111/ffe.12303.

[74] Punit Kumar, Om Prakash, and Upadrasta Ramamurty. “Micro-and meso-structures and their influence on mechanical properties of selectively laser melted Ti-6Al-4V”. In: *Acta Materialia* 154 (2018), pp. 246–260. ISSN: 13596454. DOI: 10.1016/j.actamat.2018.05.044. URL: https://doi.org/10.1016/j.actamat.2018.05.044.

[75] Thorsten Hermann Becker et al. “Near-threshold fatigue crack growth rates of laser powder bed fusion produced Ti-6Al-4V”. In: *Acta Materialia* 197 (2020), pp. 269–282. ISSN: 13596454. DOI: 10.1016/j.actamat.2020.07.049.

[76] M. Tarik Hasib et al. “Fatigue crack growth behavior of laser powder bed fusion additive manufactured Ti-6Al-4V: Roles of post heat treatment and build orientation”. In: *International Journal of Fatigue* 142.July 2020 (2021), p. 105955. ISSN: 01421123. DOI: 10.1016/j.ijfatigue.2020.105955. URL: https://doi.org/10.1016/j.ijfatigue.2020.105955.

[77] Nur Mohamed Dhansay. “Fatigue crack growth rate threshold of laser powder bed fusion Ti-6Al-4V”. PhD thesis. Stellenbosch University, 2021, p. 174.

[78] F.C Campbell. *Elements of Metallurgy and Engineering Alloys*. ASM International, 2008. Chap. Fatigue, pp. 243–264. ISBN: 978-0-87170-867-0.

[79] Haize Galarraga et al. “Fatigue crack growth mechanisms at the microstructure scale in as-fabricated and heat treated Ti-6Al-4V ELI manufactured by electron beam melting (EBM)”. In: *Engineering Fracture Mechanics* 176 (2017), pp. 263–280. ISSN: 00137944. DOI: 10.1016/j.engfracmech.2017.03.024. URL: http://dx.doi.org/10.1016/j.engfracmech.2017.03.024.

[80] ASTM E647−13. *Standard Test Method for Measurement of Fatigue Crack Growth Rates*. Tech. rep. 2014, pp. 1–50. DOI: 10.1520/E0647-15E01.2.

[81] ASTM E399. *Standard Test Method for Plane-Strain Fracture Toughness of Metallic Materials 1*. Tech. rep. 1997, pp. 1–31. DOI: 10.1520/E0399-09E02.2. URL: www.astm.org.

[82] Saeede Ghorbanpour et al. “Effect of microstructure induced anisotropy on fatigue behaviour of functionally graded Inconel 718 fabricated by additive manufacturing”. In: *Materials Characterization* 179 (Sept. 2021). ISSN: 1044-5803. DOI: 10.1016/J.MATCHAR.2021.111350.

[83] ASTM E112-13. “Standard Test Methods for Determining Average Grain Size”. In: *American Society for Testing and Materials* (2021), pp. 1–27. DOI: 10.1520/E0112-13R21.1.4.

[84] Ioannis Bantounas, David Dye, and Trevor C. Lindley. “The role of microtexture on the faceted fracture morphology in Ti–6Al–4V subjected to high-cycle fatigue”. In: *Acta Materialia* 58.11 (June 2010), pp. 3908–3918. ISSN: 1359-6454. DOI: 10.1016/J.ACTAMAT.2010.03.036.

[85] K. Sadananda and Dorai Nirmal V. Ramaswamy. “Role of crack tip plasticity in fatigue crack growth”. In: *https://doi-org.tudelft.idm.oclc.org/10.1080/01418610108214441* 81.5 (2009), pp. 1283–1303. ISSN: 01418610. DOI: 10.1080/01418610108214441. URL: https://www-tandfonline-com.tudelft.idm.oclc.org/doi/abs/10.1080/01418610108214441.

[86] Jian Gou et al. “Microstructure and mechanical properties of as-built and heat-treated Ti-6Al-4V alloy prepared by cold metal transfer additive manufacturing”. In: *Journal of Manufacturing Processes* 42 (June 2019), pp. 41–50. ISSN: 1526-6125. DOI: 10.1016/J.JMAPRO.2019.04.012.

[87] Ceyhun Köse and Engin Karaca. “Robotic Nd:YAG Fiber Laser Welding of Ti-6Al-4V Alloy”. In: *Metals 2017, Vol. 7, Page 221* 7.6 (June 2017), p. 221. ISSN: 2075-4701. DOI: 10.3390/MET7060221. URL: https://www.mdpi.com/2075-4701/7/6/221/htm%20https://www.mdpi.com/2075-4701/7/6/221.

[88] Uwe Zerbst et al. “Towards a methodology for component design of metallic am parts subjected to cyclic loading”. In: *Metals* 11.5 (2021). ISSN: 20754701. DOI: 10.3390/MET11050709.

[89] Sheng Hui Wang and Clemens Müller. “Fracture surface roughness and roughness-induced fatigue crack closure in Ti-2.5 wt% Cu”. In: *Materials Science and Engineering: A* 255.1-2 (Oct. 1998), pp. 7–15. ISSN: 0921-5093. DOI: 10.1016/S0921-5093(98)00785-0.

[90] A. J. McEvily et al. “Fatigue fracture-surface roughness and the K-opening level”. In: *International Journal of Fatigue* 19.8-9 (Sept. 1997), pp. 629–633. ISSN: 0142-1123. DOI: 10.1016/S0142-1123(97)00075-3.

[91] Valary Tubei et al. “3D short fatigue crack closure behavior in Ti-6Al-4V alloy investigated using in-situ high resolution synchrotron X-ray tomography”. In: *Engineering Fracture Mechanics* 249 (May 2021), p. 107755. ISSN: 0013-7944. DOI: 10.1016/J.ENGFRACMECH.2021.107755.

[92] Bernd Oberwinkler. “Modeling the fatigue crack growth behavior of Ti-6Al-4V by considering grain size and stress ratio”. In: *Materials Science and Engineering: A* 528.18 (July 2011), pp. 5983–5992. ISSN: 0921-5093. DOI: 10.1016/J.MSEA.2011.04.046.

[93] Sheng Cao et al. “Review of laser powder bed fusion (LPBF) fabricated Ti-6Al-4V: process, post-process treatment, microstructure, and property”. In: *Light: Advanced Manufacturing* 2.2 (2021), p. 1. ISSN: 2689-9620. DOI: 10.37188/lam.2021.020.

[94] Petr Miarka et al. “Influence of the constraint effect on the fatigue crack growth rate in S355 J2 steel using digital image correlation”. In: *Fatigue & Fracture of Engineering Materials & Structures* 43.8 (Aug. 2020), pp. 1703–1718. ISSN: 1460-2695. DOI: 10.1111/FFE.13198. URL: https://onlinelibrary.wiley.com/doi/full/10.1111/ffe.13198%20https://onlinelibrary.wiley.com/doi/abs/10.1111/ffe.13198%20https://onlinelibrary.wiley.com/doi/10.1111/ffe.13198.

[95] M Gupta, R C Alderliesten, and R Benedictus. “A review of T-stress and its effects in fracture mechanics”. In: (2014). DOI: 10.1016/j.engfracmech.2014.10.013. URL: http://dx.doi.org/10.1016/j.engfracmech.2014.10.013.

[96] C Betegon and J W Hancock. “Two-Parameter Characterization of Elastic-Plastic Crack-Tip Fields”. In: (1991). URL: http://asmedigitalcollection.asme.org/appliedmechanics/article-pdf/58/1/104/5461445/104_1.pdf.

[97] S Roychowdhury and Robert H Dodds. “A numerical investigation of 3-D small-scale yielding fatigue crack growth”. In: *Engineering Fracture Mechanics* 70 (2003), pp. 2363–2383. DOI: 10.1016/S0013-7944(03)00003-1. URL: www.elsevier.com/locate/engfracmech.

[98] Saswat Sahu. “Fatigue Behaviour of functionally graded Inconel 718 manufactured by selective laser melting”. PhD thesis. Delft university of technology, 2020. URL: http://resolver.tudelft.nl/uuid:edf44c06-a295-4f63-9d2c-181a128cc0d8.